UC Berkeley
UC Berkeley Electronic Theses and Dissertations

Title

Molecular Basis of Natural Phytochemical Effects on Mammalian Signal Transduction and Membrane Ion Transport

Permalink

https://escholarship.org/uc/item/5d8744ks

Author

Haoui, Monika

Publication Date

2020

Peer reviewed|Thesis/dissertation

Molecular Basis of Natural Phytochemical Effects on Mammalian Signal Transduction
and Membrane Ion Transport

By

Monika M. Haoui

A dissertation submitted in partial satisfaction of the

Requirements for the degree of

Doctor of Philosophy

in

Endocrinology

in the

Graduate Division

of the

University of California, Berkeley

Committee in charge:
Professor Gary Firestone, Co-Chair
Professor Polina Lishko, Co-Chair
Professor Thomas Carlson

Spring 2020

Abstract

Molecular basis of phytochemical effect on mammalian signal transduction and membrane ion transport

by

Monika M. Haoui

Doctor of Philosophy in Endocrinology

University of California, Berkeley

Professor Gary Firestone, Co-Chair

Professor Polina Lishko, Co-Chair

Natural products have been used for their medicinal properties throughout history, from ancient Mesopotamia to modern day herbal medicine. It is also estimated that 60% of currently available drugs are derived, either directly or indirectly, from natural products. Natural phytochemicals have been shown to exert strong anti-cancer, anti-obesity, and anti-bacterial effects as well as play a protective role against inflammation in the body and the brain. Due to their pleiotropic effects, these natural compounds have tremendous potential for treatment in diseases, such as melanoma and traumatic brain injury, where the heterogeneity within the tumor and among patients, respectively, has been shown to impede the development of new pharmacological agents for treatment. Melanoma, accounting for 3% of all skin cancers, but responsible for 65% of all skin-cancer related deaths, represents a great burden continuously on the rise. Current treatment options for metastatic melanoma offer short-term reprieve as resistance, due to intratumor heterogeneity, occurs within several months. Therefore, identification of a compound that can inhibit cell proliferation, regardless of the phenotype, is of dire need. Here, we show the anti-proliferative effects of 3'3-diindolylmethane (DIM), a bioactive compound found in cruciferous vegetables, on a diverse selection of melanoma cell lines. DIM inhibits cell growth in all treated melanoma cells through the down-regulation of the "master-regulator" of melanoma biology, the transcription factor, MITF-M. Due to its low toxicity, combining DIM with already established direct target therapies, could help patients overcome tumor heterogeneity driven-resistance without the deleterious effects of "cocktail-mixing". We also describe for the first time a novel activator of the inwardly-rectifying potassium channel, $K_{ir}7.1$. Progesterone, known for its positive effects following traumatic brain injury, was shown to potentiate $K_{ir}7.1$ current in multiple cell types, including choroid plexus epithelial cells, in a G-protein independent manner. We found this progesterone-induced activation of $K_{ir}7.1$ was inhibited in the presence of $20\mu M$ ursolic acid. Here, we describe for the first time an endogenous activator and natural phytochemical inhibitor of the Kir7.1, a vital ion channel in mammalian physiology.

Table of Contents

ACKNOWLEDGEMENTS:

When I started at UC Berkeley in Fall 2009 at 18 years old, I did not know I was about to spend 10 years there. None of this would have been possible if Gary Firestone hadn't taken a chance on me and invited me to join his lab after my MCB135A final (a class I then had the pleasure to teach alongside him for 6 years). Gary, I am forever grateful for your mentorship and friendship and will definitely miss our long conversations in your office. I would not love teaching as much as I do if it wasn't for you. You are the best professor I ever had. Thank you for everything! I'm also very happy that Omar Haffar and I were able to book-end your career as your first and last PhD students!

And to Polina, thank you for adopting me into your lab half-way through my PhD. I had three great years, especially learning electrophysiology alongside you. Our incredibly exciting (to me) ursolic acid discovery and my first time breaking into the cell were two of the most memorable moments in my PhD. Thank you for your guidance, energy and enthusiasm for the field; you taught me everything I know about ion channels.

I would also like to thank Thomas Carlson for being on my thesis committee and taking the time to meet with me to help plan out this thesis.

I am forever indebted to the Lishko lab girls for their constant support and friendship. I can't believe I found such a great girl gang in the sciences. Ida, Lenka, Liliya, Nadja, Nadine and Sarah – thank you for everything! And Ida, thank you for the $K_{ir}7.1$ project – you changed my life!

I'm also incredibly lucky to have such great friends from undergrad. There's no other group of people I'd rather spend my time with than the Cal Ski Team. I love you all and a special shout out goes to Frazer, Kari and Meg for supporting me and listening to my rants over the last 6 years. You guys are seriously the best.

Thank you to my parents for letting me move back home with the world's largest dog. I am incredibly lucky to have parents I enjoy spending every minute with and who love hiking Rylie as much as I do. Thank you for your encouragement and infrequent, yet perfectly timed, nagging. I could not have done this without you. And to Sophia, I'm lucky to have you as a sister/best friend.

And lastly to Craig; thank you for being by my side these last 6 years. You were the first person I would call every day after leaving lab and I can't imagine it any other way. Thank you for all the love, encouragement and support!

CHAPTER 1:

An Introduction

Skin Cancer, a global increasing threat:

The skin is the largest organ of the body comprising approximately 16% of the total adult body mass[1] and is the first line of defense against a host of external pathogens and environmental threats. The skin has three layers; the epidermis, the dermis and the hypodermis. The epidermis is made up of three types of cells: squamous cells, basal cells and melanocytes. Cancer of these cells; squamous cell carcinoma, basal cell carcinoma and melanoma, respectively, account for 99% of skin cancers.

Skin cancer is the most common malignancy worldwide and in the United States, more people are diagnosed with skin cancer each year than all other cancers combined[2,3]. Despite most cases being preventable with adequate sun protection, the rates of skin cancer incidence have continued to increase over the last two decades creating a significant, and costly, medical problem. In the past twenty years, there has been a 77% increase in nonmelanoma skin cancers diagnoses and in the past ten, a 47% increase in annual melanoma diagnoses[4,5]. There will be an estimated 100,350 new melanoma cases and 6,850 melanoma related deaths in the United States in 2020[5]. While melanoma only accounts for 3% of all skin cancer cases diagnosed each year, it is responsible for 65% of all skin cancer related deaths due to its high metastatic tendencies[6].

Melanoma:

Melanoma results from the transformation and malignant proliferation of melanocytes. Melanocytes are pigment-producing cells derived from the neural crest, a transient layer of multipotent embryonic cells that migrate during development and give rise to a diverse cell lineage. These cells are epithelial in nature and for migration to the epidermis undergo an epithelial to mesenchymal like transition characterized by loss of cell-cell contact and subsequent gain of a motile phenotype[7]. In malignant melanoma, this epithelial to mesenchymal process is exploited by tumor cells to undergo metastasis. Melanoma cells are therefore predisposed to exhibit invasive and metastatic traits due to lineage-specific factors associated with the development, differentiation and migration of melanocytes[8].

Melanoma diagnoses are given in stages characterized by thickness of tumor and whether the tumor has metastasized. Stage 1A signifies a 1mm thick tumor with no ulceration while stage 1B is 1mm thick with some ulceration. Stage 1A and stage 1B have a 97% and a 92% five-year survival rate, respectively[9]. As the tumor develops, the 5-year prognosis decreases dramatically. Stage 4 melanoma, or metastatic melanoma, has a five-year survival rate of only 15-20%[9].

Similar to most cancers, age remains one of the greatest risk factors for melanoma. Compared to younger populations, population over the age of 70 tend to have deeper primary melanomas as well as a higher number of metastasis. The average age of diagnosis is 63, with rates of

melanoma incidence in men double those seen in women. By age 80, the rates in men are triple those in women[5]. However, melanoma is not a male dominant cancer. Before the age of 50, the incidence rates in women are much higher than those of men. In fact, melanoma has become the second most common cancer in women aged 20 to 29 and the third most common in women aged 30 to 39[6] with 35% of women diagnosed with melanoma to be of child-bearing age[10]. Melamona is also one of the most commonly diagnosed cancers in pregnancy. While pregnancy is known to influence melanocyte pigmentation, with regards to melasma and linea nigra, there is currently no evidence to suggest that the increase of hormones, such as progesterone or estrogen, increase the incidence of melanoma[10]. Moreover, many studies have shown that women fare better than men with overall melanoma progression and survival[11–14]. Whether this is due to social and societal factors or biological factors is still inconclusive. While women are more likely to tan recreationally, either outside or using tanning beds, men are less likely to employ sun-protective measures when they are outside under direct UVR[15,16].

Ultraviolet radiation (UVR) is part of the natural energy produced by the sun and is classified as a "complete carcinogen" as it is both a mutagen and a non-specific damaging agent[1]. Risk of melanoma is correlated with UV exposure in a dose dependendent manner[17] and is causative for 65% of melanomas and 90% of nonmelanoma skin cancers[1]. UVR consists of two types, UVA and UVB, making up 95% and 5% of UVR, respectively. UVA has longer wavelengths and can pass deeper through the skin, but is less genotoxic while UVB has shorter wavelengths and can cause direct DNA damage in the form of photoproducts. However, these photoproducts are quickly recognized and repaired by nucleotide excision repair (NER) pathway. Therefore, the indirect DNA damage by UVA, primarily through free radical formation and oxidative stress, is believed to be the cause of skin damage and ultimately tumorigenesis[2].

In response to UV exposure, melanocytes ramp up production of melanin to protect the skin against further DNA damage. There are two forms of melanin, eumelanin and pheomelanin. Eumelanin is a brown/black pigment that is characteristic for its UV-blocking properties, preventing UVR penetration of the epidermis. Pheomelanin is a red/blond melanin bioaggregate that is less capable of blocking UV radiation and can itself induce DNA damage by promoting free radical formation[18]. Eumelanin is produced when neighboring keratinocyte cells release α-melanocortin stimulating hormone (α-MSH) in response to UV damage. α-MSH binds melanocortin-1-receptor (MC1R) on melanocytes, beginning an intracellelar signaling cascade that results in the transcription of pigment-producing enzymes. MC1R gene has a high number of polymorphisms which are associated with decreased production of eumelanin and an increase in pheomelanin. These polymorphisms are predominantly found in caucasian populations, resulting in light haired, fair skinned individuals with poor protection against UVR penetration. As a consequence, these individuals are 70 times more likely to develop skin cancer than those with dark skin[19]. In regards to melanoma specifically, for Caucasian males and females in the United States the risk of melanoma is 33.0 and 20.2 per 100,000, respectively, while the risk for African American males and females is only 1.2 and 1.1 per 100,000, respectively[20].

Cancer, a disease of somatic mutations, has significant variation in mutation rate among the different types. Out of all cancers, the rate of mutation is highest in melanomas [21] and is directly correlated with UV exposure as melanomas originating from chronically sun-exposed skin have the largest number of mutations[21]. The most common mutation in melanoma is in the oncogenic

serine/threonine protein kinase BRAF, with 50% of all melanomas harboring activing BRAF mutations. BRAF is a member of the RAS/RAF/MEK/ERK pathway which regulates many downstream transcription factors involved in cell differentiation, proliferation, growth and apoptosis. 90% of BRAF mutations are a substitution of valine for glutamic acid at codon 600 (BRAFV600E) resulting in a constitutively active form of BRAF[22]. Other mutations in the RAS/RAF/MEK/ERK (MAPK) pathway include NRAS, mutated in greater than 20% of cutaneous melanomas, and CDKN2A, a downstream cell cycle regulator mutated in 13% of melanomas and deleted in 30%[21]. Mutations in tumor suppressors such as PTEN and p53 are also common. Due to these mutations, melanoma is one of the most complex and hetergeneous cancers, and as a result, difficult to treat.

Melanoma is also the most costly skin cancer, both financially and in regards to lives lost, due to its increasing incidence rate and large metastatic potential. Everday, twenty Americans die from metastatic melanoma[23]. Annually, one million Americans are treated for melanoma, costing an average of $3.6 billion[3]. Early detection is crucial for survival, since surgery is still the most effective form of treatment. Once the cancer has metastasized, current treatment options are limited, and rates of recurrence are high. The most promising treatment option is targetted therapy, in which drugs are used to attack cancer cells specifically, causing less damage to normal cells than chemotherapy and radiation therapy. Current targetted therapies include signal transduction inhibitors such as Vemurafenib and Dabrafenib, both oncogenic BRAF inhibitors and Trametinib, a MEK inhibitor. All three drugs are inhibitors of the oncogenic BRAF pathway, which has been implicated in more than 50% of melanoma cases[24]. However, resistance to these drugs develops within 11 months after initial treatment[25] and combinatorial therapy using both BRAF and MEK inhbitors have not shown much benefit[26]. Therefore, there is an urgent need for novel therapeutics targeting alternative signal transduction pathways to be used in conjunction with current BRAF pathway inhibitors to potentially eliminate resistance and recurrence. A novel target could be MITF-M, the master regulator of melanocytes, which is overexpressed in 80% of patients taking BRAF/MEK inhibitors and is known to confer resistance to both BRAF and MEK inhibitors[27]. β-catenin, a signaling molecule downstream of the canonical Wnt-signaling pathway is a known regulator of MITF in both melanocyte development and melanoma progression and could therefore be a potential target to down-regulate the expression of MITF-M[28].

MITF-M: The Master Regulator of Melanocytes

Micropthalmia-associated transcription factor (MITF) is a basic-helix-loop-helix leucine zipper transcription factor family consisting of nine different isoforms differing in their first exons and promoters[29]. MITF is essential for development in a diverse array of tissue types as mutations in MITF can cause micropthalmia (small eyes), Waardenburg Syndrome Type IIA and Tietz Syndrome[30]. Waardenburg Syndrome Type IIA and Tietz syndrome are both rare genetic condition that are characterized by generalized hearing loss and pigmentation deficiencies. MITF-M is the melanocyte specific isoform often referred to as the "master regulator" of melanocytes because it controls melanocyte differentiation, migration, proliferation and survival. Mice lacking MITF do not develop mature melanocytes[30].

MITF-M transcription and activity levels are tightly regulated throughout development by several transcription factors, SOX10, PAX3, β-catenin and CREB, which all bind unique sites in the MITF-M promoter. SOX10 and β-catenin are critical for melanoblast development from the neural crest and play a major role in differentiation of progenitor cells. PAX3 regulates the proliferation of melanocyte stem cells (MSCs) and prevention of terminal differentiation. Lastly, CREB drives melanocyte differentiation by activating melanogenesis pathways.

The development of melanogenesis pathways is the ultimate step in the melanocyte differentiation process. MITF-M, a central regulator of melanogenesis, directs the α-MSH induced expression of three critical pigmentation enzymes; tyrosinase (TYR), tyrosinase-related protein 1 (TYRP1) and dopachrome tautomerase (DCT). MC1R binds α-MSH, released by keratinocytes post UV-induced damage, stimulating the elevation of intracellular cAMP levels, activation of phosphokinase A and subsequent phosphorylation and activation of CREB. Activated phospho-CREB binds the cAMP response element in the MITF-M promoter inducing transcription of MITF-M. MITF-M then binds to the E-box (CA[T/C]GTG) motif in the promoter of genes encoding pigmentation-related enzymes, thereby increasing eumelanin production[31].

Regulation of proliferation by MITF-M is a more complicated story. MITF-M regulates both the transcription of Cdk2, which promote G1 to S progression, as well as p16, which promotes cell cycle exit, and p21, an inhibitor of G1 to S progression. This multi-regulation could be explained by the multiple roles of MITF-M during development and the timing of those roles. During early development, as melanoblasts are proliferating, MITF-M is regulating their proliferation through transcription of Cdk2. Later in development, MITF-M controls differentiation and a critical step in proper differentiation is cell cycle exit, therefore it would be necessary for MITF-M to control p16 and p21 transcription.

This competing dual-role of MITF-M is very apparent in melanomas. MITF is a driver of melanoma progression and considered to be a melanoma addiction oncogene/lineage survival oncogene[32,33]. It is expressed in more than 80% of melanomas, detectable throughout all stages of melanoma development and amplified in approximately 5-20% of human melanomas[33,34]. It has been shown to control both the proliferative and invasive (metastatic) properties of melanoma cells. The MITF Rheostat model, first described by Carriera et al, explains MITF-M's

dual role in melanoma. The rheostat model describes three levels of MITF activity corresponding to three distinct melanoma cell phenotypes all found within a single tumor. High-level of MITF-M activity has been shown to promote differentiation and cell cycle arrest, mid-level activity has been shown to promote proliferation and low-level activity has been shown to promote stem-like characteristics and invasive potential[35]. Absence of MITF-M all together triggers senescence or cell death[36]. As a result, this tumor heterogeneity has become one of the largest hurdles in the treatment of melanoma. MITF-M is a transcription factor and therefore more challenging to target. Instead, targeting upstream regulators of MITF-M could potential be the key to regulating melanoma proliferation and progression. One key regulator of MITF-M in both melanocyte development and melanoma progression is β-catenin. β-catenin plays a crucial role in the phenotypic transition from proliferative to invasive and protein levels correlate with those of MITF-M.

Wnt Signaling

The Wnt family of proteins, with over 19 members, have been proven essential for development and adult tissue regeneration[37]. The canonical Wnt/β-catenin pathway and the non-canonical Wnt pathways have been implicated in the formation and development of neural-crest derived melanocytes[38]. Abnormal signaling of these pathways has been shown in many human cancers including colorectal cancer, lung cancer, breast cancer and melanoma[39].

The canonical Wnt/β-catenin signaling pathway plays a key role in cell fate decisions during early embryogenesis and regulates the proliferation and differentiation of neural crest cells[38]. The switch from pluripotent neural crest progenitor to melanoblast and then to mature melanocyte is mediated by Wnt signaling through β-catenin, specifically by Wnt1 and Wnt3a[40]. Cells contain two pools of β-catenin, one that is associated with cadherins at cell-cell junctions and the other which is "free" in the cytosol and the nucleus. This "free" pool of β-catenin is tightly regulated and when a cell is in resting state, a destruction complex, consisting of casein kinase 1-alpha (CK1α), adenomatous polyposis coli (APC), axin and constitutively active glycogen synthase kinase 3 (GSK3), maintains β-catenin at a low level by phosphorylating it thereby tagging it for degradation by the 26S proteasome[41]. Upon Wnt stimulation, the destruction complex dissociates and GSK3 is recruited to the membrane, displacing it and allowing for accumulation and nuclear translocation of β-catenin. Inside the nucleus, β-catenin binds to the T cell factor/lymphocyte enhancer binding factor family (TCF/LEF), inducing transcription of β-catenin/TCF/LEF responsive genes, such as MITF-M[42]. Wnt ligands (such as Wnt1 and Wnt3a) bind to their cognate frizzled (Fzd) receptors, a family of seven pass transmembrane receptors as well as LRP co-receptors, LRP5 and LRP6, resulting in the recruitment of the destruction complex to the plasma membrane, thereby inactivating it[43].

The non-canonical Wnt signaling pathways are mostly independent of β-catenin and comprise the Wnt/planar cell polarity (PCP) signaling and the Wnt/Ca^{2+} signaling. The Wnt/PCP pathway is essential for tissue patterning and morphogenesis as well as polarized cell migration. The Wnt/Ca^{2+} signaling pathway regulates intracellular calcium levels and is involved in cell migration as well as cell differentiation[43]. Binding of Wnt ligand, Wnt5a, to its Fzd receptor leads to the inositol 1,4,5-triphosphate (IP3) triggered calcium release from the ER, which activates protein kinase C as well as calcium/calmodulin-dependent protein kinase II (CaMKII), both of which activate various transcription factors[44]. While Wnt5a mostly regulates through the Wnt/Ca^{2+} signaling pathway, it has been shown to regulate β-catenin levels in melanoma cells, driving cells from the proliferative phenotype to the invasive phenotype[45].

Both canonical and non-canonical Wnt signaling pathways are important for melanoma progression and changes in these pathways have been linked to phenotype switching in melanoma cells. Canonical Wnt signaling is important for early stages of tumor development by promoting proliferation. Cells with high levels of β-catenin have been shown to be more proliferative and more differentiated while cells with low amounts of β-catenin are more invasive. The non-canonical Wnt5a is detected in later stages of melanoma progression and has

been shown to promote invasion and metastasis as well as downregulate β-catenin[28]. As a result, tumors from melanoma patients can be divided into two groups based on their Wnt5a and MITF expression levels. A Wnt5a high, MITF low profile corresponds with highly metastatic tumors while a MITF high, Wnt5a low profile corresponds with less metastatic tumors[45]. These results correlate strongly with the rheostat model of MITF-M in melanoma. High levels of β-catenin and therefore high levels of MITF-M as well as low levels of Wnt5a correspond with a proliferative phenotype while high levels of Wnt5a, low levels of β-catenin and low levels of MITF-M correspond with an invasive phenotype. Together, the canonical and the noncanonical Wnt signaling pathways mediate the progression of melanoma from largely proliferative to highly invasive.

3,3'-Diindolylmethane against Cancer

Plant-derived compounds are an important source of anti-cancer agents as 60% of the anti-cancer agents approved for treatment over the past 80 years have been derived either directly or indirectly from natural products[46]. 3,3'-diindolylmethane (DIM) is a phytochemical naturally occuring in the cruciferous vegetables of the *Brassica* genus. Cruciferous vegetables, which include cabbage, brocolli, brussel sprouts and bok choy, can be distinguished from other vegetables by their high concentration of glucosinolates, a sulfur-containing compound responsible for their characteristic bitter taste. When the vegetables are cut or chewed, myrosinase, an endogenous enzyme normally localized to a separate compartment, hydrolyzes glucosinolates into various metabolites including the bioactive compound, indole-3-carbinol (I3C)[47]. I3C then naturally self-condenses to its dimer form, DIM, in acidic pHs such as the gut. In rodents fed I3C, DIM was readily detected in the liver and feces one hour to twenty-four hours post feeding, while I3C was not[48].

The anti-cancer properties of cruciferous vegetables have been known for centuries as it was first documented by Cato and Elder (234-149 BC) in his study of medicine, "if a cancerous ulcer appears on the breasts, apply a crushed cabbage leaf and it will make it well"[49]. In 1996, Verhoeven et al. reviewed 7 cohort studies and 87 case-control studies on the assocation between cruciferous vegetable consumption and cancer risk and found that 67% of the case-control studies showed a decreased cancer risk when consuming cruciferous vetables[47], especially in lung and colorectal cancers. *In vitro,* treatment with I3C or DIM has been shown to induce apoptosis in human prostate, breast and cervical cancer cells [50]. DIM has also been shown to inhibit cell proliferation in Human Hepatocellular Carcinoma cells[51] and Human Endometrial Ishikawa cells[52]. Therefore, DIM has great potential as a chemopreventative agent due to its ability to target diverse pathways in distinct cell types.

Tumor heterogeneity is the most challenging aspect of melanoma treatment as resistance to single targetted therapies is inevitable. While combinational therapies are more promising, the use of multiple drugs can lead to high levels of added toxicity. DIM has been shown to have no toxic effects in rodents given 0, 5, 10, and 20mg/kg/day [53] as well as in humans given 75mg/day for 30 days[54]. Therefore, DIM could potentially be a safe and potent drug to use in combination with other chemotherapy drugs to maximize efficacy of treatment without increasing toxicity to the patient.

Triterpenoids as Anti-Cancer Agents

Triterpenoids form the largest class of natural phytochemicals, consisting of 20,000 different molecules, ubiquitously found throughout plants[55]. Triterpenoids have been extensively studied in recent years due to their pleiotropic effects, including, but not limited to, anti-cancer, anti-bacterial, anti-obesity as well as anti-inflammatory effects[55,56]. These compounds have shown great pharmacological potential with very low toxicity[57]. In the western world, it is predicted that we consume on average 250mg of triterpenoids per day. In the Mediterranean diet, a diet known for its health benefits, intake of triterpenoids could reach 400 mg/kg/day[57].

Three triterpenoids, ursolic acid, pristimerin and lupeol are known for their anticancer properties. Lupeol, found in vegetables such as peppers, cucumbers, tomato, olive, fig, mango, strawberries, red grapes as well as medicinal plants such as American ginseng and shea butter, has been shown to induce anti-proliferative effects on colorectal and gastric cancers[57,58]. Ursolic acid, found in the wax coating of some fruit including pears, apples and prunes, and medicinal plants such as motherwort, has been shown to play an anticancer role in a wide range of cancers. This includes, but is not limited to, ovarian carcinoma, pancreatic carcinoma, prostate cancer, cervical carcinoma, breast cancer, colorectal cancer as well as leukemia[58,59]. Pristimerin is less common and found in more obscure medicinal plants such as the thundergod vine. Regardless, it's anticancer effects are just as wide spread affecting a large range of cancer cell lines including oral cancer, colorectal cancer, glioma, leukemia, breast cancer, lung cancer and prostate cancer[60]. Pristimerin has been shown to inhibit growth and metastasis as well as induce apoptosis and autophagy in these cancer cells through multiple pathways including the MAPK pathway, the PI3K/AKT/mTOR pathway, NF-kB pathway and Wnt/beta-catenin pathway[60,61]. Therefore, the pleiotropic effects of these three compounds could be very beneficial in the treatment of cancers such as melanoma, where there is such a high amount of tumor heterogeneity.

Part II

The Choroid Plexus and Cerebrospinal Fluid

The choroid plexus (CP), located within each ventricle of the brain, is a highly vascularized and highly conserved tissue. The development of the choroid plexus starts in the fourth ventricle, then develops in the two lateral ventricles and lastly, the third ventricle[62]. The structure and the developmental pattern of CP is conserved among all species, from lower vertebrate to humans[63]. The CP is a secretory epithelial tissue, manufacturing 80% of the cerebrospinal fluid (CSF) in the brain[64]. In each ventricle, the CP consists of a single layer of cuboidal epithelial cells lining a complex network of fenestrated capillaries[62,64]. These choroid plexus epithelial cells form tight junctions with one another, creating a blood-CSF barrier to prevent paracellular passage of molecules and thereby controlling the composition of CSF[65] (Figure 1). In contrast to the blood brain barrier, the blood-CSF barrier is fenestrated and allows movement of small solutes from the blood to the CSF. The CP receives more blood flow per gram of tissue than any other tissue in the body and produces 400-600mL CSF per 24 hours[62,66,67]. The CSF has three main functions: to protect the brain, supply nutrients to the central nervous system and remove waste products from cerebral metabolism.

Cerebrospinal fluid is a clear, plasma-like fluid that bathes the central nervous system. First produced by choroid plexus epithelial cells in the lateral ventricles, CSF flows down the neuroaxis into the third ventricle, then through the cerebral aqueduct to the fourth ventricle where it eventually empties into the cerebral subarachnoid space surrounding the brain (Figure 2)[68]. From the subarachnoid space, CSF is reabsorbed into the dural venous sinuses through arachnoid granulations[69]. Complete immersion by CSF allows the brain to become buoyant, thereby reducing its 1500 gram weight to a lesser 50 gram weight and acts as a shock absorber, protecting the brain from damage during head trauma[70]. Complete CSF turnover occurs four times per day, as the subarachnoid space and the ventricles can only hold 125ml and 25ml, respectively[62,70,71]. Unidirectional passage of CSF throughout the brain also allows for removal of waste products, i.e. glycosylated proteins, excess neurotransmitters, debris from the lining of the ventricles as well as pathogens such as bacteria and viruses[72,73]. These biochemical waste products diffuse into the CSF and are removed as the CSF is reabsorbed into the dural venus sinus. Proper clearance of waste metabolites allows for normal function of the brain. Lastly, to maintain a stable environment for the brain, choroid plexus epithelial cells regulate the nutrient and ion composition of the CSF. This tightly controlled production occurs in two steps: the passive movement of water across capillaries and the active transport of ion across choroid plexus epithelial cells[67].

Cerebrospinal fluid formation begins as plasma is passed through a network of fenestrated capillaries in the basement membrane of the choroid plexus epithelial cells[64]. This initiates the flow of water, ions and small molecules from the plasma into the interstitial fluid of each plexus. Sodium ions move down their concentration gradient from the plasma into the epithelial cytoplasm via the sodium-proton pump is the basolateral membrane of the cell. A Na^+/K^+ ATPase in the apical membrane then actively pumps 3 Na^+ ions out of the cell and 2 K^+ ions into the cell, against their concentration gradient, with the use of one ATP molecule[64,65,74]. Anion transport of Cl^- and HCO_3^- across the luminal membrane follows. The transcellular transport of Na^+ and Cl^- ions generates an osmotic gradient that, in turn, drives the secretion of water from the plasma, across the choroid plexus epithelium, to the ventricular lumen through the aquaporin 1 (AQP1) channel[64]. Lastly, the K^+ ions that were brought into the cell by Na^+/K^+-ATPase are then pumped out by apical facing K^+ channels (Figure 3). There are two types of K^+ channels in choroid plexus epithelium, the inward-rectifying $K_{ir}7.1$ and the outward-rectifying $K_v1.1$ and $K_v1.3$. These K^+ channels sustain Na^+/K^+- ATPase activity by providing an efflux pathway for K^{+}[64]. Aside from the transport of ions, the choroid plexus also transports, as well as produces, important proteins, nutrients and metabolic precursors that affect a wide range of CNS functions[68,75]. While originally thought of as an ultrafiltrate of plasma, CSF is indeed a highly regulated composition of ions and nutrients necessary for brain function.

K$_{ir}$7.1 in the Choroid Plexus and Retinal Pigment Epithelial Cells

Identified by the Clapham group in 1998, K$_{ir}$7.1 is the most recent member of the Kir family of inwardly-rectifying potassium channels[76]. The Kir family has fifteen members classified in seven subfamilies (K$_{ir}$1-7)[77]. Each K$_{ir}$ has a tetrameric structure with two transmembrane segments and a pore between them to conduct potassium[78]. Under experimental conditions, K$_{ir}$ channels will pass a greater inward current (into the cell) than outward. However, under physiological conditions of the cell, K$_{ir}$ channels mainly conduct K$^+$ current outward[76]. This is due to the large difference in K$^+$ concentrations 100mM [K$^+$]$_{inside}$ and 5mM [K$^+$]$_{outside}$ of mammalian cells. K$_{ir}$7.1 is a unique K$_{ir}$ channel and only shares 38% homology with its closest relative, K$_{ir}$4.2[79]. Unlike the other K$_{ir}$ channels, who have a conserved arginine in the pore region, K$_{ir}$7.1 has a methionine. As a result K$_{ir}$7.1 has a low single channel conductance, is not sensitive ions such as barium, cesium or magnesium, which are known to inhibit other K$_{ir}$ channels[76]. Mutating the methionine back to an arginine increased the single channel conduction approximately 20-fold and barium sensitivity 10-fold to resemble a rectification profile more similar to the other K$_{ir}$ channels[79]. The family of K$_{ir}$ channels can be divided into four functional groups: the classical constitutively active K$_{ir}$ channels, G-protein gated K$_{ir}$ channels, ATP-sensitive K$^+$ channels and lastly, K$^+$ transport channels[79].

K$_{ir}$7.1 belongs to the subfamily of K$^+$ transport channels and is found in many tissue types including, but not limited to, the choroid plexus epithelial cells, retinal epithelial cells, and renal epithelial cells[78,80,81]. In these three epithelia, K$_{ir}$7.1 is co-localized with the Na$^+$/K$^+$-ATPase. In the choroid plexus and retina, K$_{ir}$7.1 and Na$^+$/K$^+$-ATPase are co-localized on the apical side on the cell, while in the kidney they are co-localized to the basolateral side[81–83]. K$_{ir}$7.1's role in these three cells is very similar. Na$^+$/K$^+$-ATPase transports three Na$^+$ ions and two K$^+$ against their concentration gradients with the use of one molecule of ATP. K$_{ir}$7.1, as a K$^+$ transport channel, then recycles the K$^+$ ions back across the membrane. The Na$^+$ gradient established by Na$^+$/K$^+$-ATPase drives secondary active transport, such as Cl$^-$ across the membrane, which osmotically drives water across the epithelial cells through the aquaporin channels[76]. While K$_{ir}$7.1 plays a role in all three epithelia, mutations in K$_{ir}$7.1 are known to interfere with retinal epithelial function, leading to blindness.

Mutations in KCNJ13, the gene that encodes K$_{ir}$7.1, lead to Leber Congential Amaurosis (LCA), a frequent cause of pediatric blindness, as well as Snowflake Vitreoretinal Degeneration (SVD), an autosomal dominant disorder that leads to clouding of the lens of the eye[82]. In these diseases, patients lose the electrical activity generated in the retina in response to light. This is because K$^+$ ions are not being replaced in the sub-retinal space after being transported into the cell by Na$^+$/K$^+$-ATPase. As a result, the cyclic nucleotide-gated ion channel (CNG) cannot uptake K$^+$ ions from the sub-retinal space to facilitate phototransduction and the electrical activity of the cell is reduced[84].

Currently there is one pharmacological inhibitor of K$_{ir}$7.1, VU590 dihydrochloride, and no known activator. K$_{ir}$7.1 is a vital ion channel, as total knockout mice die before birth[82]. Therefore, investigating the regulatory functions of K$_{ir}$7.1 is essential to further understanding its vital role in these epithelial tissues.

Traumatic Brain Injury

Traumatic Brain Injury (TBI), defined as structural and/or physiological disruption of brain function due to external force, affects the lives of 50-60 million people each year and is the leading cause of death and disability world-wide[85]. An estimated 5.3 million Americans are currently living with permanent TBI-related disability, including cognitive, sensory and motor impartments[86]. These disabilities are usual due not to the initial impact, but to secondary insult such as delayed non-mechanical damage due to neuroinflammation and cerebral edema[87]. There are multiple types of cerebral edema. The most frequent is post-traumatic hydrocephalus (PTH) which is reported to occur in 30-86% of TBI patients[88]. First reported in 1914, PTH occurs when excessive CSF collects in the brain due to accumulation of cell and proteins in the CSF, blocking CSF outflow. Excessive accumulation of cells and proteins in the CSF is usually due to a breakdown of CP function.

Despite its location in the center of the brain, choroid plexuses are still quite vulnerable to brain impact. The lateral choroid plexuses are damaged by lateral hits to the brain and the choroid plexus in the third ventricle is impacted by frontal blows[89]. Epithelial damage in the CP results in a breakdown of the blood-CSF barrier, allowing increased permeation of solutes across CP into the ventricular CSF[64,89]. This movement of macromolecules increases the osmotic pressure in the CSF, thereby increasing the flow of water into the ventricles, and ultimately resulting in swelling of the brain[71,90]. CSF with high concentration of macromolecules cannot be appropriately drained out of the subarachnoid space and instead accumulates in the brain. Lack of CSF flow-through results in not only problems in removal of waste and toxins but also interferes with nutrient delivery throughout the brain. Pressure from CSF build-up on CP causes a release of peptides, such as atrial natriuretic peptide (ANP), for fluid regulation as well as growth factors for neurogenesis of damaged cells[89,91]. The CP also absorbs harmful molecules from the CSF and enzymatically breaks them down within lysosomes in the epithelial cells[89]. While the exact mechanism of CP stabilization post-injury is unclear, it is clear that the CP plays a critical role in facilitating TBI recovery. Therefore, pharmacologic boosting of CP repair mechanisms may improve neurogenesis and help restore cognitive abilities after traumatic brain injury.

Progesterone and Traumatic Brain Injury

One promising therapeutic for treatment of traumatic brain injury is administration of progesterone. Progesterone, known mostly for its reproductive effects, is also a true neurosteroid. Synthesized by oligodendroyctes and some neurons in the brains of both men and women, P4 is thought to be involved in many normal functions of the brain as well as in repair[92–94]. Early studies showed female mice are less susceptible to secondary brain injury than male mice, suggesting females have endogenous neuroprotection[85,95]. Over the past twenty years, more than 100 articles have been published showing the benefits of progesterone using 22 different models of injury across 4 species, including human[94]. Progesterone administration after TBI has been shown to have pleiotropic effects in the brain, including reduction of lesion volume and neuronal

loss, reduction of cerebral edema and improvement of cognitive function[95,96]. Female mice displayed smaller lesions than male mice, however when male mice were administered P4, they displayed lesion size reduction comparable to female mice[95]. The functional outcomes of female mice injured at their peak P4 levels were significantly better than those injured when their P4 levels were low[94]. P4 was also able to improve blood-brain barrier integrity and attenuate the increased expression of inflammatory molecules following TBI in both male and female mice administered P4[97]. Endogenous and exogenously administered P4 showed decreases in cerebral edema following traumatic brain injury. Due to increased pressure, cerebral edema can kill nerve cells. Therefore, immediate control of edema is necessary for positive outcomes. P4, in mice, was shown to reduce cerebral edema by day 3 to that normally seen by day 7[98].

While promising in mice models, the heterogeneity of traumatic brain injury in humans has made clinic trials difficult[99,100]. The Cochrane Database for Systemic Reviews found no significant benefit of P4 for risk of death and moderate benefit for improved cognitive function. According to the report, the heterogeneity of studies done and the heterogeneity of traumatic brain injuries themselves, result in inconclusive data regarding the possible beneficial effects of P4 on TBI. Traumatic Brain Injury, like cancer, is not a uni-dimensional disorder and should not be treated as such[100]. Therefore, understanding the mechanism of action of P4 in the brain will be crucial for treating specific TBIs.

Ursolic Acid and Traumatic Brain Injury

Ursolic Acid (UA), one of the most common triterpenoids in plants, has been shown to have a multitude of cellular effects related to anti-cancer, anti-inflammation, anti-diabetes, anti-obesity, as well as anti-neurodegeneration[55,101]. Found mostly in herbs such as basil, rosemary, and sage, as well as fruits such as apples and pears, ursolic acid is a promising pharmacological compound with low toxicity[55]. In mice, UA has been shown to reduce brain edema and neurological insufficiencies when administered 24 hours after TBI induction. This was through increased nuclear translocation of Nrf2, a transcription factor that regulates expression of antioxidant proteins that protect against inflammation and injury, as response to UA was ablated in Nrf2$^{-/-}$ mice[102]. In rats, UA administered over a 48 hour period after subarachnoid hemorrhage brain injury was shown to reduce significantly intracellular inflammatory markers such as IL-6, TNF-α, IL-1β and NF-kB[103]. However, the neurological effects of UA are not limited to TBI, where the blood-brain and blood-CSF barriers have been compromised. UA was detected in the cerebrum of healthy rats 1 hour after oral administration[101], indicating its ability to cross even an intact blood-brain barrier. Accordingly, UA has been shown to attenuate cognitive deficits associated with Alzheimer's and Parkinson's through regulation of oxidative stress and inflammation in the brain[104]. Therefore, along with progesterone, ursolic acid has great potential for the treatment of neurological diseases.

Thesis Overview:

There is large promise in the use of natural phytochemicals in pharmacology due to their pleiotropic effects in mammalian models and low toxicity. The following two chapters describe the molecular basis in which natural compounds effect mammalian signaling and ion transport. In chapter 2, we focus on the anti-proliferative mechanisms of 3,3'-diindolylmethane as well the natural triterpenoids, ursolic acid, lupeol and pristermin, on multiple melanoma cell lines with distinct mutational profiles. While this work does not identify the direct target of 3,3'-diidnolylmethane in melanoma cells, it gives greater understanding to the molecular basis of 3,3'-diindolylmethane's anti-proliferative effects. In chapter 3, we describe the activation of the inwardly-rectifying $K_{ir}7.1$ potassium channel by progesterone in the choroid plexus epithelial cells and retinal epithelial cells. This is a direct activation as it was G-protein coupled receptor and ABHD2 independent. We also show the antagonistic effects of Ursolic Acid on progesterone activation of $K_{ir}7.1$ and discuss the possible physiological consequences of this.

Figure 1
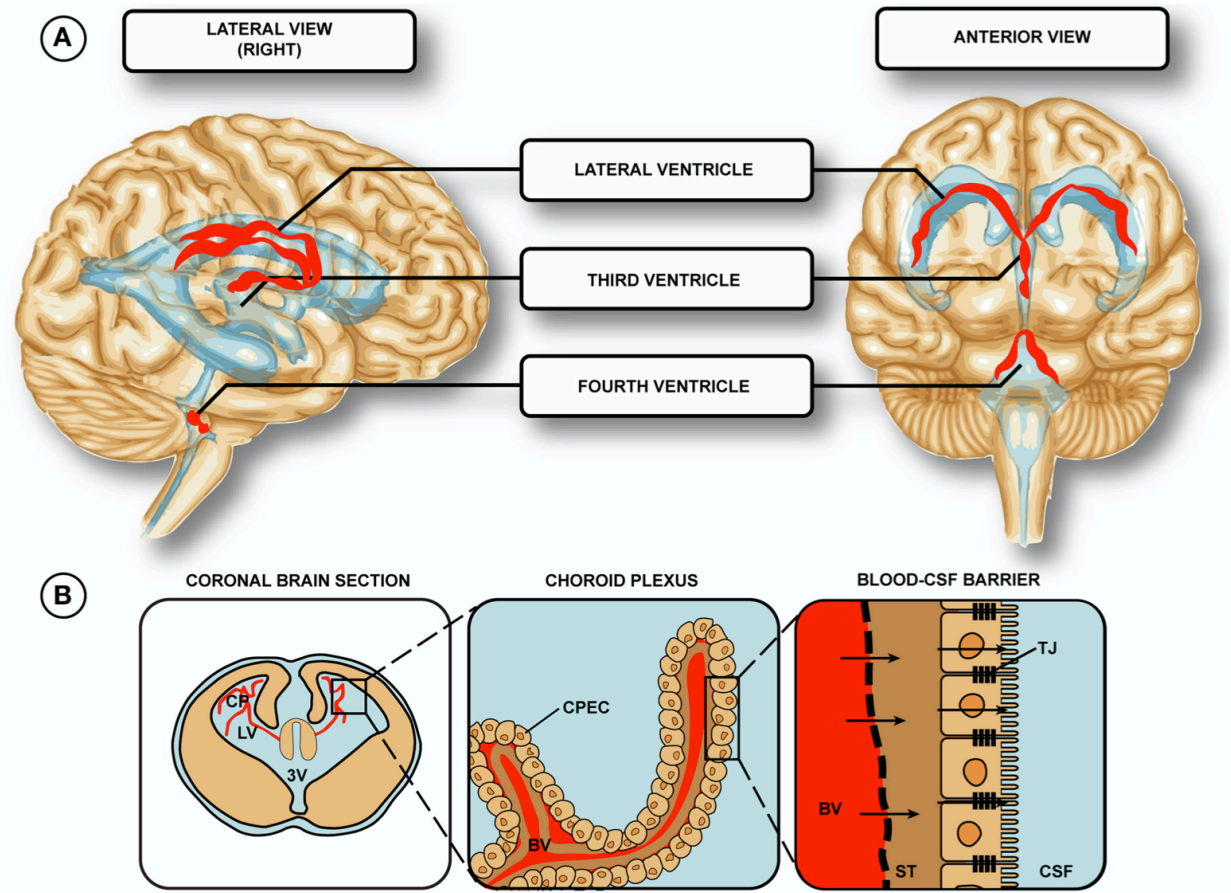
Figure 1: Localization of the Choroid Plexus in the Brain

(A) Lateral and anterior views of the brain describing the location of the choroid plexus tissues. There are two located in the lateral ventricle, one in the third ventricle and one in the fourth ventricle

(B) A subsection of the lateral ventricle shows capillaries lined with a single layer of cuboidal epithelial cells. Tight junctions (TJ) between the choroid plexus epithelial cells (CPEC) create a barrier between the blood and the CSF known as the blood-CSF barrier (BCSFB).

Adapted from Liddelow, 2015[105]

Figure 2:
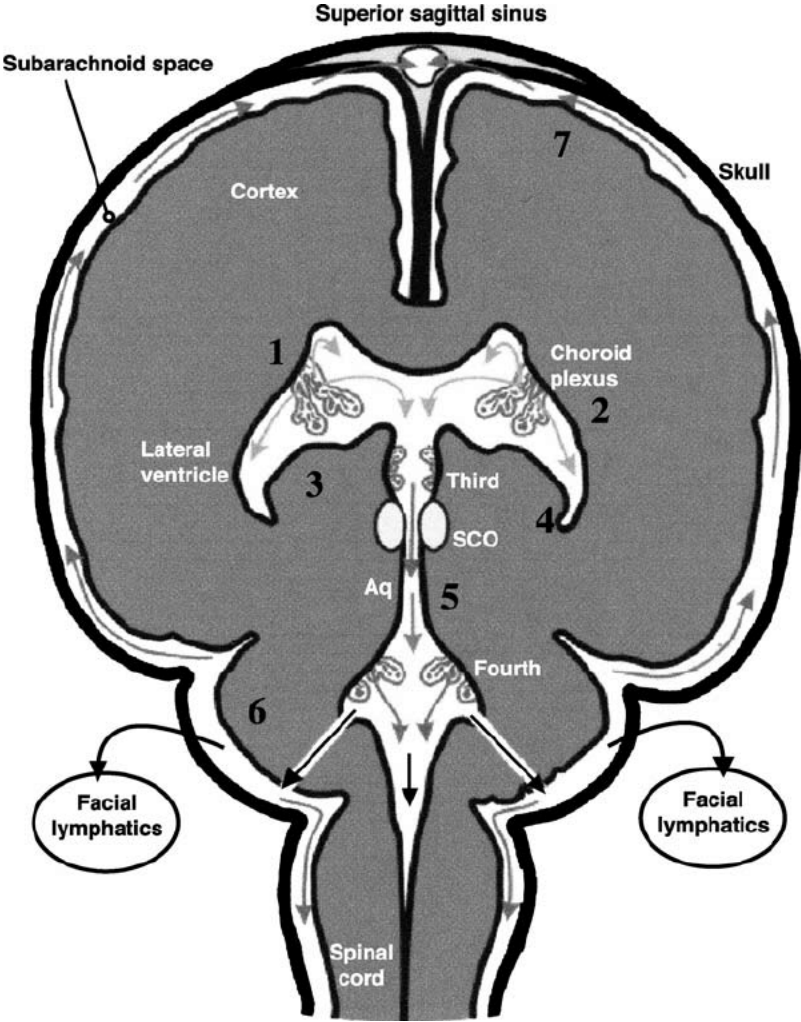
Figure 2: CSF flow pathways in adult

CSF originates from the choroid plexuses of the lateral and third ventricles, and travels downward through the narrow cerebral aqueduct (Aq), which empties into the fourth ventricle. CSF then flows out of the fourth ventricle and around the subarachnoid space.

At distal sites of the subarachnoid space, CSF flows outward through the arachnoid villi into venous blood of the superior sagittal sinus.

Not discussed in this chapter, some CSF drains directly into the lymphatic gland

Taken from Johanson et al, 2005[106]

Figure 3

CEREBROSPINAL FLUID
(apical membrane)

(basolateral membrane)

INTERSTITIAL FLUID or PLASMA ULTRAFILTRATE
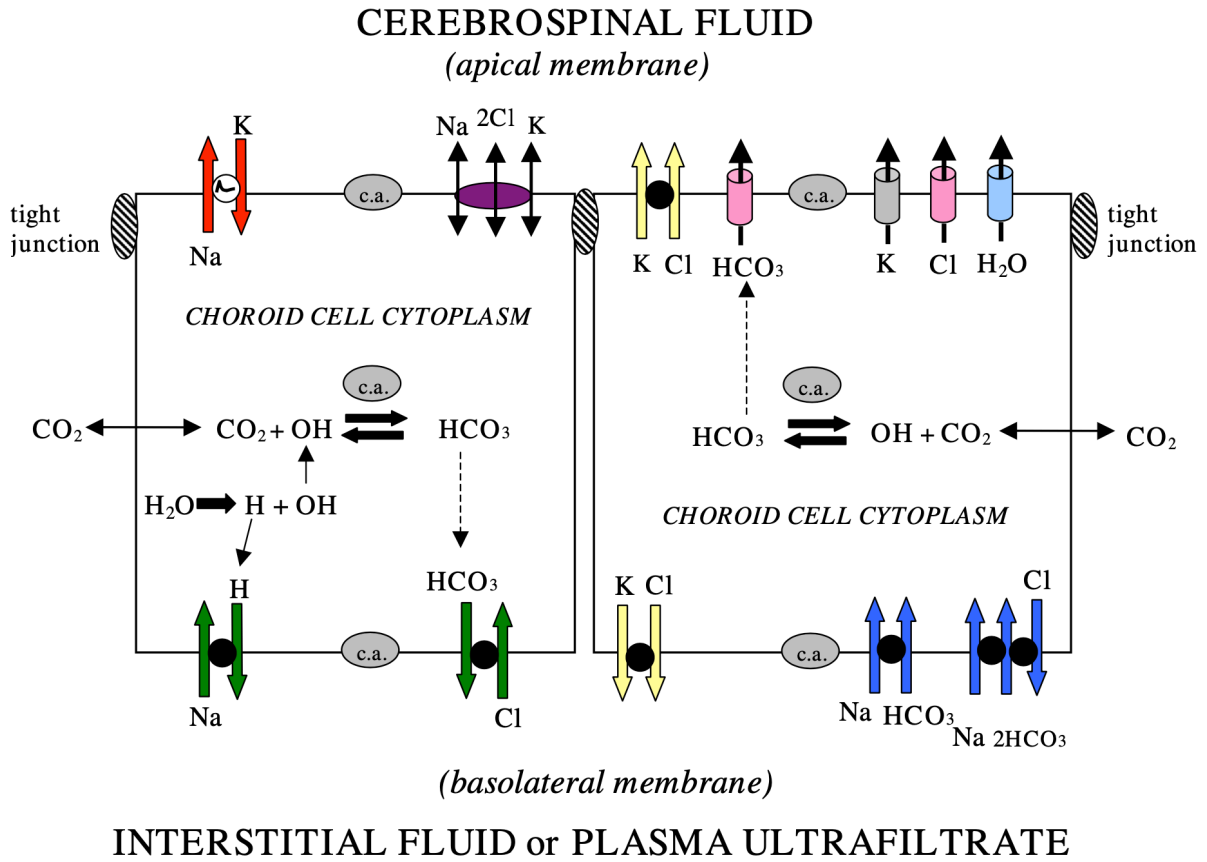
Figure 3: Ion Transporters and Channels in Mammalian Choroidal Epithelium

Coordinated transport of ions across the basolateral membrane, through the epithelial cells, into the ventricles is required for CSF secretion. On the plasma-facing membrane, parallel Na^+-H^+ and Cl^--HCO_3^- exchangers bring Na^+ and Cl^- into cells and pump H^+ and $HCO3^-$ out of the cell, respectively. This favorable Na^+ uptake is due to apical pumping of Na^+ out of the cell, maintaining a low intracellular Na^+ concentration. Na^+/K^+-ATPase is responsible for pumping Na^+ out of the cell, across its concentration gradient, with the use on one ATP molecule. K^+ and Cl^- co-transporters help maintain cell volume. Apical K^+, Cl^- and HCO_3^- channels facilitate the diffusion of these ions into the CSF. Aquaporin channel 1 (AQP1), not depicted here, are found on both the basolateral and apical membranes and mediate water flux into the ventricles.

Taken from Johanson et al, 2008[71]

CHAPTER 2:

The Anti-Proliferative Effects of 3,3'-Diindolylmethane on Human Melanoma Cells with Distinct Mutational Profiles

Abstract

Melanoma, the most aggressive and deadly form of skin cancer, is known for its high mutation rate and intratumor heterogeneity. As a result, melanoma cells confer resistance to all current targeted therapies. 3,3'-diindolylmethane (DIM), a natural phytochemical from cruciferous vegetables, showed strong anti-proliferative effects in multiple cell lines, each with distinct combinations of mutations in oncogenic BRAF and Nras as well as tumor suppressor PTEN and p53. Unlike its monomer, indole-3-carbinol, DIM inhibited proliferation in both wild-type and oncogenic BRAF cell lines by down-regulating the expression of the micropthalmia associated transcription factor, MITF-M, a master regulator of melanocyte differentiation and melanoma development. A corresponding decrease in downstream MITF-M target proteins such as cell cycle regulators, CDK2, CDK4, Cyclin-D as well as anti-apoptotic protein Bcl2 were also detected. Our results implicate this natural compound as a potential candidate for combinatorial treatments with current targeted therapies for human melanoma.

Introduction

Arising from pigment-producing melanocytes, human melanoma is the most aggressive form of skin cancer accounting for only 3% of all skin cancers but responsible for 65% of skin cancer related deaths[6]. This high mortality rate can be attributed to the speed at which melanoma adapts from a surgically removable slow-growing lesion to a highly aggressive metastatic disease, with few therapeutic options. Due to UV-induced DNA damage, melanomas have the highest mutational burden, resulting in many neutral 'passenger' mutations as well as functionally significant 'driver' mutations[107]. Recent advances in sequencing technology have led to the genomic characterization of many cancers based on their driver mutations for better targeted therapies[108]. In melanoma, prominent driver mutations have been identified as activating mutations in proto-oncogenes, BRAF and NRAS, as well as inactivating mutations in the tumor suppressors, PTEN and p53[109].

BRAF and NRAS are both members of the pro-proliferative RAS/RAF/MEK/ERK (MAPK) signaling pathway. Approximately 50% of melanoma patients have mutations in BRAF, with 90% of these mutations substituting valine for glutamic acid at codon 600. This results in a constitutively active BRAFV600E[22]. In recent years, new therapeutics specifically targeting this pro-proliferative pathway have been developed such as Vemurafenib and Dabrafenib, both oncogenic BRAF inhibitors, and Trametinib, a MEK inhibitor[110]. While these therapies initially show significant improvement in progression-free and overall survival, due to the heterogenous property of these tumors, most patients rapidly develop resistance and long-term prognosis is poor[110]. Therefore, there is an urgent need for novel therapeutics targeting alternative signal transduction pathways to be used in conjunction with current BRAF pathway inhibitors to potentially eliminate resistance and recurrence. A prospective novel target is microphthalmia-associated transcription Factor (MITF-M), the master regulator of melanocytes, which is overexpressed in 80% of patients taking BRAF/MEK inhibitors and is known to confer resistance to both BRAF and MEK inhibitors[27].

MITF-M is the melanocyte specific isoform of the microphthalmia-associated transcription factor family, often referred to as the "master regulator" of melanocytes because it controls melanocyte differentiation, migration, proliferation and survival[111]. It is also a driver of melanoma progression and considered to be a melanoma addiction oncogene as a majority of melanomas are reliant on MITF-M for cell survival and maintenance of their malignant phenotype[32,33,112]. MITF-M is expressed in >80% of melanomas, detectable throughout all stages of melanoma development and amplified in approximately 5-20% of human melanomas[33,34]. Thus, MITF-M is an intriguing candidate for new targeted therapies.

One of the many transcriptional regulators of MITF-M is β-catenin. The β-catenin-dependent (canonical) Wnt Signaling cascade is up-regulated in human melanoma and has been shown to drive tumor progression[38]. Alongside increased MITF-M levels, increased β-catenin levels have also been correlated with resistance to BRAF-targeted therapies[28]. Therefore, identifying an inhibitor to the Wnt-signaling pathway to be used in combination with BRAF-specific inhibitors could potentially help overcome therapeutic resistance. Another positive regulator of MITF-M

transcription is BRN2 (N-Oct-3). BRN2 is a neuronal-specific protein that is expressed in melanoblasts but not mature melanocytes. In melanoma cells, BRN2 has been shown to be reactivated and is regulated by oncogenic BRAFV600E[113]. Our lab has previously shown that indole-3-carbinol, a natural phytochemical, down-regulates BRN2 regulation of MITF-M in BRAFV600E melanoma cell lines[114].

Natural phytochemicals have been identified as possible alternative therapeutic agents due to their well-established anticancer roles with minimal side effects[115,116]. 3,3'-diindolylmethane (DIM) is a naturally occurring phytochemical found in cruciferous vegetables of the *Brassica* genus, such as broccoli, brussels sprouts and cauliflower. This indole compound is a stable dimer formed by the self-condensation of indole-3-carbinol (I3C) in acidic environments such as the gut[117]. DIM has been shown to have multiple anti-carcinogenic and anti-tumorigenic properties including inhibiting proliferation in many human cancers including prostate, breast, colon, ovary and pancreatic[118]. In this study, we observed that human melanoma cell lines with distinct mutational profiles were sensitive to the anti-proliferative effects of DIM in a dose-dependent and time-dependent manner. DIM induced cell cycle arrest by down-regulating protein and transcriptional expression of MITF-M, thereby down-regulating the protein expression of critical cell-cycle genes. A decrease in β-catenin protein expression and *in-silico* modeling alludes to DIM regulation of MITF-M expression through the canonical Wnt signaling pathway suggesting that this natural phytochemical could be a promising component for combination therapies for human melanoma.

Materials and Methods

Cell Culture:

Melanoma cell lines G-361 and SK-MEL-2 were purchased from American Type Culture Collection (ATCC), and were authenticated according to the ATCC guidelines. A375 and DM738 melanoma cells were acquired from the tissue culture facility at University of California, Berkeley. The G361 melanoma cells were cultured in Modified McCoy's 5A cell media (Invitrogen, 16600-082) supplemented with 10% fetal bovine serum (VWR, 45000-734), 2 mM L- glutamine (Fischer-Scientific, 25030-081), and 2.5 ml of 10,000 U/ml penicillin/streptomycin mixture (Invitrogen, 10378-016). A375, DM738 and SK-MEL-2 melanoma cells were cultured in DMEM containing 4.5 g/L Glucose, 114 mg/L Sodium Pyruvate, and 2 mM L-glutamine, supplemented as described above. Cells were grown in a humidified chamber at 37°C containing 5% CO_2.

Treatment with 3,3'-Diindolylmethane, Lupeol, Pristimerin and Ursolic Acid

3,3'-Diindolylmethane was purchased from Sigma-Aldrich (D9568). Lupeol, Pristimerin and Ursolic Acid were all purchased from Cayman Chemical (11215, 13621, 10072, respectively) 1000X stock solutions were made in 99.9% HPLC grade dimethyl sulfoxide (DMSO, Sigma Aldrich) and then diluted to 1X in media before being added to the plate. To study the effects of this compounds, cells were treated with or without indicated concentrations of each compound every 24 hours for 72 hours and harvested at 24, 48 and 72 hours for western blot.

Cell Proliferation Assay:

To look at cell viability for DIM treated cells, cells were plated onto 24-well tissue culture plates at 70% confluency and treated as indicated in triplicate with DMSO vehicle control for 48 hours. Inhibition of proliferation was measured using a standard Cell Counting Kit-8 (Dojindo, CK04) as per manufacturer's instructions. Briefly, 50µL of the CCK-8 solution was added to each well along with 450µL of full media and incubated for 2.5 hours. Absorbance was read at 450nm and percent viability was calculated by standardizing the average of each treatment triplicate to the average value of the vehicle control. For cell viability assays with Lupeol, Pristimerin, and Ursolic Acid treated cells, cells were plated in 96-well tissue culture plates, treated as indicated in triplicate with DMSO vehicle control for 48 hours. Inhibition of proliferation was then measure with Vybrant MTT Cell Proliferation Kits (ThermoFisher, V13154) as per manufacturer's instructions. Briefly, 10µL of the 12mM MTT stock solution (5mg MTT reagent in 1mL sterile PBS) was added to 100µL fresh media. Cells were incubated at 37°C for 2-4 hours depending on confluency of cells. 100µL SDS-HCl solution (1g SDS in 10mL of .01M HCl) was added and plates were incubated again at 37°C overnight. Absorbance was read 14-16 hours later

at 570nm and percent viability was calculated by standardizing the average of each treatment triplicate to the average value of the DMSO vehicle control.

Flow Cytometry Analysis of DNA content:

Melanoma cells were plated in triplicate onto six-well plates at 70% confluency and treated with the indicated concentrations of DIM for 48 hours. The DNA content of propidium iodide stained nuclei from harvested cells was determined by flow cytometry. Briefly, cells were hypotonically lysed in 300 mL of DNA staining solution (0.5 mg/mL propidium iodide, 0.1 % sodium citrate, and 0.05 % Triton-X 100). Emitted fluorescence from the nuclei of wavelengths more than 585 nm was measured with a Coulter Elite instrument with laser output adjusted to deliver 15 mW at 488 nm. For each sample, 10,000 nuclei were analyzed and the percentage of cells in G_1, S, and G_2/M phases of the cell cycle was determined by analysis with the Multicycle computer program provided by Phoenix Flow Systems in the Cancer Research Laboratory Microchemical Facility of the University of California, Berkeley.

Western Blot Analysis:

After indicated treatments, G361 and SK-MEL-2 cells were washed with phosphate buffered saline (PBS, Lonza) and harvested in 1mL PBS. Cells were subsequently pelleted by centrifugation and re-suspended in Radioimmunoprepicitation assay buffer (RIPA, (50mM Tris pH 8.0, 150 mM NaCl, 0.1% SDS, 0.1% NP-40, and 0.5% Sodium Deoxycholate) containing protease inhibitors (50µg/mL phenylmethysulfonyl fluoride, 10 µg/mL aprotinin, 5 µg/mL leupeptin, 0.1 µg/mL NaF, and 10 µg/mL β-glycerophosphate). Samples were centrifuged once more and the supernatant was collected and placed into fresh tubes. Protein concentration were determined using Pierce Bradford Protein Assay Kit (ThermoFisher, 23200). 30µg of protein was mixed with sample buffer [25% glycerol, 0.075% SDS, 1.25 ml β-mercaptoethanol, 10% bromophenol blue, 3.13% 0.5 M SDS, and 0.4% SDS (pH 6.8)], and fractionated on 12% polyacrylamide gels. A pre-stained protein ladder (Fisher Scientific 26619) was used as reference for size. Proteins were transferred electrically to nitrocellulose membranes for 1hr at 4°C. Blots were then incubated for 1h in 5% nonfat dry milk dissolved in PBST, washed and then incubated overnight at 4°C in antibodies diluted in PBST. ECL Lightening reagents were used to visualize the primary antibody bound protein bands in nitrocellulose membranes and the results captured on ECL Autoradiography Film (GE Healthcare). The western blots employed the following primary antibodies: mouse anti-MITF-M (Thermo- scientific), mouse anti-HSP 90 (BD Biosciences), mouse anti-CDK2, rabbit anti-CDK4, mouse anti-β-catenin (Santa Cruz), mouse anti-Cyclin D1 and rabbit anti-Bcl2 (Cell signaling).

RT-PCR and qPCR analysis:

Total RNA was extracted from harvested cells using TRIzol reagent (Invitrogen, 15596018) and spectrophotometrically quantified by absorbance at 260 nm. Reverse transcription (RT) reactions were carried out using RT-MMLV reverse transcriptase (Invitrogen) and the cDNA was used for PCR reactions using .5µM of the following primers: MITF-M forward 5' - CCG TCT CTC ACT GGA TTG GT - 3', MITF-M Reverse 5' – TAC TTG GTG GGG TTT TCG AG - 3' GAPDH forward, 5' – TGA ACG GGA AGC TCA CTG G – 3' and reverse, 5' – TCC ACC ACC CTG TTG CTG TA – 3'. PCR conditions were as follows: 30s at 94°C, 30s at 55°C and 30s at 72°C for 28 cycles. PCR products were electrophoretically fractionated in 2 % agarose gels containing 0.01% Gel Red (Biotium) for DNA staining along with 1kb plus DNA ladder and further visualized using a Protein Simple FluorChem machine. For quantitative, real-time PCR, cDNA was diluted and used for real-time qPCR using the Power Eva qPCR SuperMix Kit (Biochain, K5057400) following the manufacturer's protocol. qPCR was performed on the StepOne PCR system (Applied Biosystems) and analyzed with the $\Delta\Delta C_t$ method, as supplied by the manufacturer (Applied Biosystems). GAPDH gene expression was used for internal normalization.

In Silico **Computational Simulations** – performed by Jeanne Quirit

The structures Wnt8 were obtained from the Protein Data Bank. The PRODRG server was used to produce the topology files for modeling DIM. The protein and ligand (DIM) structures were subsequently loaded into the Hex Protein Docking program. Prior to docking the structures, all water molecules and hetero molecules were manually removed by editing each PDB file. Shape and electrostatics were used as restrictive parameters to model binding between the receptor and ligand. Modeling results were visualized using PyMol. The program LigPlot was then used to generate schematic diagrams that illustrate the pattern of interactions between the 3-D coordinates of the protein and bound ligand.

Results

Anti-proliferative effects of 3,3'-diindolylmethane on human melanoma cells with distinct mutational profiles.

Initially, the anti-proliferative effects of DIM were examined in four human melanoma cell lines, each displaying distinct mutational profiles (Figure 1E). A375, G361, DM738 all express an oncogenic BRAFV600E mutation while SK-MEL-2 expresses the wild-type BRAF. However, SK-MEL-2 does have a mutation in the MAPK pathway, expressing mutant NRAS. DM738 and SK-MEL2 cells each express at least one mutation in the tumor suppressors, PTEN and p53. None of the four cell lines have the same combination of mutations. This was carefully chosen in order to determine the pleiotropic effect of DIM.

Each melanoma cell line was treated with varying concentrations of DIM for 48 hours. A standard MTT assay was then used to measure cell proliferation (Figure 1A-D). Cells treated with only the DMSO vehicle control represent the 100% cell viability for each cell line. The results indicate that all four cell lines, despite their unique mutational backgrounds, are sensitive to treatment with DIM and show significant decrease in cell proliferation with increasing concentration of DIM. There was no strong correlation between the overall mutagenic profiles of these four cell lines and their sensitivity to the anti-proliferative effects of DIM. A375, G361 and DM738 cells all express the constitutively active BRAF-V600E mutation, a mutation that occurs in over 50% of melanoma cells, while SK-MEL-2 cells express the wild-type form of BRAF. Indole-3-carbinol (I3C), the monomer of DIM, has been shown to bind to and inhibit the kinase activity of BRAF-V600E in these melanoma cells but not that of wild-type BRAF [114]. The structures of I3C and DIM are shown in Figure 1F. SK-MEL-2's responsiveness to the effects of DIM, and not I3C, indicates that the dimer could have a different target in these melanoma cells than its monomer. Therefore, G361 and SK-MEL-2 were used and compared throughout our study.

DIM induces G1 cell cycle arrest in G361 but not SK-MEL-2 cells within 48 hours

To further characterize the anti-proliferative effects of DIM on these cells, changes in the cell cycle were observed using flow cytometry analysis of propidium iodine stained nuclei. In G361 cells, treatment with DIM resulted in a noticeable dose dependent increase in cells with G1 phase DNA and decrease in S phase DNA, indicating a G1 cell cycle arrest (Figure 2A). This was not observed with SK-MEL-2 cells (Figure 2B). The percent of cells in G1 for SK-MEL-2 in the DMSO vehicle control treated cells is higher than that of the G361 cells (61% and 52% respectively). This is most likely due to the slower proliferative nature of SK-MEL-2 cells than that of G361 cells. The doubling time of SK-MEL-2 cells is approximately 56 hours while G361 cells have a doubling time closer to 12 hours[119,120].

DIM downregulates key cell cycle regulators through downregulation of MITF-M

The master regulator, MITF-M, activates several critical melanoma signaling pathways by directly regulating genes involved in cell cycle progression, such as CDK2, CDK4 and cyclin D as well as inhibition of apoptosis, such as Bcl2. We therefore tested whether DIM induced cell cycle arrest results in a loss of MITF-M expression in G361 cells but not SK-MEL-2 cells. Surprisingly, treatment with 35μM DIM over the course of 72 hours showed a time-dependent decrease in MITF-M protein levels in both G361 and SK-MEL-2 cells (Figure 2A, 2B). However, it is important to note, SK-MEL-2 cells express 50% less MITF-M protein than G361 cells (Figure 2C, 2D). It is most likely this difference in expression levels that accounts for their proliferative differences as MITF-M levels are directly correlated with proliferative capacity[36]. Even though SK-MEL-2 cells did not exhibit clear cell cycle arrest at 48 hours, there is still a time-dependent decrease in protein expression of the cell cycle regulators, CDK2, CDK4 and cyclin D. This decrease is also observed in the G361 cells.

Transcriptional Regulation of MITF-M by DIM in G361 cells potentially through β-catenin signaling pathway
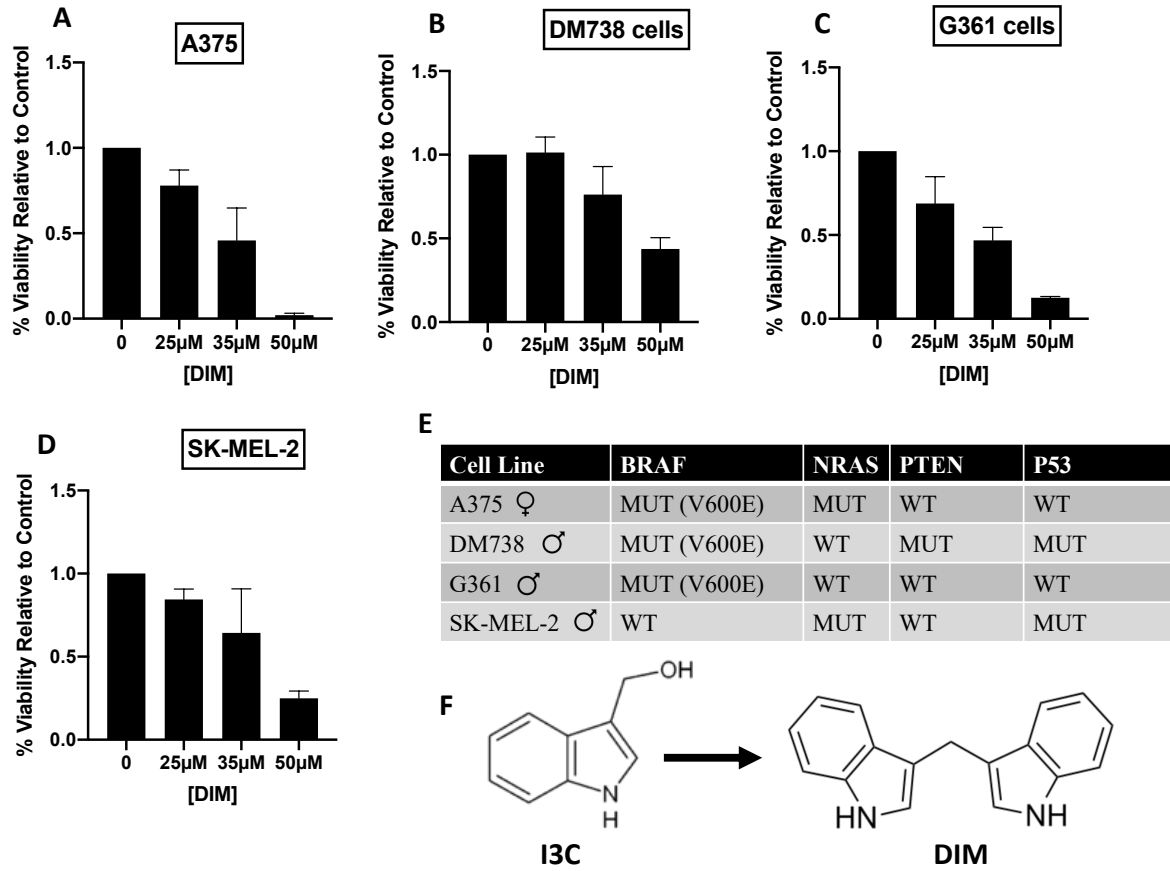
MITF-M activity is regulated on transcriptional, post-transcriptional and post-translational levels. To determine if DIM is modulating MITF-M on the transcriptional or post-transcriptional level, we looked at mRNA expression of MITF-M with or without treatment of 35μM DIM over the course of 72 hours. As shown in Figure 4A, mRNA transcript levels decreased in the presence of DIM in a time-dependent manner. This decrease was reconfirmed using quantitative PCR (Figure 4B). MITF-M mRNA transcripts decreased 60% over the 72 hour treatment with 35μM DIM. Many proteins transcriptionally regulate MITF-M through direct binding to the MITF-M promoter. One such protein, β-catenin, binds to the MITF-M promoter through a TCF/LEF-1 binding site. Increased nuclear translocation of β-catenin has been shown to promote cell proliferation in many cancers, including melanomas. Therefore, we tested if DIM affected the Wnt/ β-catenin pathway. Western blots performed on G361 cells treated with DIM revealed that β-catenin protein levels were significantly downregulated. β-catenin therefore cannot enter the nucleus to transcriptionally regulate MITF-M (as depicted in Figure 4E). Lastly, *In-silico* modeling predicted a potential binding site for 3,3'-diindolylmethane on the Wnt8 growth factor itself while bound to its receptor Frizzled (Figure 4D). Wnt8, the *Xenopus* variant of the wnt protein, was used for the *in-silico* modeling as the crystallized structure of mammalian wnt3 was not available. However, the general architecture of wnt8 and wnt3 is effectively the same[121].

Triterpenoids, another class of natural phytochemicals, also exhibit anti-proliferative effects on human melanoma cells.

The anti-proliferative effects of three triterpenoids, Lupeol, Pristimerin and Ursolic acid, were examined in three human melanoma cell lines. Each melanoma cell line was treated with varying concentrations of each compound for 48 hours. A standard MTT assay was then used to measure cell proliferation (Figure 5A-C). Cells treated with only the DMSO vehicle control represent the 100% cell viability for each cell line. All three cell lines were very responsive to low

concentrations (1µM & 10uM) of pristimerin (Figure 5B). However, none of the cell lines were responsive to those same concentrations of Lupeol. Unfortunately, Lupeol is incredibly insoluble and higher concentrations were not attainable. G361 and DM738 cells were responsive to Ursolic Acid (UA), while A375 cells were not (Figure 5C). G361 had the most dramatic response to 25µM UA, with cell viability around 5% relative to DMSO control while DM738 still had 60% cell viability. All three compounds are structurally very similar but come from a wide variety of fruits and plants (figure 5D). The ability to inhibit cell proliferation in many melanoma cell lines, each with diverse mutational profiles, is a unique characteristic of DIM, and therefore DIM could be a potential therapeutic to target the large heterogeneity in human melanoma tumors.

Figure 1

A A375

B DM738 cells

C G361 cells

D SK-MEL-2

E

Cell Line	BRAF	NRAS	PTEN	P53
A375 ♀	MUT (V600E)	MUT	WT	WT
DM738 ♂	MUT (V600E)	WT	MUT	MUT
G361 ♂	MUT (V600E)	WT	WT	WT
SK-MEL-2 ♂	WT	MUT	WT	MUT

F

I3C → DIM

Figure 1: Effects of 3,3'—Diindolylmethane on the proliferation of melanoma cell lines with distinct mutational profiles

A-D) Human melanoma cell lines (A375, DM738, G361 and SK-MEL-2) displaying different genotypes (see E) were treated with the indicated concentrations of 3,3'-diindolylmethane (DIM) for 48 hours. Cell proliferation was measured using a CCK-8 assay relative to the DMSO vehicle control.

(F) The structures of I3C and DIM

Figure 2

Figure 2

35
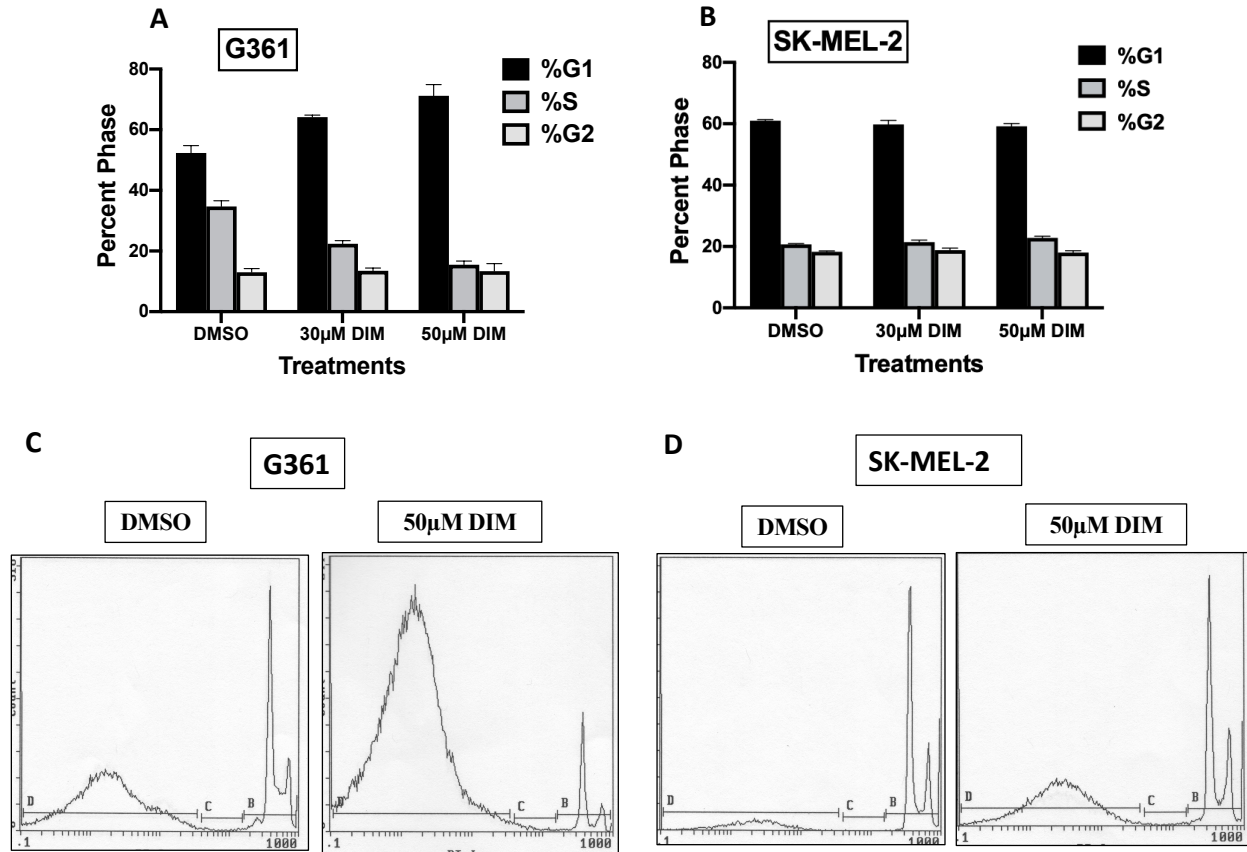
Figure 2: Cell – cycle effects of DIM on G361 and SK-MEL-2 cells

G361 cells (A) or SK-MEL-2 cells (B) were treated with 30μM and 50μM DIM for 48 hours. Cells were harvested and stained with a hypotonic solution containing propidium iodide. DNA content was quantified by flow cytometry.

(C, D) The histograms of representative experiments from three independent experiments are shown for each cell line

Figure 3

37
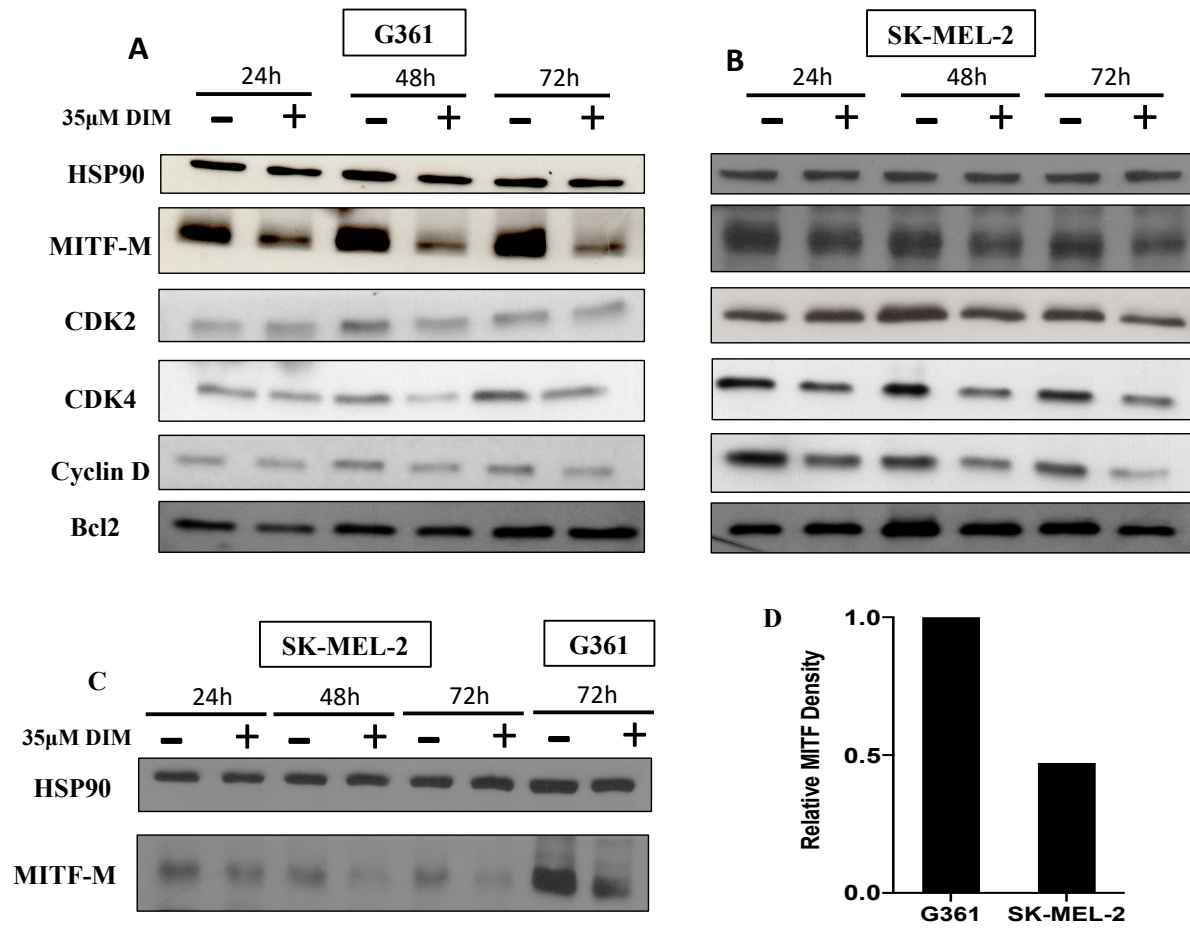
Figure 3: DIM regulation of MITF-M and downstream targets:

A, B: G361 and SK-MEL-2 cells were treated with or without 35μM DIM over a 72 hour time course. Total cell lysates were fractionated by SDS-poylacrylamide electrophoresis and levels of MITF-M, CDK2, CDK4, Cyclin D and BCl2 were determined by western blot.

C: Western blot comparison of MITF-M expression levels in SK-MEL-2 and G361 cells

D: Densitometry of 72 hour (DMSO treated) SK-MEL-2 and G361 MITF levels relative to their hsp90 loading controls

Figure 4

A   G361 RT-PCR

	24h	48h	72h
35µM DIM	– +	– +	– +

MITF-M

GAPDH

B   G361 qPCR

■ DMSO
▨ 35µM DIM

MITF relative fold change

1.5
1.0
0.5
0.0

24hrs   48hrs   72hrs

C   G361 WB

	24h	48h	72h
35µM DIM	– +	– +	– +

β-catenin

HSP90

D

E

INACTIVE   ACTIVE   INACTIVE

Frizzled Receptor   GSK3β   GSK3β

β-cat   β-cat P

LEF1 → MITF   LEF1 → MITF   LEF1 → MITF
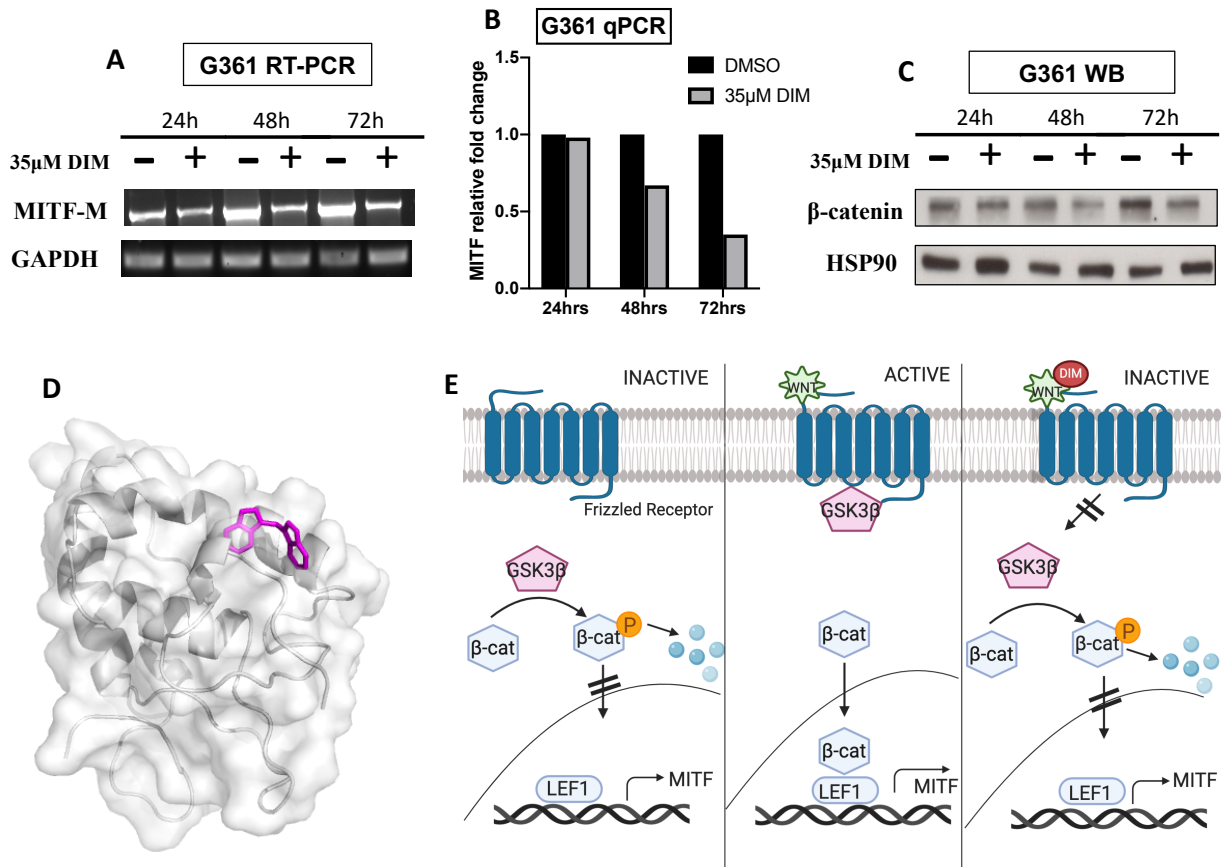
Figure 4: Transcriptional regulation of MITF-M by 3,3'-diindolylmethane through β-catenin pathway

(A) MITF-M transcript expression in G361 cells treated with or without 35μM DIM over a 72 hour time-course was determined by RT-PCR analysis

(B) MITF-M transcript expression in G361 cells treated with or without 35μM DIM over a 72 hour time-course was determined by quantitative PCR (qPCR) analysis

(C) β-catenin protein levels were determined in G361 cells treated with or without 35μM DIM over a 72 hour time-course by western blot

(D) Predictive binding simulations of DIM interactions with the Wnt8 ligand bound to the frizzled receptor analyzed using PyMol program (Courtesy of Jeanne Quirit)

(E) Diagram depicting predicted mechanism of action for DIM on β-catenin protein levels and subsequent MITF-M transcript expression

Figure 5

A. Lupeol

B. Pristimerin

C. Ursolic Acid

D.

Compound	Source
Lupeol	Mangoes
Ursolic Acid	Fruit peels and spices such as rosemary, thyme & oregano
Pristimerin	Thunder god vine
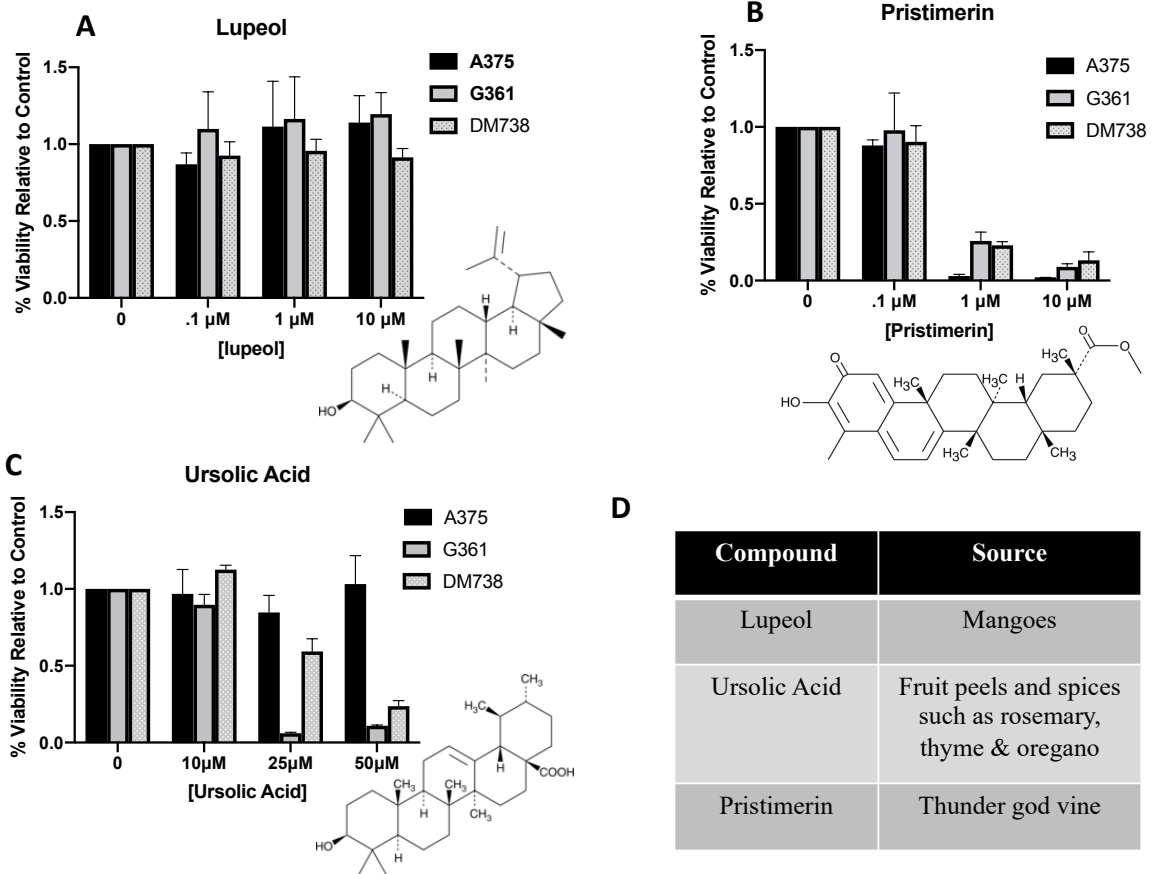
Figure 5: Effects of other natural phytochemicals on melanoma cells with distinct mutational profiles

Human melanoma cell lines (A375, DM738, G361) displaying different genotypes were treated with the indicated concentrations of Lupeol (A), Pristimerin (B) and Ursolic Acid (C) for 48 hours. Cell proliferation was measured using a CCK-8 assay relative to the DMSO vehicle control.

(D) Table describing sources for each natural phytochemical

Discussion

While the anti-cancer effects of cruciferous vegetables have been known for centuries, recent physiological and epidemiological studies have associated these anti-cancer effects to indole-3-carbinol (I3C), a bioactive hydrolysis product of the glucobrassicin found in cruciferous vegetables, and its natural condensation product, 3,3'-diindolylmethane (DIM)[47,115,116,122]. Due to its instability in acidic environment such as the gut, I3C readily self-condenses to DIM and as a result DIM is predominantly detected in the plasma and urine of individuals consuming I3C and cruciferous vegetables, respectively[123,124]. Previously our lab showed I3C inhibited cell proliferation in human melanoma cells expressing BRAFV600E only by binding directly to and inhibiting its enzymatic activity[125]. To determine if this effect was due, in fact, to I3C and not its condensation product DIM, we treated human melanoma cells with increasing concentrations of DIM for 48 hours. We discovered that, unlike I3C, the effects of DIM were not dependent on the mutational profiles of these cells, as four melanoma cell lines with individual combinations of the most common melanoma driver mutations, BRAF, NRAS, PTEN, and p53, were all responsive to DIM in a dose-dependent manner.

Melanoma, one of the most aggressive malignancies, is characterized by its high molecular heterogeneity which is mostly due to long-term exposure of these cells to UV-radiation, a strong external mutagen. Recent advances in next-generation sequencing have significantly increased our understanding of the evolution of mutations and the resulting heterogeneity within an individual tumor. Intratumor heterogeneity has profound implication for targeted therapies such as Vemurafenib and Trametinib. These inhibitors exploit melanoma's dependence on the critical pro-proliferative RAS/RAF/MEK/ERK pathway and have significantly improved overall survival[126]. However, due to the heterogeneity of melanoma, most patients become resistant to these targeted treatments within a couple of months[25]. Therefore, targeting melanoma cells through multiple pathway simultaneously can reduce the likelihood of resistance by synergistically eradicating the various clones that emerge from that tumor. DIM's ability to inhibit proliferation in many melanoma cell lines regardless of their mutational profiles validates it as a potential compound for combinatorial treatment.

Since our results demonstrated all four cell lines were equally responsive to DIM, we singled out G361 (BRAFV600E) cells and SK-MEL-2 (WT BRAF) cells to further compare the effects of I3C and DIM. As previously reported, treatment with I3C decreased the protein expression of MITF-M, the master regulator of melanocytes, in G361 cells, while increasing it in SK-MEL-2 cells[125]. Interestingly, treatment with DIM showed a decrease in MITF-M protein expression as well as a decrease in the down-stream cell cycle regulators in both G361 and SK-MEL-2 cell lines. It is important to note that G361 and SK-MEL-2 cells differ not only in their BRAF status but also in their MITF-M expression levels. MITF-M is known to follow a 'rheostat model' in which highly elevated expression of MITF-M leads to increased differentiation and cell cycle

arrest, whereas continued moderate levels of MITF-M expression signal melanoma cell survival and proliferation and low levels are linked with apoptosis or cell-cycle arrest[127]. MITF-M is expressed 50% less in SK-MEL-2 cells than G361 cells. This can be attributed to the origin of each cell line. G361 cells were derived from the primary site of a malignant melanoma while SK-MEL-2 cells were derived from a metastatic site[128,129]. G361 cells express moderate MITF-M levels corresponding with a proliferative phenotype, and a doubling time of 12 hours[119], while SK-MEL-2 cells express lower MITF-M levels corresponding with a less proliferative phenotype and a more invasive phenotype, further confirmed by their 56-hour doubling time[120]. Vehicle control treated SK-MEL-2 cells exhibited a larger percentage of cells in G_1 indicating more cells were in a G_1 cell-cycle arrest than the G361 cell population. However, due to their slower doubling time, unlike G361 cells, an increase in cell cycle arrest was not apparent within 48 hours of DIM treatment. Regardless of this, MITF-M protein expression decreased after treatment with 35μM DIM in a time dependent manner. Many proteins regulate the expression of MITF-M, however only such regulator has expression levels that correspond with the MITF rheostat. β-catenin protein expression has been linked to phenotype switching in melanoma cells as high levels of β-catenin correlate with a more proliferative phenotype while low amounts correlate with the more invasive phenotype[38].

The canonical Wnt/β-catenin signaling pathway plays an integral role in the development of neural crest cells, melanocyte lineage-specific differentiation and expansion, and has been strongly implicated in melanogenesis[130,131]. In the absence of Wnt signaling, β-catenin is phosphorylated by glycogen synthase kinase (GSK3β) and immediately degraded. When the Wnt ligand binds to its receptor, Frizzled, it sequesters and inactivates GSK3β, stabilizing β-catenin levels in the cell and increasing transcription of downstream target genes, such as MITF-M.

β-catenin is known to drive proliferation of melanoma cells through its regulation of MITF-M expression. We therefore examined the protein expression of β-catenin after treatment with DIM. DIM decreased β-catenin protein levels in the highly proliferative G361 cells in a time-dependent manner following DIM treatment. *In silico* modeling suggests a binding site for DIM on the Wnt ligand when it is bound to its receptor, frizzled. It is therefore plausible that DIM could be inhibiting Wnt ligand activation, thereby keeping GSK3β active, resulting in the degradation of β-catenin protein. However, more studies are needed to validate and confirm this assumption.

Natural dietary phytochemicals represent a large group of potential anti-cancer agents with minimal side effects. Using these in combination with current melanoma targeted therapy to create an anti-cancer drug "cocktail" could potentially counter the development of drug resistance by hitting multiple pathways without increasing toxicity. Since MITF-M is over-expressed in 80% of patients taking BRAF/MEK inhibitors and is known to confer resistance to these inhibitors, a "cocktail" combination of DIM with Vermurafenib or Trametinib would target multiple critical pathways, thereby helping overcome resistance without added side effects.

Another class of natural phytochemicals with known anti-cancer effects are triterpenoids, comprising the largest group of natural products from plants with over 20,000 known members[61]. We tested the effects of three triterpenoids, lupeol, pristimerin, and ursolic acid, on three melanoma cell lines with distinct mutational profiles. While structurally very similar, each compound exhibited distinct effects on the melanoma cell lines. Lupeol, known for its anticancer effects in colon, prostate and breast cancer[57], exhibited zero effect on any of the three melanoma cell. Ursolic acid, shown to inhibit breast cancer cells[132], exhibited anti-proliferative effects in some but not all the melanoma cells. Pristimerin, a potent anticancer agent with effects in a wide range of cancers[60], showed anti-proliferative effects on all three cell lines independent of their mutational background. DIM and pristimerin could therefore be great candidates to use in combination with targeted therapies, as they are not dependent on the presence of specific mutations in order to exert their anti-proliferative effects.

Chapter 3:

Receptor-Independent Activation of the Inwardly-Rectifying Potassium Channel, K_{ir}7.1 by Progesterone in Choroid Plexus and Retinal Epithelial Cells

Abstract

The choroid plexus (CP) epithelium secretes cerebrospinal fluid (CSF) and plays an important role in healthy homeostasis of the brain. While the steroid hormone progesterone is known to regulate water flux in the brain, the molecular mechanism is not known. Here, using whole-cell patch clamp recordings from male and female murine CP cells, we showed that application of progesterone resulted in strong potentiation of the inwardly rectifying potassium channel $K_{ir}7.1$, an essential protein needed for survival. The potentiation was progesterone-specific and independent of other known membrane progesterone receptors expressed in CP. This effect was recapitulated with recombinant $K_{ir}7.1$, as well as with endogenous $K_{ir}7.1$ in the retinal pigment epithelium. Current clamp studies further showed a progesterone-induced hyperpolarization of CP cells. Because $K_{ir}7.1$, together with the Na^+/K^+-ATPase, is indicated as the main regulator of epithelial ion homeostasis, our results provide evidence of a progesterone-driven control of tissues in which $K_{ir}7.1$ is expressed.

Introduction

Situated in each of the four ventricles, the choroid plexus (CP) constitutes an important barrier between the peripheral blood plasma and the brain. The CP consists of a single layer of cuboidal epithelial that line a complex network of capillaries and are primarily responsible for producing cerebrospinal fluid (CSF)[64,74]. CSF has many roles in the central nervous system. It provides support and acts as a mechanical buffer while also providing nutrients and removing waste products from the brain[68]. Tight junctions in the CP epithelium form a barrier between the blood plasma and the CSF, which allow channels and transporters in the CP to establish a highly regulated concentration gradient of ions between the two fluids. Located on the luminal side of the epithelium, the Na^+/K^+ -ATPase transporter drives secretion of sodium ions and influx of potassium ions, which is, in turn, counteracted by the activity of several potassium channels[64]. The ion flux generated by these channels then stimulates opening of the water channel AQP1[64] and ensures regulation of CSF production. Therefore, identification of the physiological regulators of CP potassium channels is essential to better understand the mechanism behind the healthy ion homeostasis and production of CSF. One such potential regulator is the steroid hormone progesterone (P4), the levels of which were shown to correlate with ventricular size during the female menstrual cycle[133] and pregnancy[134]. Interestingly, the expression of the genomic progesterone receptor in CP is almost negligible, while the tissue keeps responding to progesterone regulation[135,136]. Additionally, P4 has been shown to exert a neuroprotective role during brain trauma[94,97,137]. Since P4 is known to regulate ion channels through non-genomic steroid signaling[138,139], we explored whether P4 could modulate ion channels in the CP in a similar manner. To determine non-genomic signaling events, patch-clamp experiments were performed on primary cultures of murine CP cells, isolated from the lateral ventricles. These experiments revealed the inwardly rectifying potassium channel $K_{ir}7.1$, localized to the luminal side of the CP epithelium, to be the major ion channel in CP potentiated by P4 via a GPCR-independent mechanism. $K_{ir}7.1$ is vital for mammalian physiology, as mice deficient in $K_{ir}7.1$ die shortly after birth[140]. The potentiation of $K_{ir}7.1$ by P4 was confirmed in electrophysiological measurements of HEK293 cells expressing a recombinant $K_{ir}7.1$, as well as in $K_{ir}7.1$ recordings from retinal pigment epithelium (RPE) - another epithelial tissue with similar ion channel expression as the CP. Our results point to a novel unexpected regulation of $K_{ir}7.1$ by the steroid hormone progesterone in two tissues: CP and RPE. Other tissues in which $K_{ir}7.1$ was found, i.e. the uterus[141] may, therefore, be subjected to the same physiological regulation. Additionally, our results may explain how choroid plexus physiology is regulated by the female steroid hormone progesterone in a non-genomic manner.

Materials and Methods

Ethics statement

The C57Bl/6N (Charles River) mice and the *Abhd2* knockout mice of similar background were kept at the Animal Facility of the University of California, Berkeley, in a room with controlled light (14 hours light, 10 hours darkness) and temperature ($23 \pm 0.5°C$). The mice were fed a standard chow diet (PicoLab Rodent diet 20, LabDiet, 5053) and hyper-chlorinated water *ad libitum*. All experiments were performed in accordance with NIH Guidelines for Animal Research and approved by UC Berkeley Animal Care and Use Committee (AUP 2015-07-7742), with every effort made to minimize suffering for the animals. A thorough description of how the *Abhd2* full knockout mouse line was generated is provided elsewhere[142].

mRNA library preparation and sequencing

For gene expression analyses of the choroid plexus (CP), the lateral CPs from 3 adult male and 3 adult female of either *Abhd2*^{+/+} or *Abhd2*^{-/-} genotype were dissected out and snap frozen. The animals were euthanized by CO_2 followed bycervical dislocation. This procedure was performed in the mornings when the females were in proestrus. mRNA isolation was performed using the Quick-RNA Microprep Kit (Zymo Research, R1050) according to the manufacturer's instructions. The mRNA samples were processed for sequencing at QB3 Vincent J. Coates Genomics Sequencing Laboratory, UC Berkeley. The CP mRNA was enriched for using Oligo dT beads from the Invitrogen Dynabeads mRNA Direct kit (61005). Subsequent library preparation steps of fragmentation, adapter ligation, and cDNA synthesis were done on the enriched mRNA using the KAPA RNA HyperPrep kit (Roche, KK8540). Truncated universal stub adapters were used for ligation, and indexed primers were used during PCR amplification to complete the adapters and to enrich the libraries for adapter-ligated fragments. Samples were checked for quality on an AATI (now Agilent) Fragment Analyzer. Libraries were then quantified using qPCR on a BioRad CFX Connect to measure molarity of only sequence-able molecules using the Kapa Biosystems Universal Illumina quant kit (KK4824), pooled equimolar, clustered at 3nM with 2% PhiX v3 control library spike-in, and sequenced as a 100bp paired end run on an Illumina HiSeq 4000. Bcl files were then converted to fastq format and demultiplexed using the innate bcl2fastq v1.19 software.

Data analysis

The sequencing results were analyzed by Novogene. Reference genome and gene model annotation files were downloaded from the genome website browser (NCBI/UCSC/Ensembl) directly. Indexes of the reference genome was built using STAR and paired-end clean reads were aligned to the reference genome using STAR (v2.5) and the method of Maximal Mappable Prefix (MMP). HTSeq v0.6.1 was used to count the read numbers mapped of each gene.

Thereafter, fragments per kilobase of exon model per million reads mapped (FPKM) of each gene was calculated based on the length of the gene and reads count mapped to this gene[49]. Differential expression analysis between the four groups (*Abhd2*^{+/+} and *Abhd2*^{-/-} male vs. *Abhd2*^{+/+} and *Abhd2*^{-/-} female, three biological replicates per condition) was performed using the DESeq2 R package (2_1.6.3). The resulting *p*-values were adjusted using the Benjamini and Hochberg's approach for controlling the False Discovery Rate (FDR). Genes with an adjusted *p*-value < 0.05, found by DESeq2, were assigned as differentially expressed.

Lateral choroid plexus cell culture

The lateral CPs from two animals of similar age were used for each cell culture. Animals were euthanized by CO_2 followed by cervical dislocation and the sheets of CPECs were dissected out from the lateral ventricles into 37°C growth media (high glucose DMEM with L-Glutamine (ThermoFisher, 11965092), 10% Fetal bovine serum (FBS, X&Y Cell Culture, FBS-500-HI), 1% Penstrep (Fisher Scientific, 15140-122)), after which the CPs were transferred into 37°C Dulbecco's phosphate buffered saline (DPBS without Ca^+ and Mg^+ (ThermoFisher, 14190144)). Enzymatic dissociation of cells from the CP sheets was performed as previously described[143], with some minor modifications. The CP sheets were broken up by incubation with Pronase (0.1mg/ml in DPBS, Sigma, 10165921001) at 37°C for 30 min. The reaction was inhibited by adding a 5x volume of DPBS after which the cells were allowed to sediment. The cell pellet was further dissociated by trituration in 37°C TrypLE Express (ThermoFisher, 12605010). After the cell clusters had sedimented, the supernatant was transferred to a 5x volume of fresh growth media. The trituration was repeated x5 until only minor cell aggregates remained. The CPECs were washed in growth media by centrifugation at 800 x g for 5 min, resuspended in fresh growth media and plated on Poly-D-Lysine and Laminin (Cell Applications Inc., 127) coated 5mm glass coverslip in a 96-well plate. The cells were allowed to attach to the coverslip for 3 hours at 37°C and 5% CO_2 prior to electrophysiology measurements.

Retinal pigment epithelium cell culture

The RPE cells from two animals of similar age were used for each cell culture. The eyes were processed as previously described[144]. In brief, the eyes were isolated and incubated in 2% Dispase II (Sigma, D4693) in high glucose DMEM, without glutamine or pyruvate (ThermoFisher, 11960044) for 45 min at 37°C and 5% CO_2 to allow the eye tissue to soften. Afterward, the cornea, iris, and lens capsule were removed, and the remaining eye tissue was incubated in RPE culture media (10% Charcoal-Stripped FBS; R&D systems, S11650, 1% Penstrep, 2.5mM L-Glutamine (Gibco, 25030-81), 1X MEM nonessential amino acids (ThermoFisher, 11140050)) for 20 min at 37°C and 5% CO_2 to allow the neural retina to detach from the RPE. The RPE sheets were then manually dissected out and placed in an Eppendorf tube where the cells were dissociated from each other by pipetting up and down for ~40 times. The single cell suspension was plated on laminin (Gibco, 23017-015) coated 6.5 mm, 0.4 um pore Polyester Transwell membranes (Costar, 3470) in RPE culture media and incubated at 37°C and 5% CO_2 for 24 hours before being used for electrophysiology measurements.

Cloning of K$_{ir}$7.1 and expression in HEK293 cells.

The complete open reading frame of *Kcnj13* (the gene encoding K$_{ir}$7.1) was amplified from a cDNA library, generated by standard procedures from a C57Bl/6N male murine small intestine, an organ known to express high levels of *Kcnj13*. Primers used for the amplification bound to the untranslated region of the gene (in capital letters) with added restriction sites for SacI and SalI (K$_{ir}$7.1 Fw SacI: ataagagctcCACAAAGGAACCGAGAAACAC, K$_{ir}$7.1 Rev SalI: ataagtcgacGGACGGTGTAGATGAGTCTTA). After restriction digest of the sequence-confirmed full-length *Kcnj13* and the mammalian expression vector pIRES2-EGFP (Clonetech, 6029-1) by standard procedures, *Kcnj13* was inserted into the vector using the Quick Ligation Kit (New England BioLabs, M2200) according to the manufacturer's instructions. For recombinant expression, cells of the human embryonic kidney cell line (HEK293, ATCC, CRL-1573) were plated on collagen (Roche, 11179179001) coated coverslips and transfected using Lipofectamine 2000 reagent (Life Technologies, 11668027) according to the manufacturer's recommendation. Overexpression was verified by the presence of K$_{ir}$7.1 in immunocytochemical staining and Western blot analysis as mentioned below. The enhanced green fluorescent protein of the pIRES2-EGFP vector was used to visualize the transfected cells for whole-cell patch clamp experiments.

Immunohistochemistry and immunocytochemistry

For staining of mouse brain sections, C57Bl/6N, *Abhd2$^{+/+}$*, and *Abhd2$^{-/-}$* adult male mice were euthanized by perfusion with 4% paraformaldehyde (PFA, Electron Microscopy Sciences, 15714S) after which the brains were dissected out, placed in a sucrose gradient and frozen in Tissue-Tek O.C.T. compound (Sakura, 4583). The brains were sectioned using a cryotome into 8 μm thick coronal sections. For K$_{ir}$7.1 staining, the sections were permeated by incubation with 0.5% Triton X-100 (Fisher BioReagents, BP151-100) for 15 min. For the detection of ABHD2, antigen retrieval was performed by incubation with 1% sodium dodecyl sulfate (SDS, Sigma, L4509-100G) for 5 min. Thereafter, the sections were washed three times in PBS, blocked with 5% bovine serum albumin (BSA, Sigma, A9647) for one hour at room temperature, and incubated with primary antibody in PBS supplemented with 1% BSA overnight at 4°C. After washing three times in PBS, the sections were incubated with secondary antibody for 1 hour, washed three times in PBS, and mounted.

For the detection of both ABHD2 and K$_{ir}$7.1 in CPECs isolated from *Abhd2$^{+/+}$* and *Abhd2$^{-/-}$* mice, the cells were fixed with 2% PFA in PBS for 15 min and washed three times with PBS followed by antigen retrieval for 5 min using 0.75% SDS. For blocking, the cells were incubated overnight in 3% BSA and 0.1% Saponin (Sigma, 47036-50G-F) in PBS at +4°C, followed by overnight incubation with the primary antibody in blocking solution at +4°C. After washing three times in 0.1% saponin/PBS solution, the cells were incubated with secondary antibody in PBS supplemented with 1% BSA and 0.1% saponin for 1 hour, washed three times in 0.1% saponin/PBS solution, and mounted. For detection of K$_{ir}$7.1 in HEK293 cells (transfected as previously mentioned and cultured overnight on Poly-D-lysine (Millipore, P1024) coated

coverslips), the cells were fixed with 4% PFA in PBS for 10 min, permeated, stained, and mounted according to the protocol for Kir7.1 staining of brain sections.

For detection of $K_{ir}7.1$ in cultured RPE cells (isolated and cultured overnight on Poly-D-lysine and laminin coated coverslips), the cells were fixed with 2% PFA in PBS for 15 min and washed three times with PBS. Next, permeabilization and blocking of the cells were performed simultaneously by 1-hour incubation in blocking solution (1% BSA and 0.1% saponin in PBS). The cells were then incubated with the primary antibody in the blocking solution overnight at 4°C. After washing three times in 0.1% saponin/PBS, the cells were incubated with secondary antibody for 1 hour, washed three times in 0.1% saponin/PBS solution, and mounted.

The following primary antibodies were used: rabbit polyclonal anti-ABHD2 (1:300, Proteintech Group, 14039-1-AP) and mouse monoclonal anti-$K_{ir}7.1$ (1:300, Santa Cruz, sc-398810). The secondary antibodies conjugated with different fluorescent dyes were used: Dylight 488-conjugated goat anti-rabbit IgG (1:2000, Molecular Probes A11008/Jackson ImmunoResearch, 111-485-144) and Cy5-conjugated donkey anti-mouse (1:2000, Jackson ImmunoResearch, 715-175-150). For mounting, we used ProLong Gold antifade reagent with DAPI (Invitrogen, P36935). The cells were visualized with an inverse microscope (Olympus IX71) equipped with lumencor light engine (SPECTRAX 6-LCR-SA) while the brain sections were visualized using a confocal laser scanning microscopy (Olympus Fluoview FV1000).

In situ hybridization (ISH)

Lateral choroid plexus slices, isolated as described above, were used for ISH. CP total RNA was extracted from the murine ovary using a Qiagen RNAeasy mini kit followed by cDNA synthesis with a Phusion RT-PCR kit (Finnzymes, MA). The specific translated region of *Abhd2* was amplified using the following primers: forward 5' GTCGGATGGTGCCACTTC 3' and reverse 5' CCTCCATCTGCTCCGTGT 3', and subcloned into a vector containing Sp6/T7 promoters (Promega). Single strand digoxigenin-labeled RNA probes were synthesised (Roche) and colour ISH was performed as in (Ishii et al., 2004). A sense probe was used as a negative control.

Western blotting

To detect $K_{ir}7.1$ in HEK293 cells transfected with the pIRES2-EGFP/$K_{ir}7.1$ construct, the cells were cultured for 24 hours after transfection and harvested by standard procedures. The samples were analyzed by Western blotting, using the mouse monoclonal antibody against $K_{ir}7.1$ (1:10,000 dilution) and a peroxidase-conjugated goat anti-mouse secondary antibody (1:15,000 dilution, EMD-Millipore, AP181P). To ensure equal sample loading, the membrane was stripped by incubation with OneMinute Plus Strip (GM Biosciences, GM6011) according to the manufacturer's instructions. Thereafter, the membrane was re-hybridized with a mouse monoclonal anti-actin antibody (1:5,000 dilution, Abcam, ab3280-500) and the peroxidase-conjugated goat anti-mouse secondary antibody (1:15,000 dilution).

Reagents for electrophysiology

KMeSO$_3$ was purchased from Alfa Aesar (39505), progesterone from Millipore (5341), VU590 (7,13-bis[(4-nitrophenyl)methyl]-1,4,10- trioxa-7,13-diazacyclopentadecane) dihydrochloride from Fisher (389110), and Ursolic Acid from Cayman Chemical (10072). All other compounds were from Sigma Aldrich. Testosterone (Sigma, T1500) was purchased in accordance with the controlled substance protocol approved by UC Berkeley EH&S. For patch clamp measurements all bath solutions contained a concentration of 1:1000 of EtOH and DMSO, the solvents used to dissolve the steroid hormones and the antagonist VU590, respectively. Ursolic Acid was dissolved in DMSO as well.

Electrophysiology

CPECs and HEK293 cells, plated on 5mm glass coverslips, were placed in a perfusion chamber (Warner Instruments, RC-24E) and RPE cells plated on Transwell membranes were placed in an open bath recording chamber (Warner Instruments, RC22) and secured by a slice anchor (Warner Instruments, SHD-22L/15) for electrophysiological measurements at ambient temperatures. Data were acquired using the Clampex 10.5 software (Molecular Devices), which controlled an AXOPATCH 200B amplifier and an AxonTM Digidata 1550A digitizer (both Molecular Devices) with integrated Humbug noise eliminator. Data were not corrected for liquid junction potential changes. Gigaohm seals were established in dissection media (in mM: 140 NaCl, 15 HEPES, 15 d-glucose, 5 KCl, 1 CaCl$_2$, 1 MgCl$_2$ (pH 7.3 adjusted with NaOH, 310 mOsm/l)). The patch pipette was filled with either a Cs$^-$- or a K$^+$-based solution (in mM: 130 CsMeSO$_3$ or KMeSO$_3$, 20 HEPES, 5 BAPTA, and 1 MgCl$_2$ (pH 7.3 adjusted with CsOH or KOH, 295 mOsm/l)) and had a resistance of 3-6 MΩ. For measurements of the difference in monovalent currents, the bath solutions contained, in mM: 43 HEPES, 1 MgCl$_2$, and one of the following: 130 CsMeSO$_3$, 130 KMeSO$_3$, 130 RbCl, or 130 NaMeSO$_3$, (pH 7.3, 310 mOsm/l). All buffers, including those containing steroid hormones, were applied under constant perfusion. The K$_{ir}$7.1 antagonist VU590 (100 μM), in combination with P4, was applied directly to the bath solution. To block G-protein signaling 1 mM of guanosine 5'-O-(2-thiodiphosphate) (GDPβS) was applied to the K$^+$-based pipette solution. Measurements were performed at 10 kHz and filtered at 1 kHz. Cells were stimulated every 5 s by voltage ramps from –80 mV to +80 mV with a holding potential of 0 mV, or by 500 ms voltage steps from -120 mV to +40 mV in 20 mV increments with a holding potential of -40 mV. Access resistance and membrane capacitance were between 4-10 MΩ and 33 ± 1.09 pF for CPECs, 7-13 MΩ and 19.3 ± 1.08 pF for HEK293 cells and 10.5-14 MΩ and 12.7 ± 2.17 pF for RPE cells. Membrane capacitance served as a proxy for the cell surface area and used for normalization of current amplitudes (i.e. current density). Capacitance artifacts were graphically removed in OriginPro 8.6 (OriginLab Corp.). For current clamp measurements, the pipette solution contained, in mM: 40 NaCl, 100 KMeSO$_3$, 20 HEPES, 1 BAPTA, 5 Mg-ATP, and 0.5 Na-GTP, pH 7.2 was adjusted with KOH prior to adding the ATP and GTP stocks, 295 mOsm/l. The bath solution for current clamp contained, in mM: 140 NaCl, 5 KMeSO$_3$, 1 MgCl$_2$, 20 HEPES, and 10 d-glucose, pH 7.3 adjusted with NaOH, 310 mOsm/l).

Measurements were performed at 10 kHz and filtered at 10 kHz under a gap-free protocol with a 0 pA input signal.

Statistical analysis

For statistical analyses of the activation and inhibition of $K_{ir}7.1$ by different steroid hormones and the antagonist VU590, in measurements from CPECs, HEK293, and RPE cells, the Clampfit 10.3 (Molecular Devices) and GraphPad Prism 5 (GraphPad Software) software were used. Unpaired and paired t-test were used to determine statistical significance, assigning $p \leq 0.05$ as the limit. All results are shown with standard error of mean.

Results

Progesterone potentiates the activity of the inwardly rectifying potassium channel $K_{ir}7.1$ in choroid plexus epithelial cells

To study the non-genomic, fast-acting effect of steroid hormones on CP ion conductance, whole-cell patch clamp experiments were performed on choroid plexus epithelial cells (CPEC) isolated from the murine lateral ventricle. To avoid possible changes in gene expression during prolonged cell culture, all analyses were performed on the same day of tissue collection. When the cells were placed in a bath solution containing Cs^+ and Mg^{2+}, a strong inwardly rectifying current was observed in response to the voltage ramp from -80 mV to +80 mV applied from a holding potential of 0 mV (Fig. 1A). This current was further potentiated by exposure to 10 µM of P4 with a 1.69 ± 0.08 and 1.78 ± 0.11-fold change in cells isolated from female and male CP, respectively (Fig. 1B-C). The cell response to P4 was rapid with the current reaching its maximum potentiation within 50-60 seconds after the steroid was applied. Repetitive exposure to P4 only resulted in a slight desensitization of the current (Fig. 1C-E). To determine the ion channel responsible for the observed current, we analyzed mRNA expression data from adult murine CPs. Interestingly, one of the most abundantly expressed ion channels in CPEC is the inwardly rectifying potassium channel $K_{ir}7.1$ (encoded by *Kcnj13*; Fig. 2; Table 1), which is also the only potassium channel that can conduct Cs^+ ions[76]. To test the hypothesis that P4 activates $K_{ir}7.1$, the $K_{ir}7.1/K_{ir}1.1$ specific antagonist VU590 was used. When applying 20 µM of the inhibitor a significant reduction of the inward current was observed (Fig. 3A and Fig. 4A), and P4 failed to potentiate the current in the presence of VU590 (Fig. 3A and Fig. 4A). Since the expression of *Kcnj1* (encoding $K_{ir}1.1$) is not detected in CPEC (Table 1), it is highly likely that the observed reduction in current is caused by blocking the activity of $K_{ir}7.1$. Furthermore, $K_{ir}7.1$ was detected via immunohistochemical staining in the apical membrane of the murine CP, and was also present after lateral CP cell isolation and culturing (Fig. 3B-D). $K_{ir}7.1$ has a signature ion selectivity with the following order of preference: $Rb^+>>Cs^+>K^+>>Na^{+}$[84], which was indeed observed in CPEC recordings (Fig. 3E-F). Since $K_{ir}7.1$ mainly conducts potassium ions in its native state, all further experiments were performed using bath and pipette solutions where Cs^+ was replaced with K^+. In addition, 100 µM of VU590 was applied at the end of each recording to confirm that the measured potentiated current was not a byproduct of leak current.

Progesterone specific regulation of $K_{ir}7.1$ activity

By measuring $K_{ir}7.1$ potentiation with different concentrations of P4 the EC_{50} for P4 was determined to be 5.65 ± 0.50 µM with the maximal effective concentration reached around 50 µM (Fig. 5A-B). To test whether other steroid hormones are able to increase the activity of $K_{ir}7.1$, CPECs were stimulated with 10 µM of testosterone (T), estradiol (E2), pregnenolone sulfate (PS) and the synthetic progestin levonorgestrel (LNG) (Fig. 5C). Surprisingly, none of these steroids were able to significantly change the activity of $K_{ir}7.1$ (Fig. 5C-D), although the

addition of 10 µM of P4 at the end of each experiment still caused a 3.08 ± 0.20-fold increase in current at -80 mV (Fig. 5D). The results indicate that P4 activation of $K_{ir}7.1$ is specific for this steroid. The significance of P4 activation was also analyzed by current-clamp method, where the solutions used had an ion concentration and osmolarity comparable to that of CSF and the intracellular environment of CPECs. To measure the native membrane potential of CPECs, no current was applied to the cells and the average initial V_m measured was -57.2 ± 4.6 mV (n= 3; Fig. 5E). Under such conditions, the application of 10 µM of P4 caused hyperpolarization of the cells with an average decrease in membrane potential of 9.13 ± 3.56 mV (Fig. 5E-F). Similar to the whole-cell patch clamp recordings, applying 100 µM of the antagonist VU590 caused a significant inhibition of $K_{ir}7.1$ conductance which led to depolarization of the cell with a significant increase in membrane potential of 29.95 ± 6.51 mV, even in the presence of P4 (Fig. 5E).

Secondary messengers are not required for the potentiation of $K_{ir}7.1$ activity by progesterone

The CP epithelium contains many membrane-bound progesterone receptors that could potentially mediate the cell response to P4. Interestingly, we found that the recently characterized progesterone receptor α/β hydrolase domain–containing protein 2 (ABHD2)[138] is also highly expressed in the CP (Fig. 7A, Fig. 8A; Table 1) and therefore is found in cultured CPECs (Fig. 6B-C). ABHD2 has been shown to regulate ion channel activation in human sperm cells by breaking down the endocannabinoid 2-arachidonoylglycerol in the cell membrane[138] However, CPECs isolated from *Abhd2* knockout mice that were generated in our lab[142] showed similar activation of $K_{ir}7.1$ as cells from wild type animals (Fig. 8D-F), thus negating any effect of the receptor in $K_{ir}7.1$ activation. To further validate a direct interaction between P4 and $K_{ir}7.1$, the full-length mRNA sequence of murine *Kcnj13* was cloned into an expression vector and subsequently expressed in HEK293 cells. The cells do not display any endogenous expression of the channel but, as determined in previous studies[145], products of the transfected construct were able to be glycosylated and transported to the cell membrane as shown by Western blot and immunocytochemistry (Fig. 6B-C). Whole-cell patch clamp recordings of the transfected HEK293 cells show a similar potentiation of $I_{Kir7.1}$ after applying 10 µM P4 to the bath solution (Fig. 6A, G and Fig. 4B). The fast activation of $K_{ir}7.1$ by P4 in CPECs and the results from HEK293 cells make a compelling argument for the activation of $K_{ir}7.1$ to be caused by a direct interaction of P4 with the channel complex. Our mRNA seq data also provide evidence of G-protein coupled progesterone receptors in the CP (Table 1), a signaling pathway previously shown to be involved in $K_{ir}7.1$ regulation[145]. To test whether or not these signaling pathways would lead to the observed potentiation of $K_{ir}7.1$ activation, 1 mM Guanosine-5'-(β-thio)-diphosphate, Sodium salt (GDPβS), a competitive inhibitor of GTP activation of G-protein signaling, was applied to the pipette solution while recording $K_{ir}7.1$ from either CPECs (Fig 6F-G) or HEK293 cells (Fig. 6F and Fig. 4B). In both cases, the presence of the inhibitor had no effect on P4- mediated $K_{ir}7.1$ potentiation (Fig. 6), which further confirmed that G-protein signaling is not involved in P4-regulation of $K_{ir}7.1$.

Progesterone potentiates the retinal pigment epithelium $K_{ir}7.1$ activity

$K_{ir}7.1$ is also found in the RPE, where the channel works in concert with the Na^+-K^+-ATPase to regulate K^+ homeostasis and photoreceptor excitability[78]. To determine if $K_{ir}7.1$ in RPE cells shows similar activation by P4 as in CPECs, whole-cell patch clamp recordings were performed. RPE cells that had been isolated and cultured overnight were used for the experiments (Fig. 6E). The currents measured from these cells were considerably smaller than the currents of LCP cells (Fig. 6D, 9C and Fig. 4B). However, a statistically significant potentiation of inward $I_{Kir7.1}$ was observed after stimulation with 10 µM of P4 (Fig. 4B). We can thus, conclude that the effect of P4 on $K_{ir}7.1$ activity is not limited to the CP but could, in addition, have important physiological implications in other tissues.

Ursolic Acid inhibits progesterone potentiation of $K_{ir}7.1$

In the presence of the natural triterpenoid, ursolic acid (UA), progesterone-induced potentiation of $K_{ir}7.1$ was inhibited. In the presence of UA, initial activation of $K_{ir}7.1$ by P4 was still able to occur within the first 50 seconds of application, as seen previously (Fig. 9A-C). However, within 10 seconds of full potentiation by P4, UA began inhibiting the channel (Fig. 9B). Inhibition by UA was almost as profound as that of $K_{ir}7.1$ antagonist, VU590 (Fig. 9A).

Figure 1
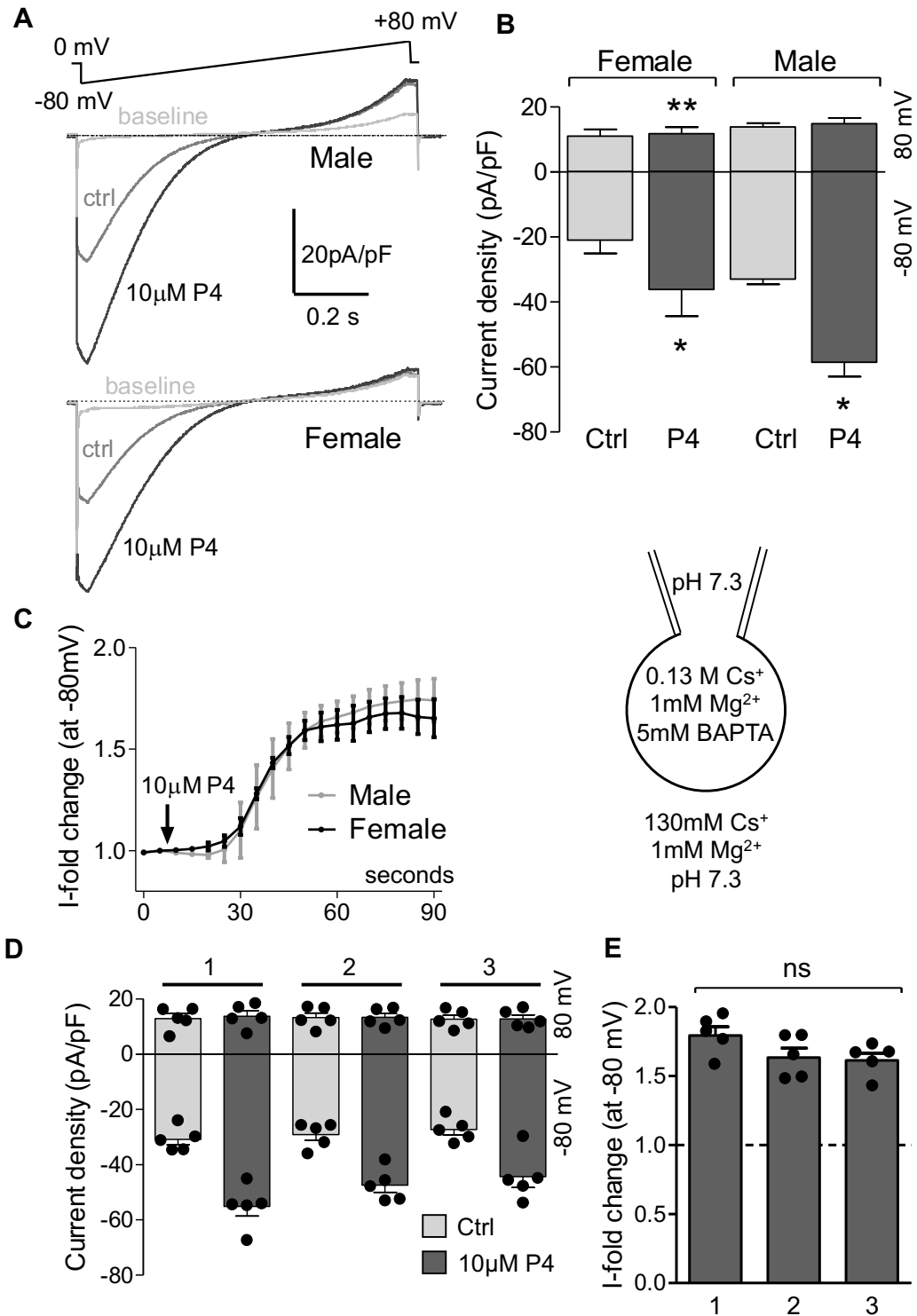
Figure 1. Potentiation of an inwardly rectifying ion conductance by progesterone in murine choroid plexus epithelial cells (CPEC).

Whole-cell recordings from both male and female CPEC show a significant potentiation of an inwardly rectifying ion current upon exposure to 10 µM progesterone (P4) in the bath solution.

A) Representative traces from isolated lateral CPEC elicited in response to a voltage ramp, as indicated. B) Average current densities at -80 mV and 80 mV from 4 female and 3 male CPEC in the absence or presence of 10 µM P4, recorded from ramps shown in (A). Statistical significance was calculated using the paired t-test and the significance of changes is indicated as follows: *, $p \leq 0.05$, **, $p \leq 0.01$.

C) Current fold increase obtained at -80 mV in (B) and plotted against time, show a fast response to P4. The time of application of 10 µM P4 to the bath solution is indicated by an arrow.

D) Application of 10 µM progesterone (P4) to lateral CPEC (n = 5) for three consecutive times did not lead to a significant desensitization of the current.

E) Current fold change at -80 mV after application of 10 µM P4. Data are means ± SEM.

Figure 2
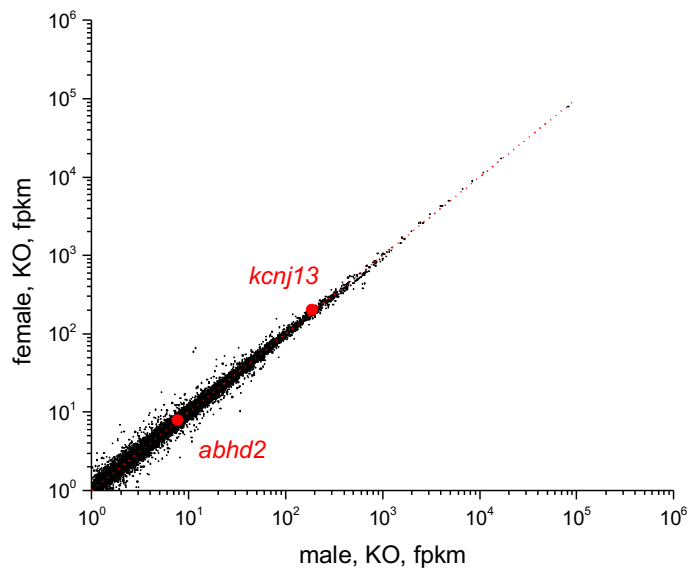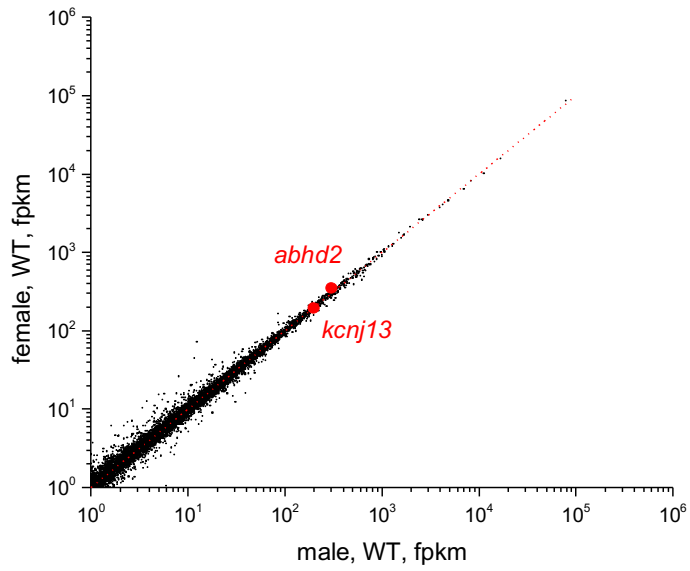
Figure 2. The relative gene expression of the lateral choroid plexuses isolated from Abhd2$^{+/+}$ and Abhd2$^{-/-}$ male and female mice.

Number of mRNA-Seq reads from corresponding choroid plexuses mapped to the mouse genome. *Abhd2* and *Kcnj13* expression levels are shown. Red dotted lines represent an expected number of sequencing reads for genes with similar expression levels between two samples. Signals < 10 reads are within statistical noise and therefore scored as non-expressed sequences. FPKM, fragments per kilobase of transcript per million mapped reads.

Figure 3

A

10µM P4   +   −   +
20µM VU590   −   +   +

B   Lateral ventricle

C $K_{ir}7.1$ DAPI   100µm   1   25µm

D   Cultured CPEC $K_{ir}7.1$ DAPI $K_{ir}7.1$ 10µm

E   +40 mV   −40 mV   −120 mV

Na^+ 0.6nA

K^+

Cs^+ 0.6nA   50ms

Rb^+ 2nA

F Rb^+ K^+ Cs^+ Na^+ pH 7.3

0.13 K^+
1mM Mg^{2+}
5mM BAPTA

130mM X^+
1mM Mg^{2+}
pH 7.3
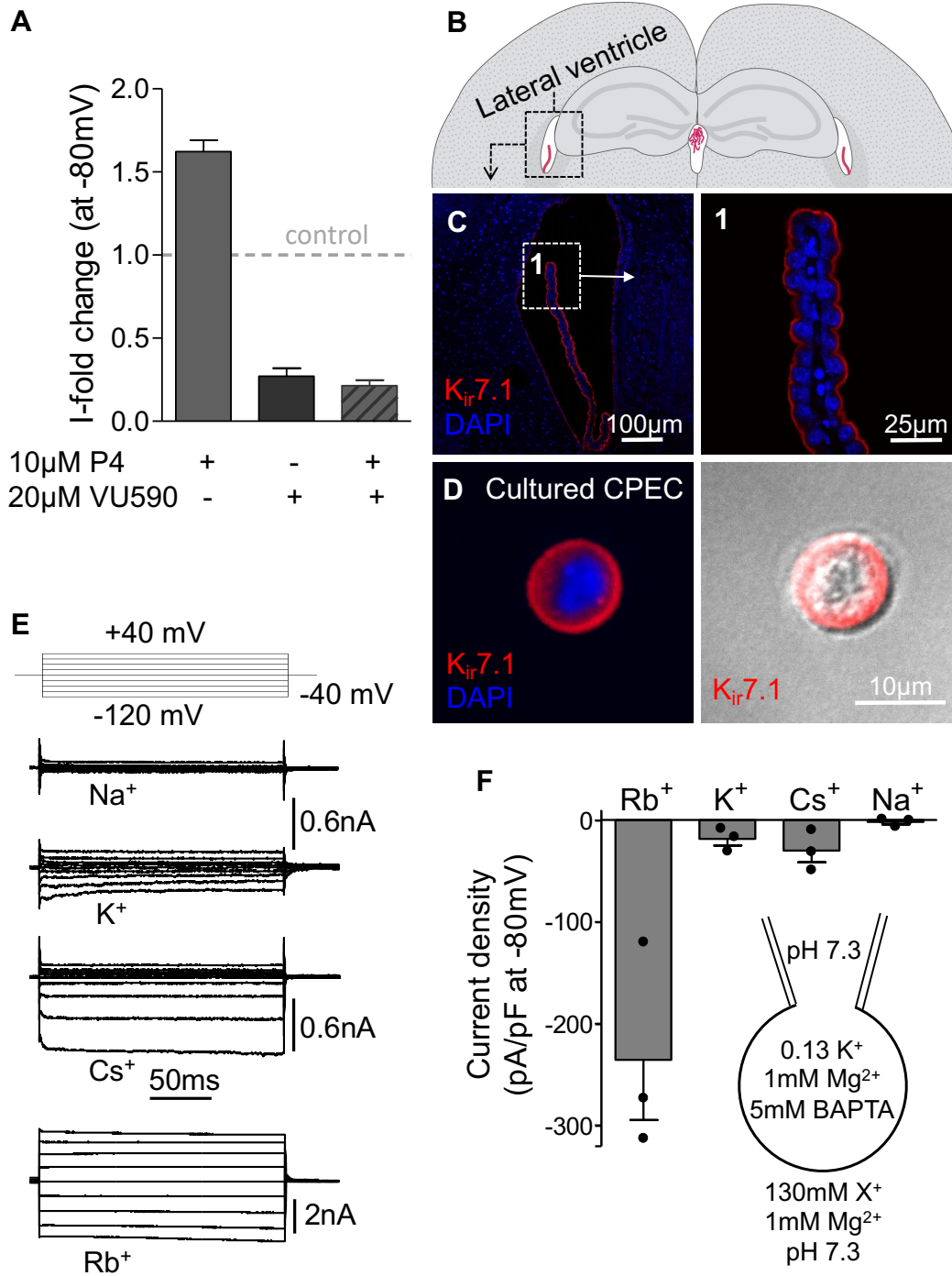
Figure 3. Expression and permeability of $K_{ir}7.1$ from murine choroid plexus.

A) The inwardly rectifying current, detected in whole cell recordings from choroid plexus epithelial cells (CPEC), was inhibited by 20 µM of the $K_{ir}7.1$ and $K_{ir}1.1$ specific antagonist VU590 added in the bath solution. In the presence of VU590, further potentiation of the current by 10 µM progesterone (P4) was prevented. The $K_{ir}7.1$ current fold change at -80 mV is shown upon stimulation with either 10 µM P4, 20 µM VU590, or 20 µM VU590 + 10 µM P4 to three individual CPEC.

B) Schematic image showing localization of the lateral ventricle in the mouse brain.

C) Immunohistochemical image from a C57Bl/6N adult male, shows $K_{ir}7.1$ expression on the (1) apical side of the lateral ventricle choroid plexus.

D) $K_{ir}7.1$ is also detected in the plasma membrane of CPEC that have been isolated from an adult female mouse and cultured for 3 hours.

E) Representative traces of $K_{ir}7.1$ currents recorded in whole-cell mode from lateral CPEC in response to a voltage step protocol (from -120 mV to +40 mV, in 20 mV increments, starting from a holding potential of -40mV) as shown. Exposing CPEC to different bath solutions shows large conductance when the cells are in a Rb^+-based buffer, while Cs^+ and K^+ -based buffers showed smaller, but similar conductances. Na^+ -based bath solution did not elicit any current.

F) Current densities from three CPEC exposed to the different bath solutions at -80 mV, as recorded in (E). Data are means ± SEM.

Figure 4
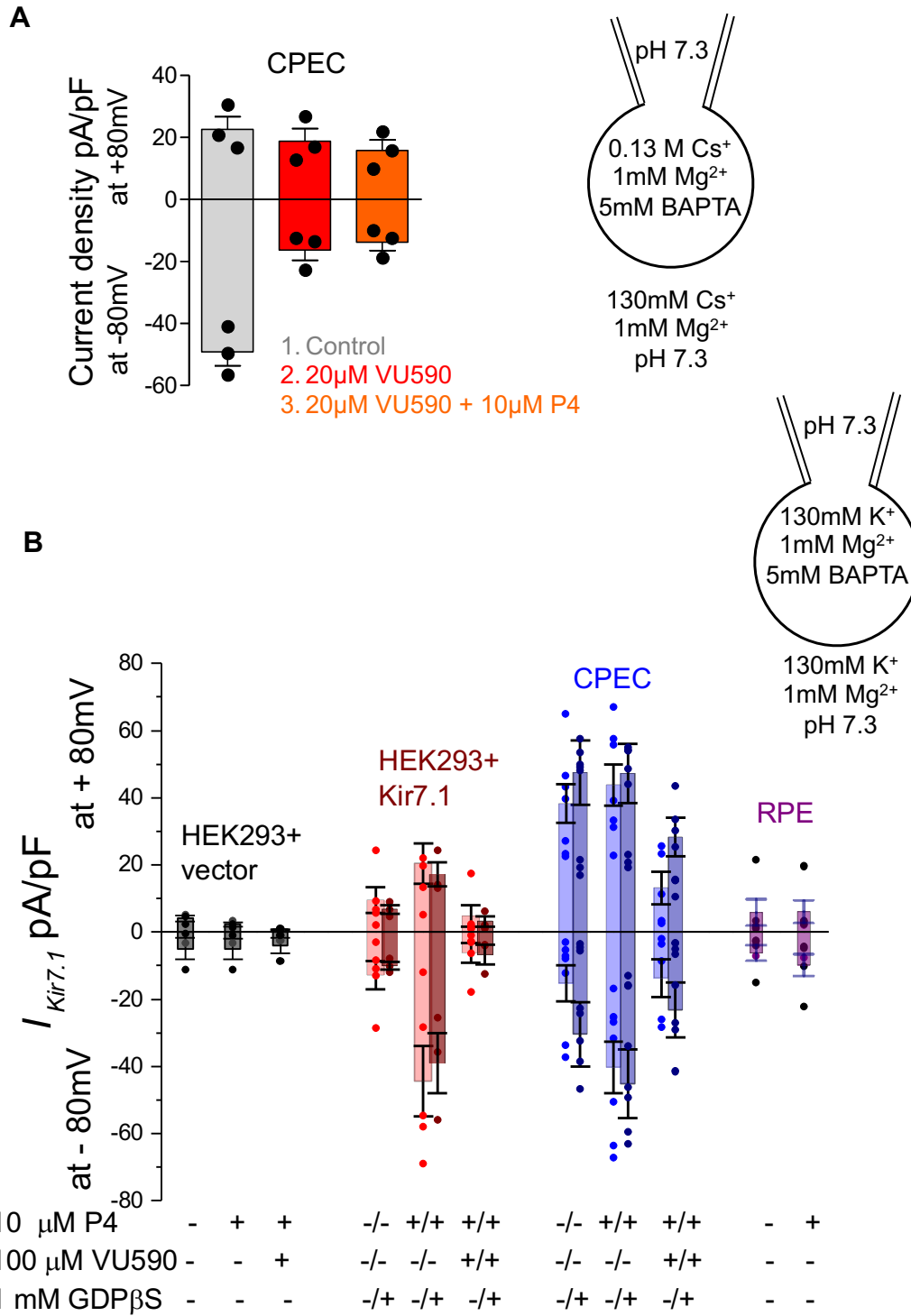
Figure 4. Kir7.1 current density in different cell types in the presence of progesterone and inhibitors.

A) A reduction in current density was observed at -80 mV after applying 20 µM of the $K_{ir}7.1$ and $K_{ir}1.1$ inhibitor VU590 to choroid plexus epithelial cells (CPEC). VU590 prevented any potentiation of the current by progesterone (P4).

B) Current densities recorded from HEK293 cells transfected with a recombinant $K_{ir}7.1$ or with the empty vector, as well as from CPEC and retinal epithelial cells (RPE). Currents were recorded as shown in 4A in the presence or absence of P4, Guanosine-5'-(β-thio)-diphosphate, Sodium salt (GDPβS) or VU590 as indicated. HEK293 cells transfected with the empty vector were used as a control.

Figure 5
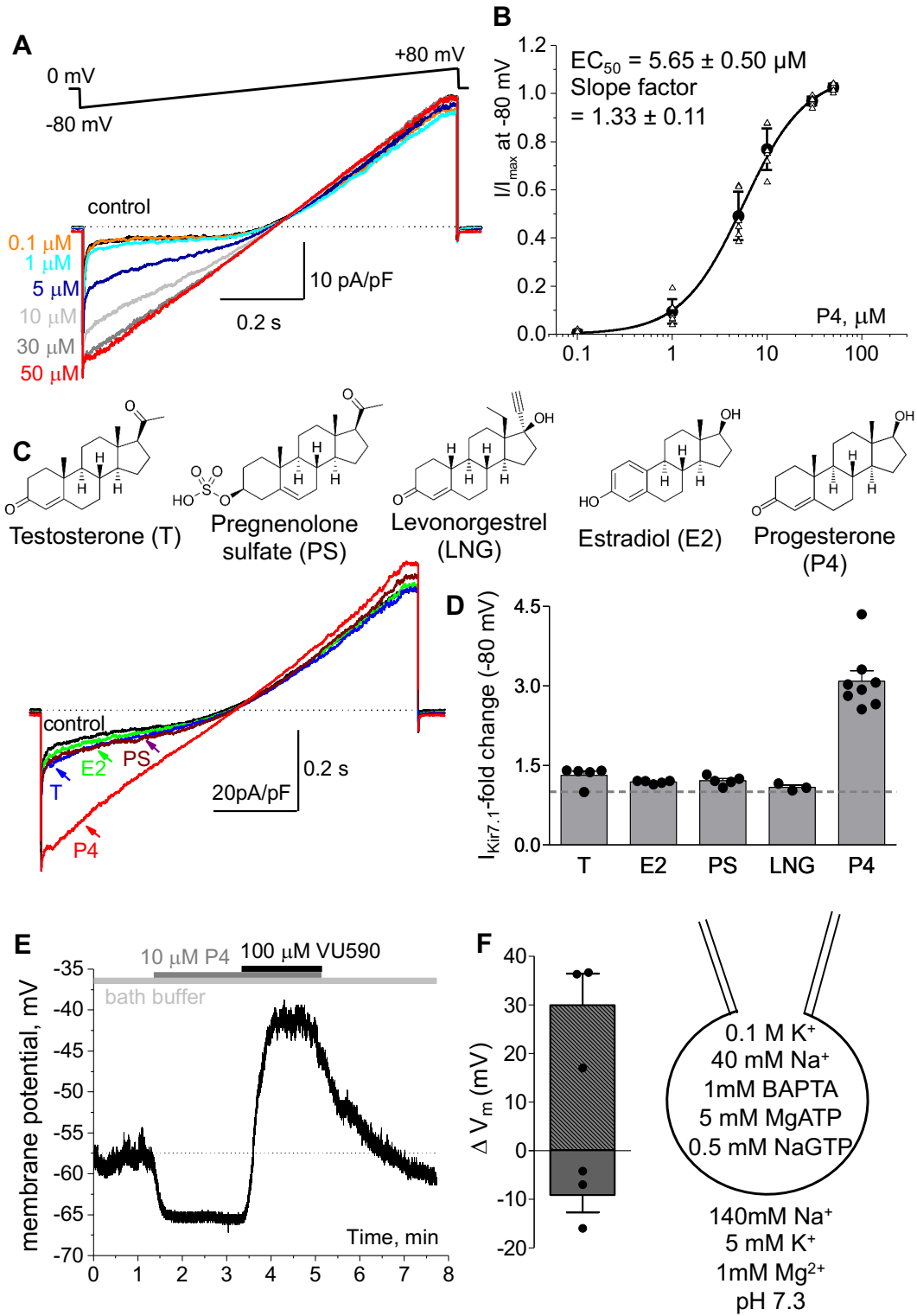
Figure 5. Potentiation of $K_{ir}7.1$ by steroid hormones.

A) Representative traces recorded from female murine choroid plexus epithelial cells (CPEC) isolated from a lateral ventricle. A gradual increase in current was observed after applying increasing concentrations of P4 to the bath solution.

B) EC_{50} for P4 was calculated using the average current density at -80 mV for 7 cells isolated from CPEC, as mentioned in (A).

C) Representative traces and D) the average current fold increase of $K_{ir}7.1$ at -80 mV recorded from 5 CPECs that were exposed to 10 µM of T, E2, PS and P4. Three CPEC were assessed on their modulation by 10 µM LGN. The chemical structure of the different steroids used for patch clamp recordings is shown. The steroids were applied in different orders for each cell, with P4 always added in the last order.

E) A representative current clamp measurement, which shows hyperpolarization of a CPEC after applying 10 µM P4 to the bath buffer. When blocking $K_{ir}7.1$ activity with 100 µM VU590 a significant cellular depolarization was detected.

F) Average changes in membrane potential (mV) as measured by current clamp recordings of 3 cells when applying 10 µM P4 (grey bar) or 100 µM VU590 + 10 µM P4 (patterned bar). Data are means ± SEM.

Figure 6
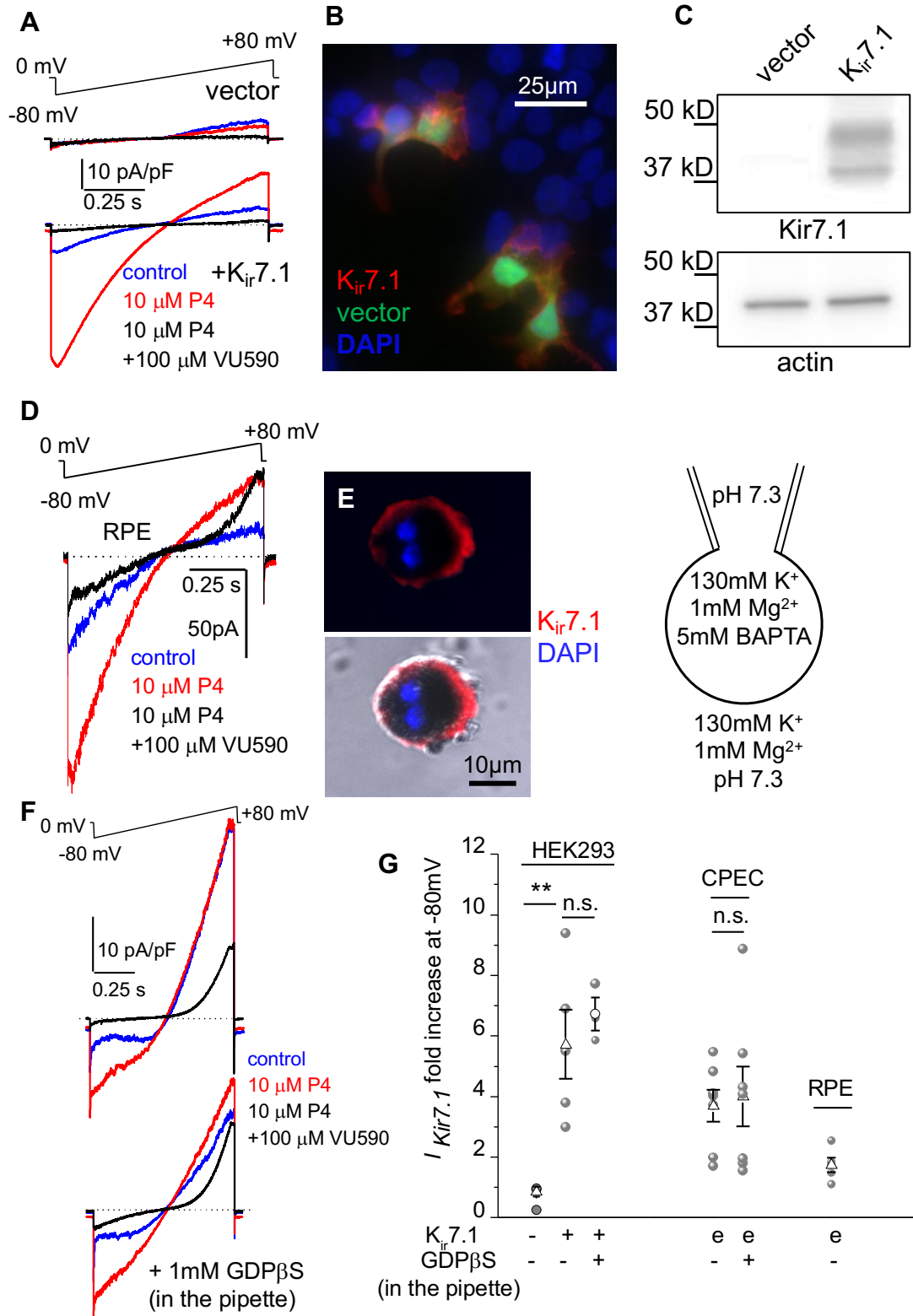
Figure 6. Potentiation of Kir7.1 by progesterone in different cell types is independent of G-protein coupled receptor signaling.

A) Representative traces recorded from HEK293 cells transfected with a pIRES2-EGFP/K$_{ir}$7.1 construct show a five-fold potentiation of the current after addition of 10 µM progesterone (P4) to the bath. The cells transfected with the empty vector do not respond to P4 or display $I_{Kir7.1}$.

B) Immunohistochemical staining of recombinant K$_{ir}$7.1 in HEK293 cells transfected with the pIRES2-EGFP/K$_{ir}$7.1 construct.

C) Western blotting detects both the mature glycosylated and the shorter immature product of K$_{ir}$7.1 seen in HEK293 cells transfected with the pIRES2-EGFP/K$_{ir}$7.1 construct. The cells transfected with the empty vector do not express K$_{ir}$7.1. Actin was used as a loading control.

D) Representative whole-cell recordings from retinal pigment epithelial (RPE) cells in response to 10 µM P4. RPE was isolated from a 1-month-old female mouse. A significant increase in the inward current density occurred at -80 mV, while the outward current recorded at +80mV did not change.

E) Immunocytochemical staining of mouse RPE cells detects K$_{ir}$7.1.

F) Representative $I_{Kir7.1}$ from an isolated adult female lateral choroid plexus epithelial cell (CPEC) is similarly activated by 10 µM P4 in the presence of 1 mM Guanosine-5'-(β-thio)-diphosphate, Sodium salt (GDPβS) in the pipette.

G) Graph depicting the fold change in $I_{Kir7.1}$ after exposure to 10 µM P4 recorded from transfected HEK293 cells, CPEC and RPE cells. Data are means ± SEM.

Figure 7
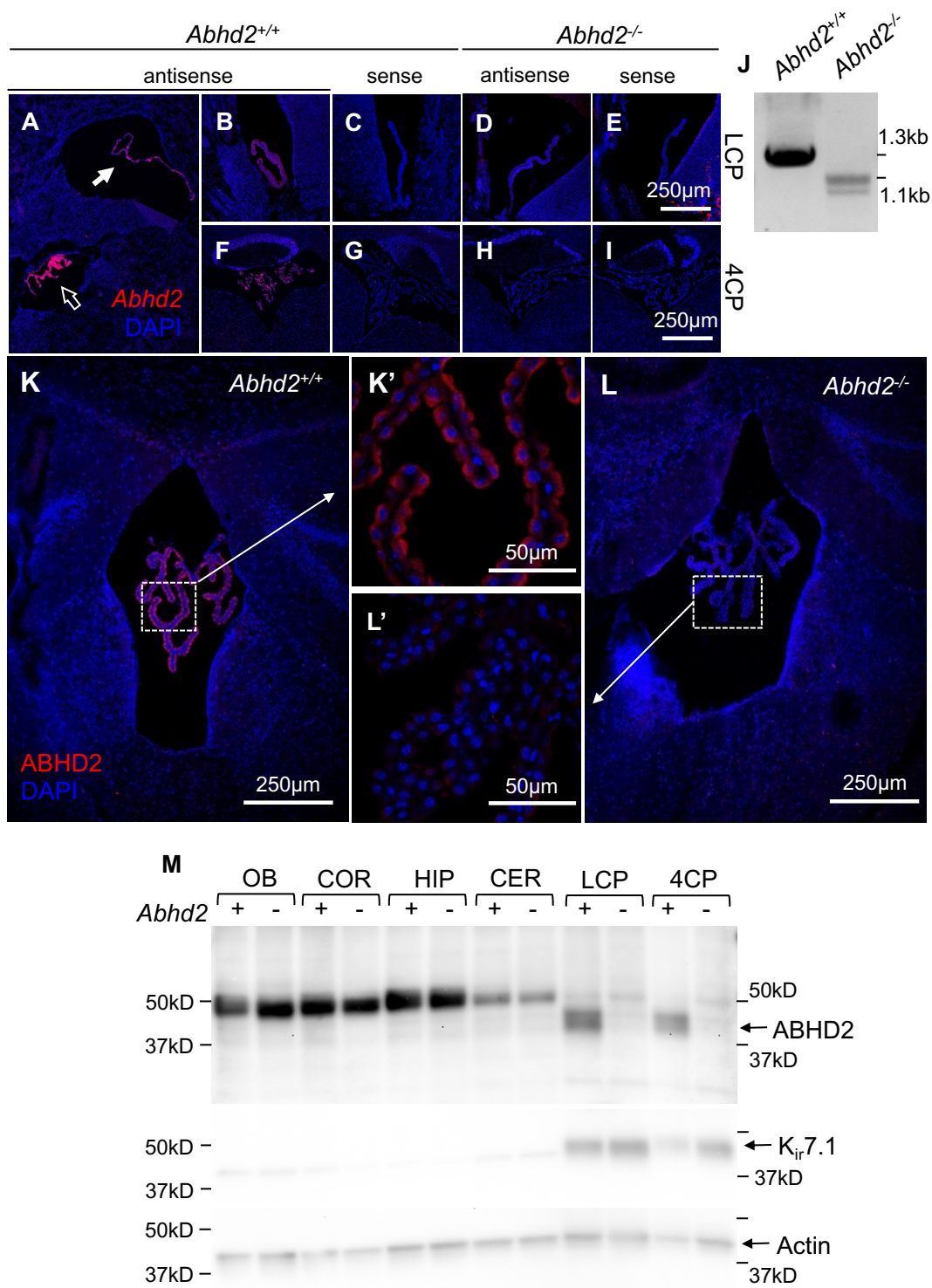
Figure 7. Expression of *Abhd2* in murine choroid plexuses.

In situ hybridization (ISH) show strong expression of α,β-hydrolase domain-containing protein 2 (*Abhd2*) in the lateral (A; solid arrow, and B), 3rd (A; open arrow) and 4th ventricle choroid plexus (F) of *Abhd2*$^{+/+}$ mice. The adult *Abhd2*$^{-/-}$ mice display similar background staining when using either the antisense (D and H) or the sense (E and I) probe against *Abhd2*. J) Although the antisense probe failed to bind to *Abhd2* mRNA in the *Abhd2*$^{-/-}$ animals in ISH experiments, a product lacking either *Abhd2* exon 6 or both exon 6 and exon 7 are detected in the kidney of *Abhd2*$^{-/-}$ mice. However, this mRNA product would lead to a frame shift and results in a truncated non-functional form of the protein. ABHD2 protein was detected by immunohistochemistry and western blot in the choroid plexus of *Abhd2*$^{+/+}$ mice (K and M), with a localization on the apical side of the epithelium (K'). L) ABHD2 was not detected in CP of *Abhd2*$^{-/-}$ mice (L'). M) ABHD2 was not detected in the other regions of the brain, such as the olfactory bulb (OB), the cortex (COR), the hippocampus (HIP), and the cerebellum (CER). However, it was exclusively found in both the lateral (LCP) and the 4th (4CP) ventricle choroid plexus of *Abhd2*$^{+/+}$ animals. *Abhd2*$^{-/-}$ animals do display a strong expression of Kir7.1 even in the absence of ABHD2. Actin was used as a loading control.

Figure 8
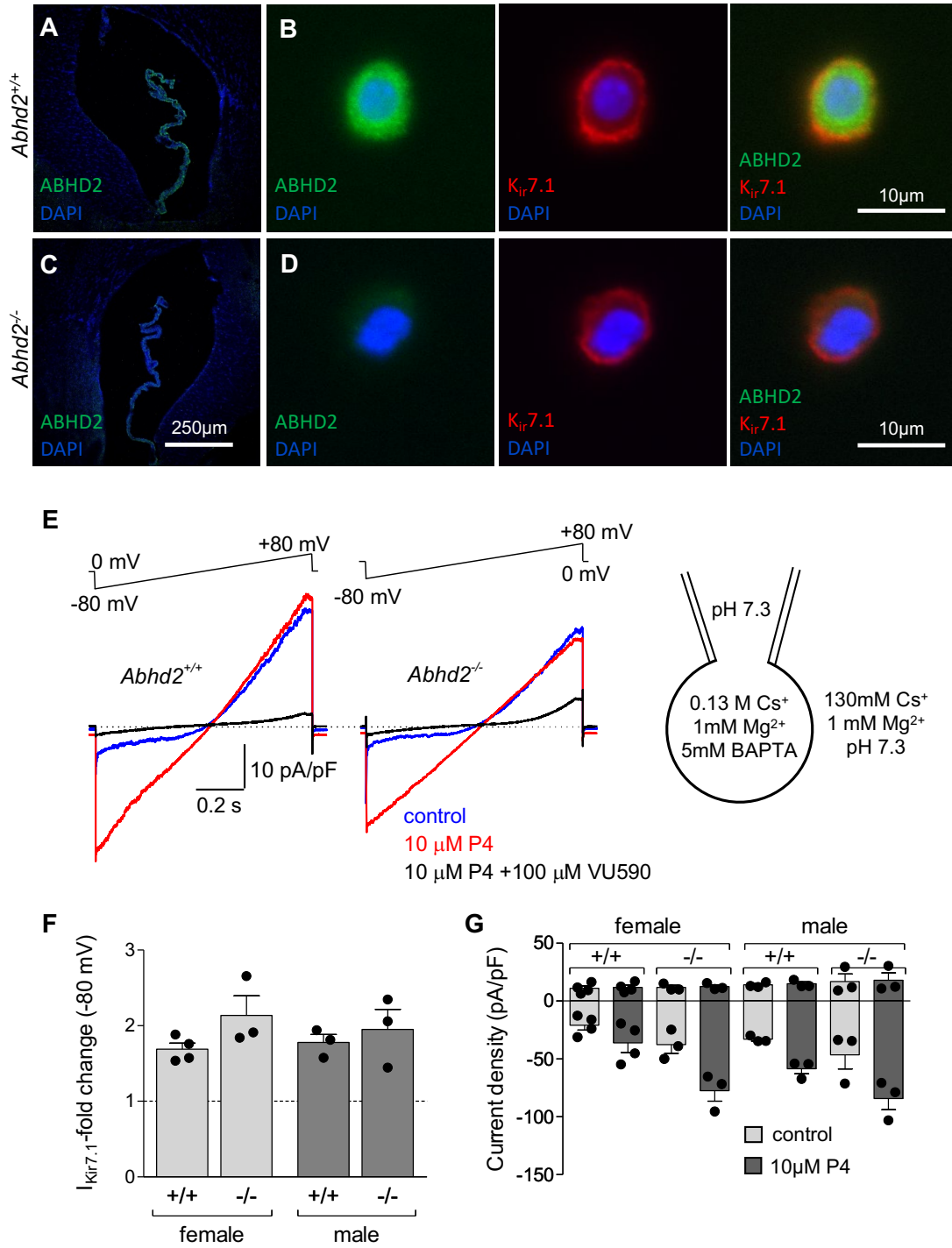
Figure 8. *Abhd2^{-/-}* murine choroid plexus epithelial cells (CPEC) show similar potentiation of K$_{ir}$7.1 by progesterone (P4) as wild type mice.

A) Immunohistochemical staining of the lateral ventricle choroid plexus of   hydrolase domain-containing protein 2 (ABHD2) in *Abhd2$^{+/+}$* and (B) *Abhd2$^{-/-}$* adult male mice.

C and D) Immunocytochemical staining of cultured CPEC show presence of K$_{ir}$7.1 in cells of both genotypes (*Abhd2$^{+/+}$* and *Abhd2$^{-/-}$*), although the latter lack ABHD2.

E) Representative recordings from adult male CPEC from *Abhd2$^{-/-}$* mice show similar potentiation of the K$_{ir}$7.1 current as cells from *Abhd2$^{+/+}$* animals when 10 µM P4 was added to the bath solution. Whole-cell recordings were performed using Cs^{+} bath and pipette solutions, as indicated.

F) The fold change of $I_{Kir7.1}$ at -80 mV was calculated from recordings of 4 wild type female cells and 3 cells of all other genotypes and genders shown in (G). Although the *Abhd2* knockout cells show a slightly higher current fold increase, the difference is not statistically significant when compared to that of wild type cells.

Figure 9

A

+UA 20 μM+ 10 μM P4 +VU590

50 pA

200 ms

control
+UA 20 μM
+UA 20 μM+ 10 μM P4 (initial)
+UA 20 μM+ 10 μM P4 (desensitization)

B

UA 20 μM   10 μM P4   VU590

current density at -80mV, pA/pF

Time, s

C

$I_{Kir7.1}$ fold increase at -80mV

**

n.s.

UA +P4

UA alone

HEK293
/vector

HEK293
/K$_{ir}$7.1

CP
+ 1mM
GDPβS

CP

RPE
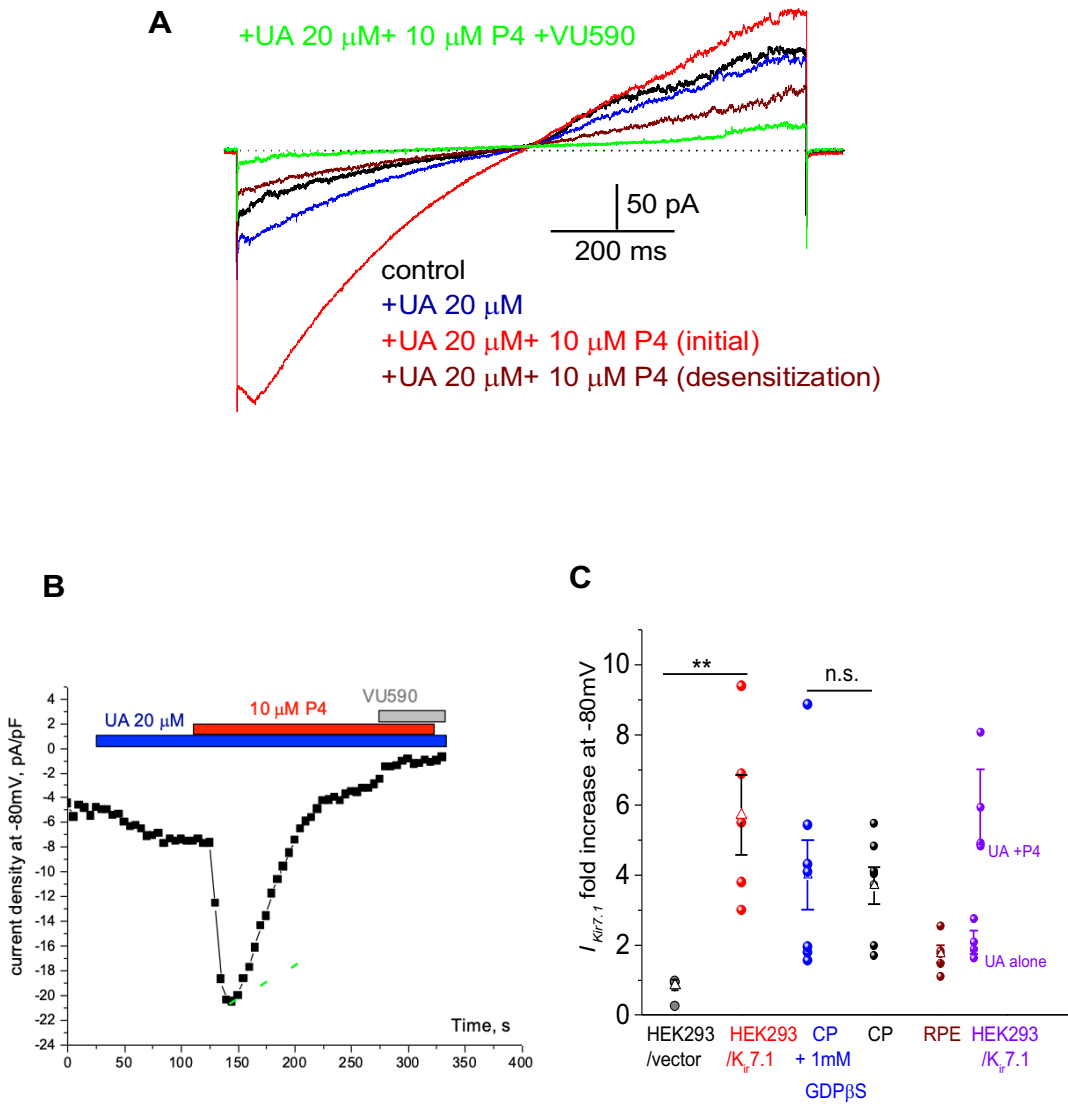
HEK293
/K$_{ir}$7.1

Figure 9: Inhibition of progesterone-induced potentiation of Kir7.1 by 10µM Ursolic Acid

A) Representative traces recorded from HEK293 cells transfected with a pIRES2-EGFP/K$_{ir}$7.1 construct show a five-fold potentiation of the current after addition of 10 µM progesterone (P4) to the bath. Show no potential with UA alone but saw large inhibition of current in the presence of P4

B) Current Density at -80mV shows the initial potential by P4 followed by immediate inhibition by UA. The antagonist VU590, added at the end, showed a slight further inhibition of K$_{ir}$7.1.

(C) Graph depicting the fold change in $I_{Kir7.1}$ after exposure to 10 µM P4 alone or 10µM P4 and 20µM UA, recorded from transfected HEK293 cells, CPEC and RPE cells. Data are means ± SEM.

Table 1: Expression of the Potassium voltage-gated channel subfamily J (KCNJ) in the mouse choroid plexus, determined by mRNA sequencing.

Gene	Protein	Female (fpkm)	Male (fpkm)	p-value (male vs. female)
Kcnj1	Kir1.1	0	0	*NA*
Kcnj2	Kir2.1	0.14	0.08	*0.255*
Kcnj3	Kir3.1	0.002	0.06	*0.070*
Kcnj4	Kir2.3	0.19	0.18	*0.920*
Kcnj5	Kir3.4	0.002	0	*0.701*
Kcnj6	Kir3.2	0	0.01	*0.570*
Kcnj8	Kir6.1	0.81	0.55	*0.279*
Kcnj9	Kir3.3	0.03	0.18	**0.039*
Kcnj10	Kir4.1	0.61	0.77	*0.726*
Kcnj11	Kir6.2	0.82	0.76	*0.967*
Kcnj12	Kir2.2	0.08	0.12	*0.686*
Kcnj13	**Kir7.1**	**195.13**	**198.09**	*0.724*
Kcnj14	Kir2.4	0.008	0	*0.701*
Kcnj15	Kir4.2	0.009	0.02	*0.732*
Kcnj16	Kir5.1	0.08	0.03	*0.271*

n = 3 for each gender, statistical significance is indicated as follows: *, $p \leq 0.05$.

Table 2: Expression of progesterone receptors in the choroid plexus of adult female and male mice, analyzed by mRNA sequencing.

Gene	Protein	Female (fpkm)	Male (fpkm)	p-value (male vs. female)
Pgr	Progesterone receptor	0.008	0.014	0.74
Paqr7	Membrane progesterone receptor alpha (mPRα)	5.09	4.96	0.84
Paqr8	Membrane progesterone receptor beta (mPRβ)	1.60	1.53	0.65
Paqr5	Membrane progesterone receptor gamma (mPRγ)	12.90	15.77	**0.0023
Paqr6	Membrane progesterone receptor delta (mPRδ)	1.85	1.18	*0.044
Paqr9	Membrane progesterone receptor epsilon (mPRε)	9.86	7.92	**0.0013
Pgrmc1	Progesterone receptor membrane component 1	301.29	310.57	0.43
Pgrmc2	Progesterone receptor membrane component 2	54.90	59.81	0.062
Abhd2	Abhydrolase domain-containing protein 2	351.53	300.73	**0.0070

n = 3 for each gender, statistical significance is indicated as follows: *, $p \leq 0.05$, **, $p \leq 0.01$.

Discussion

The adult murine choroid plexus represents a novel model to study nongenomic steroid signaling, because P4 is able to regulate this tissue[136,146] even under negligible expression levels of the nuclear progesterone receptor (Extended Data Tables 1-3). Since P4 is known to affect ion channels in neurons, either through a direct interaction between the steroid and the channel, or as an indirect response that occurs following steroid binding to its receptor[92,135,136,138,147], we aimed to determine whether P4 can influence ion conductance in CPEC via one of those mechanisms. By performing electrophysiological studies on CPECs, we showed a novel, P4- specific activation of an inwardly rectifying potassium channel $K_{ir}7.1$. This P4 activation was inhibited by the addition of VU590, a specific inhibitor of $K_{ir}1.1$ and $K_{ir}7.1$ channels. Since only $K_{ir}7.1$ is highly expressed in CPECs, these experiments further confirm the channel identity. Furthermore, the recorded conductance displayed $K_{ir}7.1$- specific hallmarks, such as the lack of an internal Mg^{2+} block, a high Rb^+ conductivity, and a low sensitivity to Cs^+ [76,84,148]. Interestingly, the rapid potentiation of $I_{Kir7.1}$ by P4 was independent of ABHD2- the known P4 membrane receptors. This was confirmed by recordings from *Abhd2*-deficient murine CPECs, which retained a similar activation of $K_{ir}7.1$ by P4. The involvement of G-protein coupled receptors in this process was ruled out, as addition of GDPβS, a competitive inhibitor of G-protein signaling, did not alter the potentiation of $I_{Kir7.1}$. Additionally, recordings of a recombinant $K_{ir}7.1$ expressed in HEK293 cells, as well as recordings in the absence of intracellular messengers, such as GTP, displayed similar potentiation of $K_{ir}7.1$ by P4. We, therefore, suggest that P4 activates $K_{ir}7.1$ directly. Previous studies on the effect of membrane fluidity on K_{ir} channels have shown cholesterol- driven regulation of these channels. Although the activity of most K_{ir} channels is suppressed with increased cholesterol levels in the membrane, $K_{ir}7.1$ is an exception to the rule and, instead, showed a slight activation of ion flux[77]. In silico analyses stated that this activation was caused by a weak interaction between $K_{ir}7.1$ and cholesterol rather than a change in membrane fluidity[149]. Similarly, steroids are known to change the cell membrane fluidity[150–152]. If $K_{ir}7.1$ activation by P4 is due to an altered membrane composition, then other lipophilic hormones would have had a similar effect on $K_{ir}7.1$. However, none of the tested steroids; testosterone, estradiol, levonorgestrel and pregnenolone sulfate, were able to influence $I_{Kir7.1}$. Thus, $K_{ir}7.1$ displays a specific affinity for P4, and the mechanisms of such an interaction will be interesting to explore.

In addition to CPECs, $K_{ir}7.1$ is also found on the apical side of RPE cells, where it works in concert with the Na^+,K^+-pump to maintain the ion homeostasis of the sub-retinal space[84]. $K_{ir}7.1$ is vital for normal RPE physiology, as RPE-specific deletion of the channel leads to photoreceptor degradation[82]. Mutations in $K_{ir}7.1$ gives rise to Snowflake Vitreoretinal Degeneration and Leber Congenital Amaurosis, retinal dystrophy disorders that also cause blindness[153]. Similar to CPECs, RPE cells utilize $K_{ir}7.1$ to balance the ion content of the cell through secretion of K^+ ions taken up by the Na^+,K^+-ATPase. Our results showed that $K_{ir}7.1$ expressed in RPE also responded to P4, which points to a potential regulatory role for P4 in the function of RPE. The effect of sex hormone signaling on RPE functions has not been well studied, although enzymes required for synthesis of P4 are found in the retina[154,155]. Changes in hormone production during aging are also thought to cause a difference in eye disorder

prevalence among men and women[155]. Further studies on the connection between P4 production in the eye and $K_{ir}7.1$ activity could give new insight into these discrepancies.

We are just beginning to observe the full impact of $K_{ir}7.1$ on brain functions, especially since a recent study by Papanikolaou et al.[156] showed expression of $K_{ir}7.1$ throughout the brain, in both neuronal and glial structures. In addition, $K_{ir}7.1$ is highly expressed in tissues such as the thyroid, small intestine, and uterus. During pregnancy, $K_{ir}7.1$ is known to influence the contractility of uterine smooth muscle cells[141]. High levels of P4 at mid-gestation cause an increased expression of *Kcnj13* (the gene encoding for $K_{ir}7.1$), which keeps the muscle tissue in a hyperpolarized state and prevents early contractions[141]. At the end of pregnancy, even before the drop in P4, *Kcnj13* expression is reduced and the resulting rise in membrane potential allows for an increased voltage-gated influx of Ca^{2+} and initiation of labor[141]. Our results now point to an additional, non-genomic function for P4, which could, hypothetically, prevent preterm labor. High levels of P4, together with an increased number of $K_{ir}7.1$ in the myometrium, would cause a significant hyperpolarization of the tissue, while even a rapid reduction in P4 levels could have a detrimental effect on $K_{ir}7.1$ conductance and pregnancy outcome.

Our data prompts future studies on the relationship between P4-driven $K_{ir}7.1$ regulation and CSF production, as well as the regulation of ventricle size. It also would be important to explore the role of P4-activation of $K_{ir}7.1$ in TBI pathology. At high enough concentrations, P4 could lead to hyperpolarization, altering ion exchange and inhibiting water secretion into the ventricles, which ultimately would benefit TBI patients. Since the natural triterpenoid, ursolic acid, has been shown to mitigate the long-term effects of TBI by improving cognition and motor control through an unknown mechanism, we tested the effects of ursolic acid on recombinant Kir7.1 expressed in HEK293 cells. We found that UA alone had no effect on $K_{ir}7.1$. However, in the presence of progesterone, UA was shown inhibit the initial progesterone-induced potentiation of $K_{ir}7.1$. This inhibition by UA was inhibited only slightly more by VU590. While unexpected because of UA's known effects in the brain, these results are not surprising as ursolic acid has been previously shown to antagonize progesterone activation[157]. While the role in the brain is unclear, these data give more insight into the role of $K_{ir}7.1$ in the uterus. Motherwort, botanical name *Leonurus cardiaca,* has been shown to be a potential abortifacient because of its ability to initiate contractions in the uterus. A main component of motherwort is ursolic acid. Therefore, ursolic acid in the motherword could be inhibiting P4 activation of $K_{ir}7.1$, resulting in depolarization of the uterine muscle, and subsequent uterine contraction. Further studies will need to be done to confirm this hypothesis.

While the low micromolar concentration range required for $K_{ir}7.1$ activation appears high for CSF, which is known to have a low composition of steroid carriers, the concentration of steroid hormones within the CPEC plasma membrane is not known. The filtration rate of the CP is ~ 0.5L per day, which allows for a total exchange of the 150 mL CSF within the ventricular system 2-3 times daily. As filtration progresses, it leads to accumulation of lipophilic compounds and locally produced neurosteroids in the CPEC plasma membrane, which could potentially reach the concentration levels required for channel modulation.

In conclusion, the inwardly rectifying potassium channel $K_{ir}7.1$is emerging as the major ion channel in the CP potentiated by P4 via a GPCR-independent mechanism. As few endogenous

regulators of $K_{ir}7.1$ are known, its P4-activation as well as UA inhibition, represent novel significant regulatory modalities for this channel. The fast-acting potentiation of $K_{ir}7.1$ by P4 was steroid specific and took place regardless of what cell type the channel was expressed in. The impact of P4 regulation on $K_{ir}7.1$ may, therefore, not be limited to the CP and RPE but extend to all tissues where the channel is found. Future studies should focus on the possible impact of increased P4 levels on these tissues.

References:

1. D'Orazio, J., Jarrett, S., Amaro-Ortiz, A. & Scott, T. UV radiation and the skin. *International Journal of Molecular Sciences* vol. 14 12222–12248 (2013).
2. Gordon, R. Skin cancer: An overview of epidemiology and risk factors. *Semin. Oncol. Nurs.* **29**, 160–169 (2013).
3. Department of Health, U. & Services, H. *The Surgeon General's Call to Action to Prevent Skin Cancer*. http://www.surgeongeneral.gov. (2014).
4. Mohan, S. V. & Chang, A. L. S. Advanced Basal Cell Carcinoma: Epidemiology and Therapeutic Innovations. *Curr. Dermatol. Rep.* **3**, 40–45 (2014).
5. Institute, N. N. C. Cancer Facts & Figures 2020. (2020).
6. Pavri, S. N., Clune, J., Ariyan, S. & Narayan, D. Malignant melanoma: Beyond the basics. *Plast. Reconstr. Surg.* **138**, 330e-340e (2016).
7. Thiery, J. P. Epithelial-mesenchymal transitions in development and pathologies. *Current Opinion in Cell Biology* vol. 15 740–746 (2003).
8. Gupta, P. B. *et al.* The melanocyte differentiation program predisposes to metastasis following neoplastic transformation. *Nat. Genet.* **37**, 1047–1054 (2005).
9. American Cancer Society. *Cancer Facts and Figures 2020*. https://www.cancer.org/content/dam/cancer-org/research/cancer-facts-and-statistics/annual-cancer-facts-and-figures/2020/cancer-facts-and-figures-2020.pdf (2020).
10. Still, R. & Brennecke, S. Melanoma in pregnancy. *Obstetric Medicine* vol. 10 107–112 (2017).
11. Joosse, A. *et al.* Gender differences in melanoma survival: Female patients have a decreased risk of metastasis. *J. Invest. Dermatol.* **131**, 719–726 (2011).
12. Gamba, C. S., Clarke, C. A., Keegan, T. H. M., Tao, L. & Swetter, S. M. Melanoma survival disadvantage in young, non-hispanic white males compared with females. *JAMA Dermatology* **149**, 912–920 (2013).
13. Donley, G. M. *et al.* Reproductive factors, exogenous hormone use and incidence of melanoma among women in the United States. *Br. J. Cancer* **120**, 754–760 (2019).
14. Fisher, D. E. & Geller, A. C. Disproportionate burden of melanoma mortality in young US men: The possible role of biology and behavior. *JAMA Dermatology* vol. 149 903–904 (2013).
15. Chen, J. *et al.* Gender-Based Differences and Barriers in Skin Protection Behaviors in Melanoma Survivors. *J. Skin Cancer* **2016**, (2016).
16. Choi, K. *et al. Prevalence and Characteristics of Indoor Tanning Use Among Men and Women in the United States*. *Arch Dermatol* vol. 146 http://archderm.jamanetwork.com/ (2010).
17. Mulliken, J. S., Russak, J. E. & Rigel, D. S. The Effect of Sunscreen on Melanoma Risk. *Dermatologic Clinics* vol. 30 369–376 (2012).
18. Jarrett, S. G., Orazio, J. A. D., Biology, C. & Sciences, N. Hormonal Regulation of the Repair of UV Photoproducts in Melanocytes by the Melanocortin Signaling Axis. **93**, 245–258 (2018).
19. Nasti, T. H. & Timares, L. MC1R, eumelanin and pheomelanin: Their role in determining the susceptibility to skin cancer. *Photochem. Photobiol.* **91**, 188–200 (2015).

20. Mahendraraj, K. *et al.* Malignant Melanoma in African-Americans. *Med. (United States)* **96**, (2017).

21. Davis, E. J., Johnson, D. B., Sosman, J. A. & Chandra, S. Melanoma: What do all the mutations mean? *Cancer* **124**, 3490–3499 (2018).

22. Ascierto, P. A. *et al. The role of BRAF V600 mutation in melanoma.* http://www.translational-medicine.com/content/10/1/85 (2012).

23. American Academy of Dermatology. https://www.aad.org/media/stats-skin-cancer.

24. Delyon, J., Lebbe, C. & Dumaz, N. Targeted therapies in melanoma beyond BRAF: Targeting NRAS-mutated and KIT-mutated melanoma. *Current Opinion in Oncology* vol. 32 79–84 (2020).

25. Medical University of Vienna. Melanoma: mechanisms of BRAF-inhibitor resistance deciphered. *Science Daily* www.sciencedaily.com/releases/2016/08/160829094302.htm (2016).

26. Wahid, M. *et al.* Recent developments and obstacles in the treatment of melanoma with BRAF and MEK inhibitors. *Critical Reviews in Oncology/Hematology* vol. 125 84–88 (2018).

27. Arozarena, I. & Wellbrock, C. Overcoming resistance to BRAF inhibitors. *Ann. Transl. Med.* **5**, 1–12 (2017).

28. Kaur, A., Webster, M. R. & Weeraratna, A. T. In the Wnt-er of life: Wnt signalling in melanoma and ageing. *British Journal of Cancer* vol. 115 1273–1279 (2016).

29. Seberg, H. E., Van Otterloo, E. & Cornell, R. A. Beyond MITF: Multiple transcription factors directly regulate the cellular phenotype in melanocytes and melanoma. *Pigment Cell Melanoma Res.* **30**, 454–466 (2017).

30. Mort, R. L., Jackson, I. J. & Elizabeth Patton, E. The melanocyte lineage in development and disease. *Development (Cambridge)* vol. 142 620–632 (2015).

31. Kawakami, A. & Fisher, D. E. The master role of microphthalmia-associated transcription factor in melanocyte and melanoma biology. *Lab. Investig.* **97**, 649–656 (2017).

32. Hartman, M. L. & Czyz, M. MITF in melanoma: Mechanisms behind its expression and activity. *Cell. Mol. Life Sci.* **72**, 1249–1260 (2015).

33. Wellbrock, C. & Arozarena, I. Microphthalmia-associated transcription factor in melanoma development and MAP-kinase pathway targeted therapy. *Pigment Cell Melanoma Res.* **28**, 390–406 (2015).

34. Hsiao, J. J. & Fisher, D. E. The roles of microphthalmia-associated transcription factor and pigmentation in melanoma. *Archives of Biochemistry and Biophysics* vol. 563 28–34 (2014).

35. Hoek, K. S. & Goding, C. R. Cancer stem cells versus phenotype-switching in melanoma. *Pigment Cell and Melanoma Research* vol. 23 746–759 (2010).

36. Seberg, H. E., Van Otterloo, E. & Cornell, R. A. Beyond MITF: Multiple transcription factors directly regulate the cellular phenotype in melanocytes and melanoma. *Pigment Cell and Melanoma Research* vol. 30 454–466 (2017).

37. Zhang, L. shu & Lum, L. Chemical Modulation of WNT Signaling in Cancer. in *Progress in Molecular Biology and Translational Science* vol. 153 245–269 (Elsevier B.V., 2018).

38. Sinnberg, T. *et al.* β-catenin signaling increases during melanoma progression and promotes tumor cell survival and chemoresistance. *PLoS One* **6**, (2011).

39. Zhan, T., Rindtorff, N. & Boutros, M. Wnt signaling in cancer. *Oncogene* vol. 36 1461–1473 (2017).

40. Weeraratna, A. T. *A Wnt-er Wonderland-The complexity of Wnt signaling in melanoma. Cancer and Metastasis Reviews* vol. 24 (2005).

41. Stamos, J. L. & Weis, W. I. The β-catenin destruction complex. *Cold Spring Harbor Perspectives in Biology* vol. 5 (2013).

42. Vachtenheim, J. & Ondrušová, L. Microphthalmia-associated transcription factor expression levels in melanoma cells contribute to cell invasion and proliferation. *Exp. Dermatol.* **24**, 481–484 (2015).

43. Ji, Y., Hao, H., Reynolds, K., McMahon, M. & Zhou, C. J. Wnt Signaling in Neural Crest Ontogenesis and Oncogenesis. *Cells* **8**, 1173 (2019).

44. De, A. Wnt/Ca2+ signaling pathway: A brief overview. *Acta Biochimica et Biophysica Sinica* vol. 43 745–756 (2011).

45. O'Connell, M. P. & Weeraratna, A. T. Hear the wnt ror: How melanoma cells adjust to changes in Wnt. *Pigment Cell and Melanoma Research* vol. 22 724–739 (2009).

46. Popolo, A. *et al.* Two likely targets for the anti-cancer effect of indole derivatives from cruciferous vegetables: PI3K/Akt/mTOR signalling pathway and the aryl hydrocarbon receptor. *Semin. Cancer Biol.* **46**, 132–137 (2017).

47. Verhoeven, D. T. H., Goldbohm, R. A., Van Poppel, G., Verhagen, H. & Van Den Brandt, P. A. Epidemiological studies on Brassica vegetables and cancer risk. *Cancer Epidemiol. Biomarkers Prev.* **5**, 733–748 (1996).

48. Anderton, M. J. *et al.* Pharmacokinetics and tissue disposition of indole-3-carbinol and its acid condensation products after oral administration to mice. *Clin. Cancer Res.* **10**, 5233–5241 (2004).

49. Maruthanila, V. L., Poornima, J. & Mirunalini, S. Attenuation of carcinogenesis and the mechanism underlying by the influence of indole-3-carbinol and its metabolite 3,3′-diindolylmethane: A therapeutic marvel. *Adv. Pharmacol. Sci.* **2014**, (2014).

50. HIGDON, J., DELAGE, B., WILLIAMS, D. & DASHWOOD, R. Cruciferous vegetables and human cancer risk: epidemiologic evidence and mechanistic basis. *Pharmacol. Res.* **55**, 224–236 (2007).

51. Jiang, Y. *et al.* Anti-cancer effects of 3, 3'-diindolylmethane on human hepatocellular carcinoma cells is enhanced by calcium ionophore: The role of cytosolic Ca2+ and P38 mapk. *Front. Pharmacol.* **10**, 1–23 (2019).

52. Kim, B. G. *et al.* 3,3′-diindolylmethane suppressed cyprodinil-induced epithelial-mesenchymal transition and metastatic-related behaviors of human endometrial ishikawa cells via an estrogen receptor-dependent pathway. *Int. J. Mol. Sci.* **19**, (2018).

53. Su, M. *et al.* Inhibitory effect of the low-toxic exogenous aryl hydrocarbon receptor modulator 3'3-diindolylmethane on gastric cancer in mice. *Oncol. Lett.* **14**, 8100–8105 (2017).

54. Estela Ytelina Godínez Martínez. Effectiveness of DIM Supplements to Increase 2-OHE1/16 Ratio (EDIMI216OHE1). https://clinicaltrials.gov/ct2/show/NCT02525159 (2018).

55. Habtemariam, S. Antioxidant and Anti-inflammatory Mechanisms of Neuroprotection by Ursolic Acid: Addressing brain injury, cerebral ischemia, cognition deficit, anxiety, and depression. *Oxidative Medicine and Cellular Longevity* vol. 2019 (2019).

56. Bednarczyk-Cwynar, B., Ruszkowski, P., Jarosz, T. & Krukiewicz, K. Enhancing anticancer activity through the combination of bioreducing agents and triterpenes. *Future Med. Chem.* **10**, 511–525 (2018).

57.   Saleem, M. Lupeol, a novel anti-inflammatory and anti-cancer dietary triterpene. *Cancer Letters* vol. 285 109–115 (2009).

58.   Chudzik, M., Korzonek-Szlacheta, I. & Król, W. Triterpenes as potentially cytotoxic compounds. *Molecules* vol. 20 1610–1625 (2015).

59.   Kashyap, D., Tuli, H. S. & Sharma, A. K. Ursolic acid (UA): A metabolite with promising therapeutic potential. *Life Sciences* vol. 146 201–213 (2016).

60.   Li, J. *et al.* Anti-Cancer Effects of Pristimerin and the Mechanisms: A Critical Review. *Front. Pharmacol.* **10**, (2019).

61.   Petronellia, A., Pannitterib, G. & Testaa, U. Triterpenoids as new promising anticancer drugs. *Anti-Cancer Drugs* vol. 20 880–892 (2009).

62.   Kaur, C., Rathnasamy, G. & Ling, E. A. The choroid plexus in healthy and diseased brain. *J. Neuropathol. Exp. Neurol.* **75**, 198–213 (2016).

63.   Lun, M. P., Monuki, E. S. & Lehtinen, M. K. Development and functions of the choroid plexus-cerebrospinal fluid system. *Nature Reviews Neuroscience* vol. 16 445–457 (2015).

64.   Damkier, H. H., Brown, P. D. & Praetorius, J. Cerebrospinal fluid secretion by the choroid plexus. *Physiological Reviews* vol. 93 1847–1892 (2013).

65.   Spector, R., Keep, R. F., Robert Snodgrass, S., Smith, Q. R. & Johanson, C. E. A balanced view of choroid plexus structure and function: Focus on adult humans. *Experimental Neurology* vol. 267 78–86 (2015).

66.   Karimy, J. K. *et al.* Inflammation-dependent cerebrospinal fluid hypersecretion by the choroid plexus epithelium in posthemorrhagic hydrocephalus. *Nat. Med.* **23**, 997–1003 (2017).

67.   Kant, S., Stopa, E. G., Johanson, C. E., Baird, A. & Silverberg, G. D. Choroid plexus genes for CSF production and brain homeostasis are altered in Alzheimer's disease. *Fluids Barriers CNS* **15**, (2018).

68.   Lun, M. P., Monuki, E. S. & Lehtinen, M. K. Development and functions of the choroid plexus-cerebrospinal fluid system. *Nat. Rev. Neurosci.* **16**, 445–457 (2015).

69.   Marques, F. *et al.* The choroid plexus in health and in disease: dialogues into and out of the brain. *Neurobiology of Disease* vol. 107 32–40 (2017).

70.   Telano, L. & Baker, S. *Physiology, Cerebral Spinal Fluid (CSF)*. (StatPearls Publishing, 2018).

71.   Johanson, C. E. *et al.* Multiplicity of cerebrospinal fluid functions: New challenges in health and disease. *Cerebrospinal Fluid Research* vol. 5 (2008).

72.   Cheng, Y. & Haorah, J. *How does the brain remove its waste metabolites from within? Int J Physiol Pathophysiol Pharmacol* vol. 11 www.ijpppp.org (2019).

73.   Trillo-Contreras, J., Toledo-Aral, J., Echevarría, M. & Villadiego, J. AQP1 and AQP4 Contribution to Cerebrospinal Fluid Homeostasis. *Cells* **8**, 197 (2019).

74.   Kaur, C., Rathnasamy, G. & Ling, E. A. The choroid plexus in healthy and diseased brain. *Journal of Neuropathology and Experimental Neurology* vol. 75 198–213 (2016).

75.   Redzic, Z. B., Preston, J. E., Duncan, J. A., Chodobski, A. & Szmydynger-Chodobska, J. The Choroid Plexus-Cerebrospinal Fluid System: From Development to Aging. *Current Topics in Developmental Biology* vol. 71 1–52 (2005).

76.   Krapivinsky, G. *et al. A Novel Inward Rectifier K Channel with Unique Pore Properties*. *Neuron* vol. 20 (1998).

77.   Rosenhouse-Dantsker, A., Leal-Pinto, E., Logothetis, D. E. & Levitan, I. *Comparative analysis of cholesterol sensitivity of Kir channels: role of the CD loop*. *Channels (Austin)*

vol. 4 (2010).

78. Shahi, P. K. *et al.* Abnormal Electroretinogram after Kir7.1 Channel Suppression Suggests Role in Retinal Electrophysiology. *Sci. Rep.* **7**, (2017).

79. Hibino, H. *et al.* Inwardly Rectifying Potassium Channels: Their Structure, Function, and Physiological Roles. (2010) doi:10.1152/physrev.00021.2009.-Inwardly.

80. Millar, I. D., Bruce, J. I. E. & Brown, P. D. Ion channel diversity, channel expression and function in the choroid plexuses. *Cerebrospinal Fluid Res.* **4**, 1–16 (2007).

81. Ookata, K. *et al. Localization of Inward Rectifier Potassium Channel Kir7.1 in the Basolateral Membrane of Distal Nephron and Collecting Duct.* (2000).

82. Roman, D., Zhong, H., Yaklichkin, S., Chen, R. & Mardon, G. Conditional loss of Kcnj13 in the retinal pigment epithelium causes photoreceptor degeneration. *Exp. Eye Res.* **176**, 219–226 (2018).

83. Nakamura, N. *et al. Inwardly rectifying K+ channel Kir7.1 is highly expressed in thyroid follicular cells, intestinal epithelial cells and choroid plexus epithelial cells : implication for a functional coupling with Na+,K+-ATPase. Biochem. J* vol. 342 (1999).

84. Shimura, M. *et al.* Expression and Permeation properties of the K(+) channel Kir7.1 in the retinal pigment epithelium. *J. Physiol.* **531**, 329–346 (2001).

85. Mollayeva, T., Mollayeva, S. & Colantonio, A. Traumatic brain injury: sex, gender and intersecting vulnerabilities. *Nature Reviews Neurology* vol. 14 711–722 (2018).

86. Thurman, D., Alverson, C. & Browne, D. *Traumatic Brain Injury in the United States: A report to Congress.* https://www.cdc.gov/traumaticbraininjury/pdf/TBI_in_the_US.pdf (1999).

87. Zeiler, F. A. *et al.* Cerebrospinal fluid and microdialysis cytokines in severe traumatic brain injury: A scoping systematic review. *Frontiers in Neurology* vol. 8 (2017).

88. Yoon, J. E., Lee, C. Y., Sin, E. G., Song, J. & Kim, H. W. Clinical feature and outcomes of secondary hydrocephalus caused by head trauma. *Korean J. Neurotrauma* **14**, 86–92 (2018).

89. Johanson, C., Stopa, E., Baird, A. & Sharma, H. Traumatic brain injury and recovery mechanisms: Peptide modulation of periventricular neurogenic regions by the choroid plexus-CSF nexus. *J. Neural Transm.* **118**, 115–133 (2011).

90. Cherian, I. *et al.* Introducing the concept of "CSF-shift edema" in traumatic brain injury. *Journal of Neuroscience Research* vol. 96 744–752 (2018).

91. Johanson, C. E. *et al.* Atrial natriuretic peptide: its putative role in modulating the choroid plexus-CSF system for intracranial pressure regulation. *Acta Neurochir* **96**, 451–456 (2006).

92. Majeed, Y. *et al.* Stereo-selective inhibition of transient receptor potential TRPC5 cation channels by neuroactive steroids. *Br. J. Pharmacol.* **162**, 1509–1520 (2011).

93. Karahan, S., Yarim, G. & Yarim, M. Choroid epithelial cells: source cerebrospinal fluid progesterone in sheep? *Med Weter* **63**, 935–937 (2007).

94. Stein, D. G. & Wright, D. W. Progesterone in the clinical treatment of acute traumatic brain injury. *Expert Opinion on Investigational Drugs* vol. 19 847–857 (2010).

95. Jones, N. C. *et al.* The neuroprotective effect of progesterone after traumatic brain injury in male mice is independent of both the inflammatory response and growth factor expression. *Eur. J. Neurosci.* **21**, 1547–1554 (2005).

96. Santarsieri, M. *et al.* Cerebrospinal fluid cortisol and progesterone profiles and outcomes prognostication after severe traumatic brain injury. *J. Neurotrauma* **31**, 699–712 (2014).

97.   Deutsch, E. R. *et al.* Progesterone's role in neuroprotection, a review of the evidence. *Brain Research* vol. 1530 82–105 (2013).

98.   Stein, D. G. Progesterone exerts neuroprotective effects after brain injury. *Brain Research Reviews* vol. 57 386–397 (2008).

99.   Brotfain, E. *et al.* Neuroprotection by Estrogen and Progesterone in Traumatic Brain Injury and Spinal Cord Injury. *Curr. Neuropharmacol.* **14**, 641–653 (2016).

100. Stein, D. G. Embracing failure: What the Phase III progesterone studies can teach about TBI clinical trials. *Brain Injury* vol. 29 1259–1272 (2015).

101. Ramos-Hryb, A. B., Pazini, F. L., Kaster, M. P. & Rodrigues, A. L. S. Therapeutic Potential of Ursolic Acid to Manage Neurodegenerative and Psychiatric Diseases. *CNS Drugs* **31**, 1029–1041 (2017).

102. Ding, H., Wang, H., Zhu, L. & Wei, W. Ursolic Acid Ameliorates Early Brain Injury After Experimental Traumatic Brain Injury in Mice by Activating the Nrf2 Pathway. *Neurochem. Res.* **42**, 337–346 (2017).

103. Zhang, T. *et al.* Ursolic acid alleviates early brain injury after experimental subarachnoid hemorrhage by suppressing TLR4-mediated inflammatory pathway. *Int. Immunopharmacol.* **23**, 585–591 (2014).

104. Liang, W., Zhao, X., Feng, J., Song, F. & Pan, Y. Ursolic acid attenuates beta-amyloid-induced memory impairment in mice. *Arq. Neuropsiquiatr.* **74**, 482–488 (2016).

105. Liddelow, S. A. Development of the choroid plexus and blood-CSF barrier. *Front. Neurosci.* **9**, 1–13 (2015).

106. Johanson, C. E., Duncan, J. A., Stopa, E. G. & Baird, A. Enhanced prospects for drug delivery and brain targeting by the choroid plexus-CSF route. *Pharm. Res.* **22**, 1011–1037 (2005).

107. Kontogianni, G., Piroti, G., Maglogiannis, I., Chatziioannou, A. & Papadodima, O. Dissecting the mutational landscape of cutaneous melanoma: An omic analysis based on patients from Greece. *Cancers (Basel).* **10**, (2018).

108. De Unamuno Bustos, B. *et al.* Towards Personalized Medicine in Melanoma: Implementation of a Clinical Next-Generation Sequencing Panel. *Sci. Rep.* **7**, (2017).

109. Hodis, E. *et al.* A landscape of driver mutations in melanoma. *Cell* **150**, 251–263 (2012).

110. Rissmann, R., Hessel, M. H. M. & Cohen, A. F. Vemurafenib/dabrafenib and trametinib. *Br. J. Clin. Pharmacol.* **80**, 765–767 (2015).

111. Saleem, M. D. Biology of human melanocyte development, Piebaldism, and Waardenburg syndrome. *Pediatric Dermatology* vol. 36 72–84 (2019).

112. Weinstein, I. B. & Joe, A. K. Mechanisms of Disease: Oncogene addiction - A rationale for molecular targeting in cancer therapy. *Nature Clinical Practice Oncology* vol. 3 448–457 (2006).

113. Wellbrock, C. *et al.* Oncogenic BRAF regulates melanoma proliferation through the lineage specific factor MITF. *PLoS One* **3**, (2008).

114. Kundu, A., Quirit, J. G., Khouri, M. G. & Firestone, G. L. Inhibition of oncogenic BRAF activity by indole-3-carbinol disrupts microphthalmia-associated transcription factor expression and arrests melanoma cell proliferation. *Mol. Carcinog.* **56**, 49–61 (2017).

115. Higdon, J. V., Delage, B., Williams, D. E. & Dashwood, R. H. Cruciferous vegetables and human cancer risk: epidemiologic evidence and mechanistic basis. *Pharmacological Research* vol. 55 224–236 (2007).

116. Sarkar, F. H. & Li, Y. Harnessing the fruits of nature for the development of multi-

targeted cancer therapeutics. *Cancer Treatment Reviews* vol. 35 597–607 (2009).

117. Thomson, C. A., Ho, E. & Strom, M. B. Chemopreventive properties of 3,30-diindolylmethane in breast cancer: Evidence from experimental and human studies. *Nutr. Rev.* **74**, 432–443 (2016).

118. Lee, G. A., Hwang, K. A. & Choi, K. C. Roles of dietary phytoestrogens on the regulation of epithelial-mesenchymal transition in diverse cancer metastasis. *Toxins* vol. 8 (2016).

119. ATCC. *PBCF SOP Thawing, Propagating and Cryopreserving Protocol for NCI-PBCF-HTB68 SK-MEL-2 Malignant melanoma cells; Version 1.0.* http://www.atcc.org/Products/All/HTB-68.aspx (2013).

120. Gh. Benga. Basic studies on gene therapy of human malignant melanoma by use of the human interferon   gene entrapped in cationic multilamellar liposomes. *J. Cell. Mol. Med.* **5**, 402–408 (2001).

121. Hirai, H., Matoba, K., Mihara, E., Arimori, T. & Takagi, J. Crystal structure of a mammalian Wnt–frizzled complex. *Nat. Struct. Mol. Biol.* (2019) doi:10.1038/s41594-019-0216-z.

122. Maruthanila, V. L., Poornima, J. & Mirunalini, S. Attenuation of carcinogenesis and the mechanism underlying by the influence of indole-3-carbinol and its metabolite 3,3′-diindolylmethane: A therapeutic marvel. *Advances in Pharmacological Sciences* vol. 2014 (2014).

123. Banerjee, S. *et al.* Attenuation of multi-targeted proliferation-linked signaling by 3,3'-diindolylmethane (DIM): From bench to clinic. *Mutation Research - Reviews in Mutation Research* vol. 728 47–66 (2011).

124. Fujioka, N. *et al.* Urinary 3,30-diindolylmethane: A biomarker of glucobrassicin exposure and indole-3-carbinol uptake in humans. *Cancer Epidemiol. Biomarkers Prev.* **23**, 282–287 (2014).

125. Aronchik, I., Kundu, A., Quirit, J. G. & Firestone, G. L. The antiproliferative response of indole-3-carbinol in human melanoma cells is triggered by an interaction with NEDD4-1 and disruption of wild-type PTEN degradation. *Mol. Cancer Res.* **12**, 1621–1634 (2014).

126. Dean, L. *Vemurafenib Therapy and BRAF and NRAS Genotype. National Center for Biotechnology Information (US* (2017).

127. Goding, C. R. & Arnheiter, H. Mitf—the first 25 years. *Genes and Development* vol. 33 983–1007 (2019).

128. ATCC. G-361 product sheet. www.atcc.org.

129. ATCC. *SK-MEL-2 product sheet*. www.atcc.org.

130. Bandarchi, B., Jabbari, C. A., Vedadi, A. & Navab, R. Molecular biology of normal melanocytes and melanoma cells. *J. Clin. Pathol.* **66**, 644–648 (2013).

131. Hari, L. *et al.* Lineage-specific requirements of β-catenin in neural crest development. *J. Cell Biol.* **159**, 867–880 (2002).

132. Iqbal, J. *et al.* Ursolic acid a promising candidate in the therapeutics of breast cancer: Current status and future implications. *Biomedicine and Pharmacotherapy* vol. 108 752–756 (2018).

133. Hagemann, G. *et al.* Changes in brain size during the menstrual cycle. *PLoS One* **6**, (2011).

134. Oatridge, A. *et al. Change in Brain Size during and after Pregnancy: Study in Healthy Women and Women with Preeclampsia.*

135. Luoma, J. I., Kelley, B. G. & Mermelstein, P. G. Progesterone inhibition of voltage-gated

calcium channels is a potential neuroprotective mechanism against excitotoxicity. *Steroids* **76**, 845–855 (2011).

136. Kelley, B. G. & Mermelstein, P. G. Progesterone blocks multiple routes of ion flux. *Mol. Cell. Neurosci.* **48**, 137–141 (2011).

137. Pettus, E. H., Wright, D. W., Stein, D. G. & Hoffman, S. W. Progesterone treatment inhibits the inflammatory agents that accompany traumatic brain injury. *Brain Res.* **1049**, 112–119 (2005).

138. Miller, M. R. *et al.* Unconventional endocannabinoid signaling governs sperm activation via the sex hormone progesterone. *Science (80-.).* **352**, 555–559 (2016).

139. Lösel, R. & Wehling, M. Nongenomic actions of steroid hormones. *Nature Reviews Molecular Cell Biology* vol. 4 46–56 (2003).

140. Yin, W. *et al.* The potassium channel KCNJ13 is essential for smooth muscle cytoskeletal organization during mouse tracheal tubulogenesis. *Nat. Commun.* **9**, (2018).

141. McCloskey, C. *et al.* The inwardly rectifying K + channel KIR 7.1 controls uterine excitability throughout pregnancy . *EMBO Mol. Med.* **6**, 1161–1174 (2014).

142. Björkgren, I. *et al.* Alpha/Beta Hydrolase Domain-Containing Protein 2 regulates the rhythm of follicular maturation and estrous stages of the female reproductive cycle. doi:10.1101/684951.

143. Johnson, B. A. *et al.* Accurate, strong, and stable reporting of choroid plexus epithelial cells in transgenic mice using a human transthyretin BAC. *Fluids Barriers CNS* **15**, (2018).

144. Shang, P., Stepicheva, N. A., Hose, S., Zigler, J. S. & Sinha, D. Primary cell cultures from the mouse retinal pigment epithelium. *J. Vis. Exp.* **2018**, (2018).

145. Carrington, S. J. *et al.* G protein– coupled receptors differentially regulate glycosylation and activity of the inwardly rectifying potassium channel Kir7.1. *J. Biol. Chem.* **293**, 17739–17753 (2018).

146. Lindvall-Axelsson, M. & Owman, C. Actions of sex steroids and corticosteroids on rabbit choroid plexus as shown by changes in transport capacity and rate of cerebrospinal fluid formation. *Neurol. Res.* **12**, 181–186 (1990).

147. Miehe, S. *et al.* Inhibition of diacylglycerol-sensitive TRPC channels by synthetic and natural steroids. *PLoS One* **7**, (2012).

148. Sackin, H., Nanazashvili, M., Li, H., Palmer, L. G. & Walters, D. E. A conserved arginine near the filter of Kir1.1 controls Rb/K selectivity. *Channels* **4**, (2010).

149. Fürst, O., Nichols, C. G., Lamoureux, G. & Davanzo, N. Identification of a cholesterol-binding pocket in inward rectifier K+ (Kir) channels. *Biophys. J.* **107**, 2786–2796 (2014).

150. Korkmaz, F. & Severcan, F. Effect of progesterone on DPPC membrane: Evidence for lateral phase separation and inverse action in lipid dynamics. *Arch. Biochem. Biophys.* **440**, 141–147 (2005).

151. Mcdonnel, A. C., Van Kirk, E. A., Isaak, D. D. & Murdoch}, W. J. *Inhibitory Effects of Progesterone on Plasma Membrane Fluidity and Tumorigenic Potential of Ovarian Epithelial Cancer Cells*. *Exp Bioi Med* vol. 228 (2003).

152. Whiting, K. P., Restall, C. J. & Brain, P. F. *Steroid hormone-induced effects on membrane ßuidity and their potential roles in non-genomic mechanisms*. *Life Sciences* vol. 67 (2000).

153. Hejtmancik, J. F. *et al.* Mutations in KCNJ13 Cause Autosomal-Dominant Snowflake Vitreoretinal Degeneration. *Am. J. Hum. Genet.* **82**, 174–180 (2008).

154. Guarneri, P. *et al. Neurosteroidogenesis in Rat Retinas*. *J. Neurochem* vol. 63 (1994).

155. Cascio, C., Deidda, I., Russo, D. & Guarneri, P. The estrogenic retina: The potential contribution to healthy aging and age-related neurodegenerative diseases of the retina. *Steroids* **103**, 31–41 (2015).

156. Papanikolaou, M., Lewis, A. & Butt, A. M. Glial and neuronal expression of the Inward Rectifying Potassium Channel Kir7.1 in the adult mouse brain. *J. Anat.* **235**, 984–996 (2019).

157. Mannowetz, N., Miller, M. R. & Lishko, P. V. Regulation of the sperm calcium channel CatSper by endogenous steroids and plant triterpenoids. *Proc. Natl. Acad. Sci. U. S. A.* **114**, 5743–5748 (2017).